

SEGMENTING the UNIVERSE

Master Thesis by Erwin Platen

Supervised by Rien van de Weygaert

Contents

1	Introduction to Cosmic Large Scale Structure	1
1.1	From minuscule to immense	1
1.2	Observed large scale structure	3
1.2.1	Voids, discovered by nothing	4
1.2.2	Galaxies in Voids	6
1.2.3	The Evolution of Voids	6
1.2.4	Outline	7
2	Isolated void evolution: the spherical case	8
3	The Excursion Set Model of Void Evolution	12
3.1	Press-Schechter model of haloes	12
3.2	Excursion Sets	13
3.3	The Void Distribution	15
4	Void N-Body Simulations	20
4.1	The Initial Conditions	21
4.1.1	The Powerlaw Voids	23
4.2	Global Void Evolution	23
4.3	Void Collapse	28
5	Segmentation by overflow	33
5.1	Void Detection	34
5.2	Introduction to Mathematical Morphology	36
5.2.1	Grayscale Images	37
5.2.2	Distances	38
5.3	Watersheds in image segmentation	39
5.4	The watershed transform, continuous case	40
5.5	The watershed transform, discrete case and algorithms	42
5.5.1	Plateau problem	43
5.5.2	Oversegmentation	43
5.6	Discrete point distributions and continuous density fields	44
5.7	Extensions to three dimensions	44
6	Segmentation: the Kinematic Voronoi Model, a testcase	45
6.1	Kinematic Voronoi Model	45
6.2	Watershed on the Kinematic Voronoi Model	46
6.2.1	Smoothing	48
6.2.2	Thresholding	52
6.2.3	Thresholding and Smoothing	52

7	Segmentation, the “real” world	55
7.1	GIF density field	57
7.1.1	Grey levels	58
7.2	GIF Watersheds	59
7.2.1	Watersheds and the <i>Cosmic Skeleton</i>	60
7.2.2	Watersheds and the <i>Void Hierarchy</i>	62
7.2.3	Watersheds and the Void Size Distribution	67
7.3	Watersheds and Void Evolution	74
7.3.1	Lagrangian Evolution of the Watershed Selected Particles	84
8	Conclusion	88
9	Discussion and Future Prospects	90
A	Delaunay Triangulation Field Estimation, DTFE	92
A.1	Delaunay-Voronoi tessellations	92
A.2	Interpolation of points distribution to a grid	93
B	Simulation Method, P³M	94

Abstract

One of the most striking aspects of redshift surveys is that there are huge regions of space totally devoid of galaxies. These are the cosmic voids, which grew hierarchically from the initial density troughs in the primordial fluctuation field. In a hierarchical structure formation scenario smaller voids build up larger ones; the void hierarchy. In this paper we study the void evolution and merging history of large voids and void ensembles. We do this by means of constrained realizations of Gaussian fields, which are our initial fields for N-body simulations. Our direct goal was to test the theoretical model of Sheth & van de Weygaert (2004). In this model they proposed that small voids can either merge into larger ones or collapse into larger overdense regions. Preliminary analysis confirms this model, where smaller voids either merge away in large voids, analogue to build up of large haloes or small voids can collapse away. The model assumes that small voids collapse, if they are embedded in larger spherical overdensities. Our results, however, indicate that this condition might be even too stringent and that void-collapse also occurs when the local deformation, caused by the tidal field, is strong enough that it can shear and tear away voids into filaments or walls. In order to track this Lagrangian evolution of small voids and its surrounding in an objective manner we propose the usage of the Watershed transformation. This tool combines the capability of detecting filaments and voids simultaneous in a parameter free way. In combination with the DTFE interpolation method we regard it as an excellent tool to extract and visualize the cosmic foam. Here we present the 2 dimensional version with applications to slices out of a large simulation. In upcoming work it will be extended to three dimensions and we expect it to use as a foam extractor.

Chapter 1

Introduction to Cosmic Large Scale Structure

1.1 From minuscule to immense

About 13 billion years ago, an extremely hot and compact ball of energy started to expand, forming the Universe where we live in today. According to the most commonly accepted model, the Universe is made up of four major components; dark energy, dark matter, baryons and radiation. As the Universe expanded, it went through several distinct phases, each with their own characteristic timescales, and governed by their own physically dominant processes. The earliest signal that can be observed is the Cosmic Microwave Background (CMB). It dates back to a time when the Universe was only 380 thousand years old. It is the oldest observable object, and tells a lot about the conditions of the early Universe. For example, it contains information how the present day structure came about, what kinds of matter it is made up of, how much of each species was around, what the geometry and age of the Universe is, and many more .

In describing the Universe, the Robertson-Walker metric and the Friedmann equation, are used to formulate the expansion of the Universe. These describe the dynamics of the space-time on the grandest scales, and strictly valid for an isotropic and homogeneous Universe. To great precision on the largest scales, it is observed that the Universe indeed looks the same everywhere and in every direction. However, on scales smaller than about 100-150 $h^{-1}\text{Mpc}$ we see a rich and varied structure corresponding to the Large Scale Structure (LSS). Fluctuations on this uniform background are for example galaxies, stars and people. These fluctuations originate from a time before the formation of the CMB and figure(1.1) shows these fluctuations in the temperature map of CMB. These temperature perturbations are still very small in amplitude, but it are these same perturbations that grew into the stars, galaxies, clusters, etc. that we see today. These primordial fluctuations are also the initial conditions for the subject described here, i.e. the voids in the large scale structure.

We assume that the primordial density and velocity fluctuations are produced during inflation and that they are Gaussian random field, meaning that fluctuations in each scale are independent Gaussians, distributed around zero with a characteristic average spread, i.e. the power spectrum. The media in which these fluctuations can originate are matter and radiation. Dependent on the mode of perturbations these are either adiabatic (adiabatic change of volume elements in the isotropic field) and these are both fluctuations in the matter as the radiation field. Alternatively they could be isocurvature (perturbation of the entropy, but not in the energy distribution), which are matter perturbations, while the radiation is constant. The growth of these fluctuations in each medium behaves distinctly though not independently, and here we are only concerned with the evolution of the dark matter fluctuations.

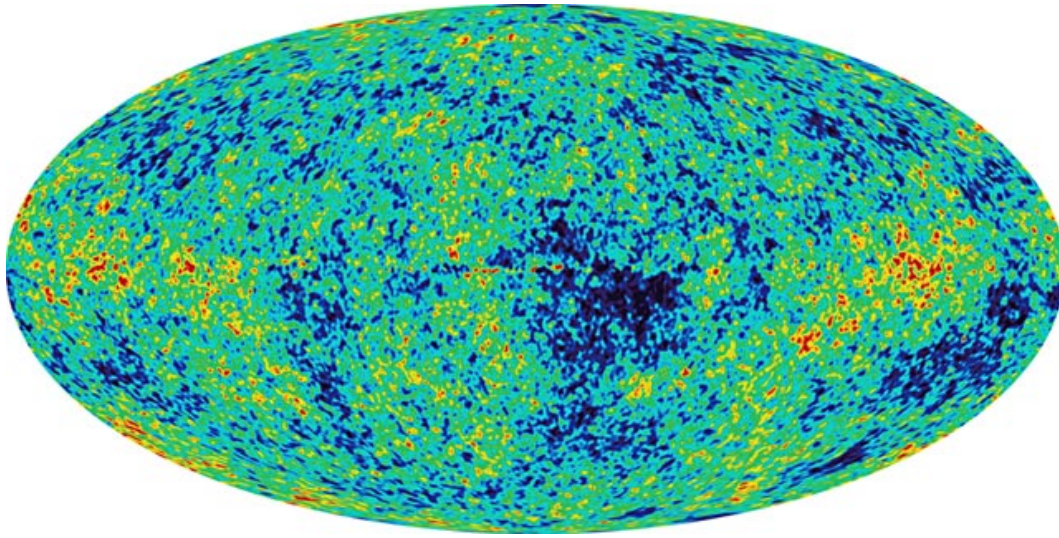


Figure 1.1: The cosmic microwave background as observed by WMAP. The colors indicate slightly higher and slightly lower temperatures. These represent the same kind of fluctuations from which the Large Scale Structure formed.

Several phases of the dark matter structure growth can be discerned. Beginning with the Gaussian random field, which is fully specified by its power spectrum, i.e. the average power at each wavelength. This initial spectrum can have several shapes depending on what kind of dark matter is most dominant. The most commonly considered model of dark matter is the Cold Dark Matter version, which has two important characteristics; it does not interact with normal matter and it is only noted through its gravitational force. The characteristics of a CDM spectrum is that there is more power on decreasing mass scales. A spectrum with such a shape describes structure formation scenario which is hierarchical. In such a scenario small structures emerge before they get embedded into larger ones. The evolution of the CDM distribution may be reasonably by the pressureless fluid equation with inclusion of a gravitational driving term. In the early stages the solution of this set of coupled equation can be approximated with linear perturbation theory. This gives a universal growth factor for each scale. During the linear stage of evolution the spatial matter retains its topology, and that the perturbation values are just uniformly multiplied by this factor.

However the strongest perturbations begin to contract under self-gravity and ultimately collapse into a compact clump. Initially these will be small clumps as on small scales there is more power than on the larger scales. Subsequently many of these clumps merge to form yet larger ones, which in turn can accrete small clumps or merge into even larger ones. Complete solution of the nonlinear perturbation equations is quickly rendered impossible once the process gets dominated by higher order terms. For various clustering regimes we may still use some extremely useful analytical formulations. In highly symmetric circumstances the non-linear evolution can be followed with the spherical perturbation model. If small scales fluctuations are ignored then the Lagrangian evolution of the density field is described by the Zel'dovich approximation. Furthermore, in a hierarchical model, every clump has to grow from merging and accretion of smaller clumps. Therefore, by filtering the initial fluctuation field on ever increasing scales, the merging history of clumps can be traced, this is the Press-Schechter/Excursion formalism.

While these models are successful in predicting certain aspects of the Large Scale Structure, they do not manage to describe the full nonlinear evolution. In order to do so, one must resort to do simulations of the structure formation scenario. This is usually done by means of N-body

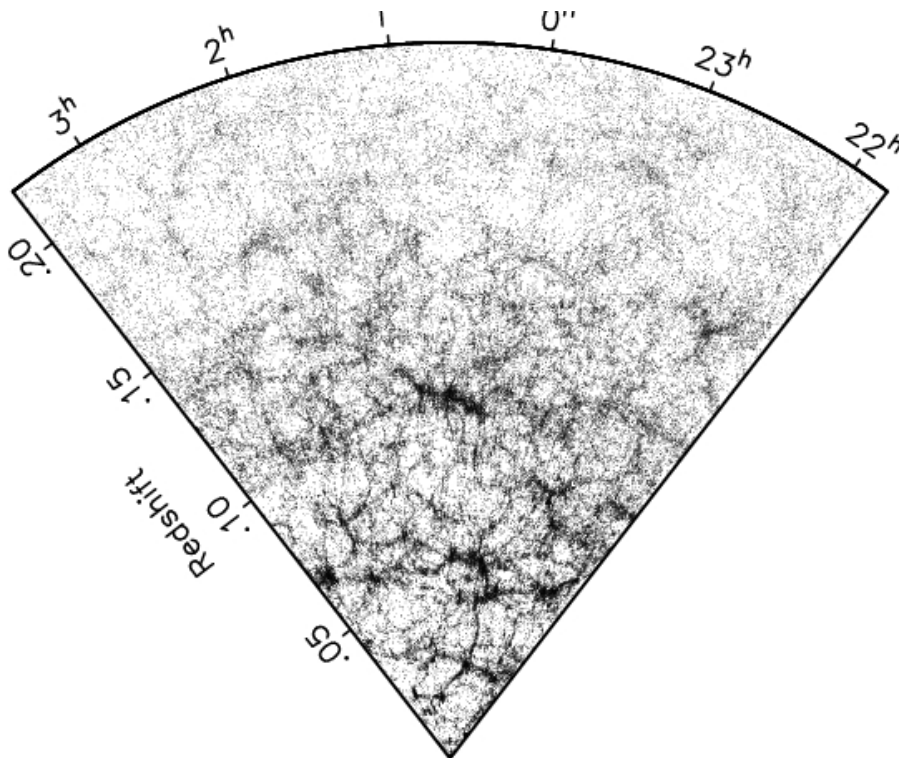


Figure 1.2: A map of the local Universe out to a redshift of $z=0.2$ (corresponds to a distance of about $500 h^{-1}\text{Mpc}$). In the picture each dot represents a galaxy. This redshift survey of galaxies was made by the 2dFGRS team and the total survey encompasses of the order of 10^5 galaxy redshifts measurements. A striking aspect is the foamy appearance of the LSS, where superclusters and voids segment the Universe into empty like bubbles surrounded by massive walls and filaments. Also visible are the radial directed needle like structures, which are clusters of galaxies smeared out due to their large internal velocities. Although somewhat less pronounced, but visible, is the void hierarchy. The thin filamentary substructures inside larger voids, which are delineated by the most massive galaxy conglomerations; the superclusters. *Courtesy of W.Schaap & 2dFGRS consortium*

simulations, where particles trace the Lagrangian evolution of a volume of fluid material. The outcome of simulations of the large scale structure, can be confronted with maps of the galaxy distribution.

1.2 Observed large scale structure

That galaxies are not distributed regularly through space is a fact dating back to the earliest extragalactic observations by E. Hubble. The model advocated by Hubble was that galaxies are randomly distributed, and isotropic on the larger scales. However, it was noticed already at a very early stage that nearby galaxies have a striking anisotropic distribution, which later was realized to be a reflection of the Local Supercluster. Subsequently the hypothesis was proposed that galaxies might be ordered in yet larger structures. This spatial distribution of galaxies is referred to as the Large Scale Structure (LSS) of the Universe. This structure was never discovered by one individual, but was gradually confirmed by observation and in time has been steadily expanded by observational and analytical work of people like Hubble, Oort, Zwicky, Zel'dovich.

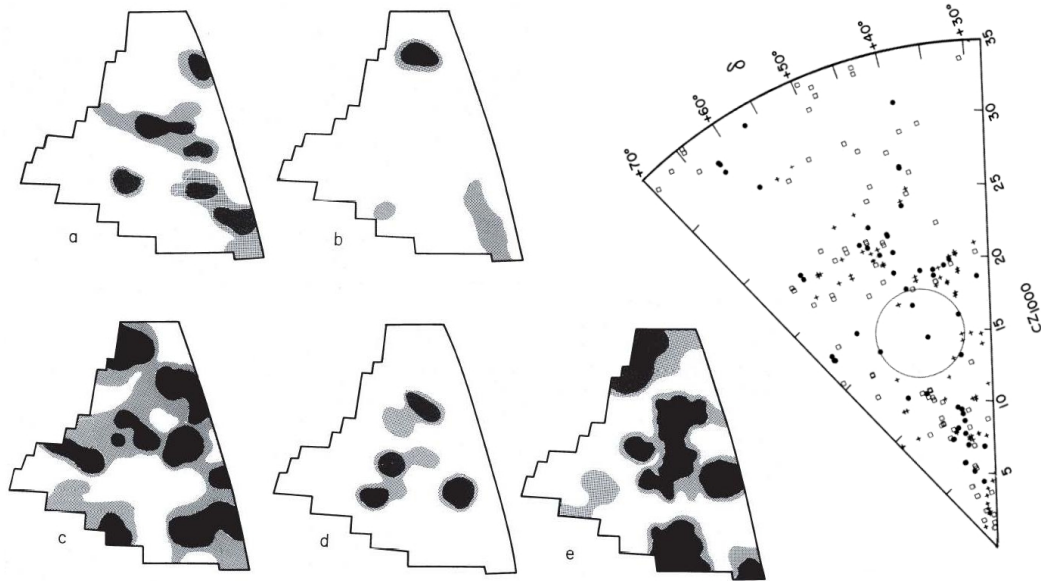


Figure 1.3: The contour plots are five consecutive slices through the Boötes void, especially note the empty second slice.

Since the time of the first extragalactic observations, the surveys have increased their typical amount of observed galaxies by orders of magnitude. This progress is particularly due to the great advances in telescope technology, the higher sensitivity of detectors and great leaps in computing power. The picture that emerged is that galaxies act as the fundamental building block of the LSS, which is organized in ever increasing objects, beginning with galaxies, followed by groups, clusters, filaments, walls and largest objects which can be identified are voids and superclusters. Superclusters seem to be the most massive recognizable structural entities in the Universe, basically they represent the clusters of clusters of galaxies. Perhaps voids are the largest objects that can be identified in the spatial distribution of galaxies. While they represent less mass than the overdense filaments, walls and clusters they do occupy by far the largest fraction of space. Together, voids and superclusters produce the foamy appearance of the LSS that is readily visible in the figure(1.2). This cosmic foam is clearly visible in the Sloan Digital Sky Survey (SDSS) and the 2degree Field Galaxy Redshift Survey (2dFGRS), which are major galaxy redshift campaigns. A variety of statistical measures like for example the two point correlation function can specify various characteristics of the LSS.

1.2.1 Voids, discovered by nothing

Here we will focus on one component of the Large Scale Structure, namely the voids. It is unknown to whom the word 'void' must be attributed, but it is supposed to be a contraction of "region devoid of any galaxy", see Rood(1989). Voids are huge underdense regions, and by definition almost devoid of any galaxy. Logically, much of the attention has gone into the study of the formation of these overdense regions, be it superclusters, clusters or galaxies. The first detection of voids in the large scale structure happened at the same time that superclusters were confirmed, as both are responsible for the appearance of the LSS. The Coma and Hercules void were one of the first detected voids by resp. Gregory & Thomson(1978) and Chincarini & Rood (1981). At about the same time the Boötes void (figure 1.3) was discovered by Kishner et al.(1981). The Boötes void is a huge underdense region of $100 h^{-1}\text{Mpc}$ scale. These large voids

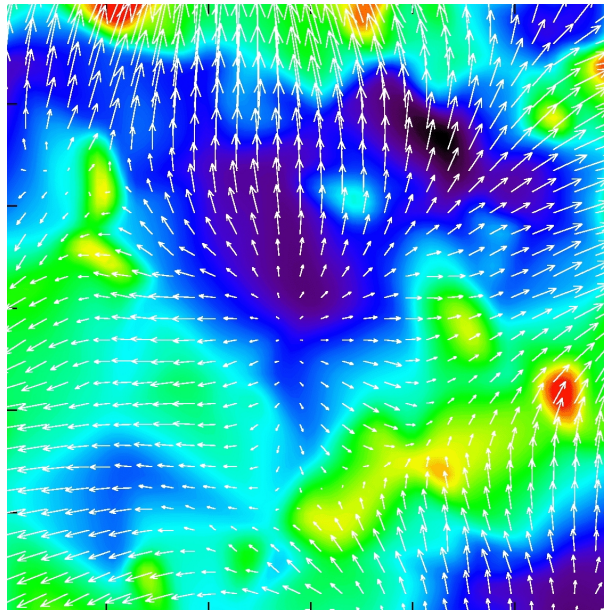


Figure 1.4: The sculptor void from the the PSCz survey. The colors show the interpolated density field and the arrows indicate the velocity field around the Sculptor void. Well recognizable is the large underdense spherical hole (blue), which is surrounded by high dense regions shown in green and red. Also note the nice outflow pattern out of the void. The image was obtained from E.Romano-Diaz (2004) and made with the DTFE method of Schaap et al().

are sometimes referred to as supervoids, to discern them from their smaller counterparts, which have an average size between the 20 to 50 h^{-1} Mpc scale. Voids are often defined in two ways, either by empty regions devoid of non-void galaxies, or by connected underdense regions in the density field. In both cases voids need not to be completely empty, although this criterion is sometimes also used.

Deep observational studies of individual voids have been carried out for several large voids and at several different wavelengths (Cruzen et al 1997,2002, Grogin & Geller 1999,2000, Lindner et al. 1996, Szomoru et al. 1996 (So96)). So96 performed a HI survey study of the Boötes void and found that void galaxies are unaware that they live in a void (see below for further discussion). They also found that the void-galaxies lie in a wall like structure. This might be an indication for the void hierarchy in the Boötes void. A study of the Northern Local Void (NLV) by Lindner et al (1996), showed that the NLV as outlined by clusters seems to be further subdivided by the galaxies into smaller voids. They claimed that it has a void hierarchy with less massive objects.

The confirmation that the LSS has a supercluster-void bubble like topology came with the CfA redshift survey (deLapparent et al 1986) and this reached sufficient depth to start the study of the void ensemble and use voids as a statistical tool to study the LSS see Vogeley et al (1991). The main statistical tools to study the LSS involving voids and void galaxies are Nearest-Neighbor analysis, the Void Probability Function/Underdense Probability Function, topological/shape measures and the void-void correlation function, recently introduced by Colberg et al. (2004). The study of the void-size spectrum has been carried out by many authors and for different surveys (Kauffmann & Fairall (1991), El-AD & Piran (1997) SSRS2+IRAS, Hoyle & Vogeley (2002) (HV02) PSCz+UZC, Plionis & Basilakos (2002) PSCz+IRAS, Hoyle & Vogeley (2004) (HV04 2dFGRS). The main conclusion about the void size distribution of these studies can be summarized as follows. The average void radii varies from around 10 h^{-1} Mpc to around 20 h^{-1} Mpc . This difference may be due to the fact that the typical size of a void

depends on what kind of definition for a void is used, and on the particular search method which is employed. For example, voids defined by the absence of wall galaxies inside a void (VOIDFINDER method) retrieve a very low density contrast inside the voids, probably indicating that only central region of the void is found (HV02). Furthermore the shape of the void distribution has not been determined very well due to a sparse sampling of the void distribution. Some studies indicate a peaked distribution (Kauffmann & Fairall 1991), while others claim that it has a Schechter function like behavior within the observational limits, HV02. The most recent research have focused on the large dataset of the 2dFGRS surveys. The study of voids in the 2dFGRS by HV02 concluded that voids have an average radius of at least $15 h^{-1}\text{Mpc}$, as they retrieve only the inner parts of the voids.

1.2.2 Galaxies in Voids

As was pointed out by Peebles(2001) the Standard Model of Cosmology CDM has several shortcomings. Among it the standard model predicts a measurable population of void dwarf-galaxies. Also Numerical studies point out that there should be halos in voids, be it that compared to overdense regions they should be less massive. The underlying question is how much mass there is in voids and in what kind of objects it resides. Many possibilities exist for this hypothetical void population. They either could be low surface brightness galaxies or dwarf irregular. Another possibility could be that the matter resides in primordial gas clouds. Observational work of voids has not found a population of typical void galaxies. Moreover the ones that do lie inside voids seem to be of average type. This *void-phenomenon* was also confirmed by Peebles(2001), using Nearest-Neighbor statistics between two types of galaxies. It was shown that most of the possible candidates respect the same voids as normal spiral galaxies do, in effect excluding these as the void population. So it seems that voids are indeed very empty and devoid of most matter.

An analysis of about thousand void-galaxies selected out of the SDSS survey (Rojas et al. 2004a,b) shows that void-galaxies are bluer and more disk-like than wall-galaxies. The spectral properties show that this is due to the higher star-formation rate in galaxies that reside in voids. Using N-body simulations and semi-analytical modeling (Benson et al. 2003, Mathis & White 2002, Gottlober et al. 2003) have studied the evolution of matter in voids. They looked whether the simulated voids, defined by the mock galaxies have the same properties and are as empty as observed. Mock galaxies seem to have the correct Void Probability Function according to HV04, and according to Croton et al. (2004) it is well fitted when galaxies cluster like a negative binomial model.

The “observational” properties of mock galaxies (Color,SFR, etc) also confirm that void galaxies should be bluer and have high star formation rates. Voids defined by the galaxies as retrieved from semi-analytical models produce regions that at least out to a scale of $10 h^{-1}\text{Mpc}$ are completely empty. However, whether this is sufficient to produce the voids that are large enough remains to be seen. The provisional conclusion is that there should be some process in the early Universe that prohibited the formation of galaxies in the inner parts of voids. This could be explained either via the baryonic process, such as supernova, winds or ionization suppression. A recent study by Hoeft et al(2004) showed that this latter effect alone is too weak to explain the void suppression. Another consideration might be that the overall cosmological model (possibly WDM) needs to be altered, to get less power on the small scales.

1.2.3 The Evolution of Voids

Voids are assumed to originate from minima in the initial density field. Newton’s second theorem states that in spherical symmetry only the matter within a shell determines the force felt by the shell. Therefore in the case of a minima, which is underdense at some scale, this region will have a net gravity deficit. This results in an outward gravitational force, and therefore matter will begin to stream outwards. As matter leaves the void toward its edge, the internal density

will further decrease. Within this general outflow pattern at least three important dynamical features of void evolution can be discerned, see chapter 2 for more details. The outflow will set up a tophat density profile, tends to make the void more spherical and mass accumulates around the edge of the void, forming a dense ridge. The formation of this ridge marks the stage that the void evolution goes non-linear and often this is taken as the moment that a void becomes an object, which is similar to the moment of full collapse for overdensities.

As noted above for hierarchical models smaller objects merge into larger objects, and voids have a similar behavior. Dubinski et al (1996) analyzed the void merging process in N-body simulations starting out with an idealized minima configuration. This resulted in a picture where neighboring voids expand and as they go non-linear they would collide. The matter in between colliding voids would form a wall like structure. Such walls also have an outward flow pattern in the plane of the wall, thus perpendicular on the line connecting the voids. Regös & Geller (1991) pointed out that the overdensity of this wall is a measure of the state of merging. As the wall streams empty the colliding voids will gradually merge into a larger one. The walls of these previous generation will gradually fade away and remain as substructure. Van de Weygaert & van Kampen (1991,1993) studied this in a more general context and qualitatively found that this concept also applied to voids in a general Gaussian field. This evolution is called the *Void-Hierarchy*. An evolution pattern in which small voids merge together to form larger encompassing voids and the smaller predecessors remain visible as subvoids. The dividing walls between the previous generation of voids remains as substructures, which gradually fades away. Quantitative description of this process has been rather limited, although attention to this issue is increasing, see Colberg et al.(2004).

The study of voids is thus not only from the cosmological aspect interesting, as this might provide ways to discriminate between various models, but also from a galaxy formation point of view voids can place constraints on formation histories. Recently a new aspect of the void population was uncovered by Sheth & van de Weygaert (2004), which indicated that small voids in a general field could collapse if they are embedded in larger overdensities. The problem was translated in the excursion set model and showed that the void distribution is peaked around a typical void scale.

1.2.4 Outline

The goal of this study was to test this void collapse in the context of N-body simulations. This paper is organized as follows; in the first two chapters we will show the background behind the void distribution model of Sheth & van de Weygaert (2004). In chapter four the set of N-body simulations of large constraint voids is explained, and are analyzed. These simulations drew our attention to the boundary of large voids, there it seems that large voids may have a strong impact on the small void population. In chapter 5 we propose a new tool to extract these small voids in N-body simulations, in order to follow their evolution. As a first application of this method we apply it to a 2d and the semi-2d field. In upcoming work this method will be applied to the full three dimensional set of simulations in order to extract the small scale collapsing void population.

Chapter 2

Isolated void evolution: the spherical case

Before tackling the evolution of voids in a general fluctuation field, a brief review of the evolution of an isolated spherical underdense perturbation is presented. In some sense the evolution of an underdense region resembles that of a time reversal of an overdense fluctuation. It will expand in a comoving frame and while overdensities amplify any asphericity, voids become more spherical. Overdensities first grow linearly, then turn-around and begin to collapse. Before they would have been totally collapsed, dissipative processes will start and virialize the halo. By contrast voids only expand and the stage of maturity can be defined on the moment of ‘*shell-crossing*’. This may be intuitively understood by the following analogy. The outward force felt by a test-particle increases toward the center of the void as in general the mean internal density diminishes towards the center. Hence there will be a point in time when inner shells take over the outer ones. From that point on the evolution is no longer a simple redistribution of matter over increasing shells. This thus indicates the moments when non-linear void evolution begins.

A standard FRW-Universe is assumed, with an average density $\bar{\rho}$, which is related to Ω_0 via the critical density

$$\Omega = \frac{8\pi G\bar{\rho}}{3H^2}. \quad (2.1)$$

Furthermore we assume that the Universe is totally homogeneous, except at $r = 0$ where an underdense perturbation ($-1 < \delta < 0$) is located. Let δ denote the density contrast with respect to the average density of the Universe, i.e.

$$\delta(r) = \frac{\rho(r) - \bar{\rho}}{\bar{\rho}}. \quad (2.2)$$

Since a spherical perturbation is assumed, the goal is to derive the radial expansion of shell, $r(r_i, t)$, at any time, t . Here r denotes the physical distance, which is the comoving distance x multiplied by the scale factor, $a(t)$. The evolution of a shell in the spherical symmetric case depends only on the mean density within the shell and on its initial velocity. The mean density within a shell can be written in terms of the density contrast

$$\Delta(r, t) = \frac{3}{r^3} \int_0^r \delta(r', t) r'^2 dr'. \quad (2.3)$$

The equation of motion for a spherical shell of mass M , with radius r are

$$\frac{d^2 r}{dt^2} = -\frac{GM}{r^2}, \quad (2.4)$$

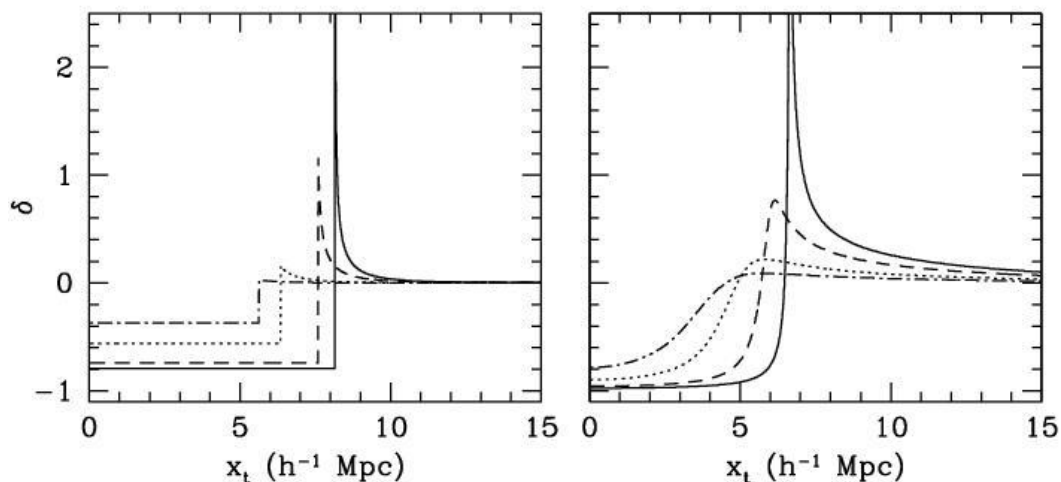


Figure 2.1: The evolution of two different underdense voids.

with M defined as

$$M = \bar{\rho} \left(\frac{4\pi}{3} r^3 \right) (1 + \Delta). \quad (2.5)$$

The first integral of motion is,

$$\frac{1}{2} \left(\frac{dr}{dt} \right)^2 - \frac{GM}{r} = E \quad (2.6)$$

Substituting this in equation(2.5) and replacing the average density in this equation by Ω (eq(2.1)) yields

$$\left(\frac{\dot{r}}{Hr} \right)^2 - \Omega(1 + \Delta) = E. \quad (2.7)$$

The solution to these equations depends on the value of E , which itself depends on the initial velocity and on the initial depth of the perturbation, resp. the first and second term in the above expression. The solution to equation 2.4 is the familiar cycloid solution, i.e.;

$$\begin{aligned} \mathcal{R} &= A(1 - \cos(\theta)), & t &= B(\theta - \sin(\theta)) & E > 0 \\ \mathcal{R} &= A(\cosh(\theta) - 1), & t &= B(\sinh(\theta) - \theta) & E < 0. \end{aligned}$$

Where \mathcal{R} is the scaling factor, akin the cosmological one, of the initial physical radius, r_i to the radius at time t , $r(t(\theta))$. The factor A and B are related via equation (2.4) and eq.(2.7). The evolution of the mean internal density before shell crossing is just the scaling of the initial one with the expansion of the Universe and the void, thus

$$(1 + \Delta) = (1 + \Delta_i) \frac{1}{\mathcal{R}^3} \frac{a}{a_i}. \quad (2.8)$$

From this equation we see that the density contrast increases, i.e. Δ becomes more negative within the shell. Because matter is redistributed over a larger volume, thereby lowering the mean central density. Another consequence of such an expansion is that internal variations are smeared out over an ever increasing volume. As the differential outward directed peculiar acceleration is stronger as one goes inward. The inner shells move out faster, this will set up a flat inner profile. Furthermore the void velocity profile is characterized by an increases with

distance from the center of the void. This velocity profile is for obvious reasons called the 'Super-Hubble' flow. In case of a pure top-hat profile is characterized by a steep ridge, this may also form if the differential acceleration at the edge of the void is sufficient. However, before such a ridge can form, inner shells near the boundary have to take over outer shells, i.e. shells have to cross.

The moment of *shell-crossing* can be found by calculating when the distance between two initially adjacent shells is zero. For a top-hat model this happens at the steep boundary. Therefore, after *shell-crossing*, shells begin to accumulate at this boundary position, these in turn form the steep ridge, see figure(2.1). By equation (2.8) it is seen that for any decreasing profile the average density inside the shell diminishes as the void expands. Matter will thus always accumulate towards the outside of the void. However whether a steep ridge will form, is rather sensitive to the steepness of the profile. If the profile is not steep enough, the differential acceleration is too small to bring enough shell towards a boundary to form such a ridge.

For a top-hat initial underdense profile in an Einstein-deSitter Universe ($\Omega = 1$ and $\Lambda = 0$), *shell-crossing* happens when the development angle θ_{sc} is about 3.5. Time evolution of a density perturbation can also be expressed with the value of the linear extrapolated density contrast. This value represents the density contrast at that particular moment if it would just have grown linearly,

$$\delta(x, t) = D(t)\delta(x, t_0), \quad (2.9)$$

where $D(t)$ is the linear growth function that depends on the particular cosmological model. For shell-crossing, this linearly extrapolated density contrast (thus not the real value of *delta*!) has reached a value of $\delta_v = -2.81$. At this moment the void has grown a factor 1.7 in comoving space. This is analogous to the evolution of haloes, which collapses around a linear extrapolated delta of $\delta_c = 1.69$. Using the fact that in an Einstein-deSitter Universe the linear growth factor is proportional to the expansion factor a , the corresponding redshift of *shell-crossing* is thus

$$1 + z_v = |\Delta_{lin,0}|/2.81 \quad (2.10)$$

In summary, the evolution of an isolated spherical void can be characterized by the following phases:

(1) **Expansion** of an initial underdense fluctuation w.r.t the background, and a subsequent **decrease** of the density due to the expansion of the void. This expansion is more effective along the shortest axis of any asphericity. A void will thus become more **spherical** as it evolves.

(2) The inner regions will flatten due to the expansion, i.e. the profile will become like a reversed **top-hat**. Due to this inner flattening the gravitational force increases with distance. This in turn will set up a **super-hubble flow**. The opposite happens near the boundary where outer shells are overtaken by inner shells, the **shell-crossing** phase, which characterizes the transition from linear to non-linear evolution. Moreover if the initial profile was steep enough, also a **ridge** may form near the boundary.

This description is only valid in the very idealized case of spherical symmetry. In a general fluctuation field distortions from fluctuations within the void as well as outside the void may seriously distort this model. The first is called the substructure of the void, which originates from the previous generation of voids and haloes from which a void has evolved, also referred to as the 'void hierarchy'.

The second are large overdense and underdense regions at the boundary of the void. The overdense regions will cause an infall towards it, thereby increasing the outflow in the void. While the second will be more like a collision of two regions diminishing the total expansion of the void. Although both seriously reshape the outer boundary of the void the overall evolution of the top-hat evolutionary model can still be identified in the general case (van de Weygaert

and van Kampen 1993 and here below). Mainly this is due to the fact that voids will become more spherical and generate a top-hat profile. Both cause a simplification of the situation in time. Note that this argument will only be valid for voids which are at that particular moment of the typical scale, and not for small scale voids. The evolution of the smaller voids is closely related to the evolution of larger scales.

Chapter 3

The Excursion Set Model of Void Evolution

One of the first attempts to explain the physical origin of the matter distribution of non-linear clumps was made by Press & Schechter (PS hereafter). This model is based on a description of clumps which are formed through the consecutive merging of smaller clumps. In a hierarchical model the fluctuations on the largest scales are on average the latest to appear, and they must then be built up from smaller clumps.

The basic principle of the excursion model is that smoothing at ever increasing scales around a certain position in the **initial** Gaussian field, one can separate various clumps. A record for the average density at each scale can be made, that is centered at that same position. This record will yield a jiggly track, that has most amplitude when the filter scale is of the same size of an object that emerges out of these fluctuations. The merging evolution of the matter may be predicted. Because scales with high amplitude are associated with clumps of that scale. The general underlying assumption is that a sphere with a particular over or underdensity in the initial field has formed when the linear extrapolated value crosses a certain value δ_c or δ_v . This crossing value is most frequently based on the isolated spherical tophat model as described above.

3.1 Press-Schechter model of haloes

The Press-Schechter model can be described as counting objects in the primordial field at each smoothing scale. An object is defined as a region in the initial Gaussian field that has an linear extrapolated (see eq. 2.9) overdensity larger than δ_c at filter scale R_f . Thus the distribution $N(> M)$ is found by integrating the probability of the initial linear extrapolated gaussian density field larger than the boundary, δ_c at a given smoothing scale. The probability of finding a value δ at some location when the field is smoothed at scale R_f is

$$P(\delta|R_f) = \frac{1}{\sqrt{2\pi\sigma(R_f)^2}} \exp\left(-\frac{1}{2} \frac{\delta^2}{\sigma(R_f)^2}\right). \quad (3.1)$$

$$\sigma(R_f) = \int \frac{d^3k}{2\pi^3} |\delta_k(t)|^2 W_k(R_f) \quad (3.2)$$

Where W_k is the fourier transform of the filter function. The conditional probability for the smoothed field being larger than δ_c (or mass if the conversion via the volume is known) is

$$P(\delta > \delta_c|R_f) = \frac{1}{2} \left[1 - \operatorname{erf}\left(\frac{\delta_c}{\sqrt{2}\sigma(R_f)}\right) \right]. \quad (3.3)$$

This is the fraction of the Universe which is in collapsed objects with mass $>M$, or also called $F(> M)$. To get the number of objects in a mass range dM , equation (3.3) has to be differentiated with respect to the mass(or radius) and deviding through $M/\bar{\rho}$ to get the mass number function $f(M)dM$

$$f(M)dM = \frac{\bar{\rho}}{M} \frac{dF(> M)}{dM} \quad (3.4)$$

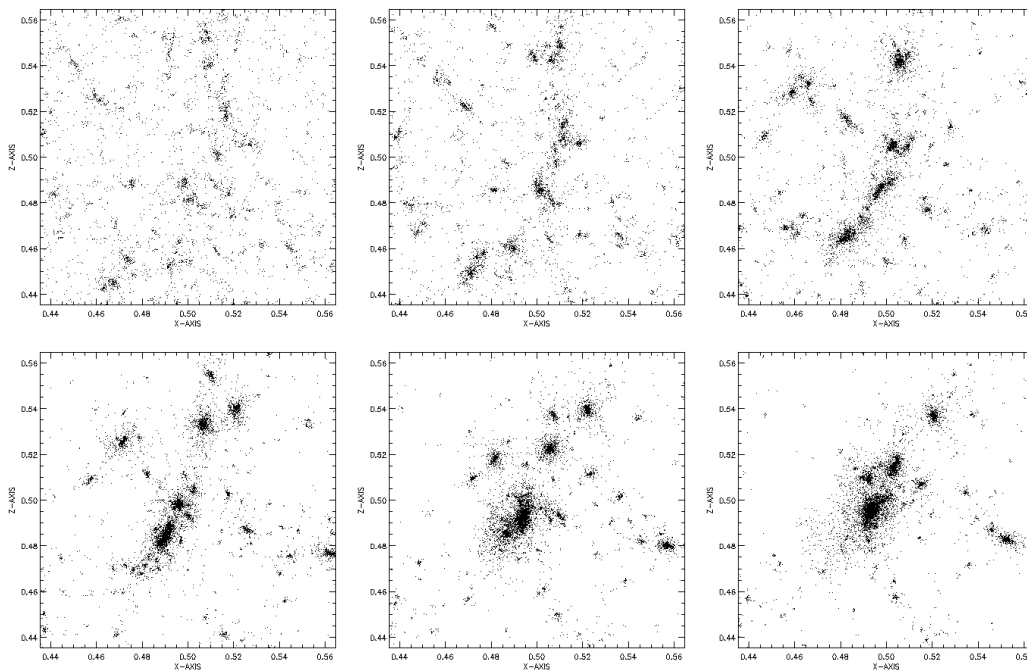
$$f(M) = -\left(\frac{\bar{\rho}}{M}\right) \frac{1}{\sqrt{(2\pi)}} \left(\frac{\delta_c}{\sigma^2}\right) \left(\frac{d\sigma}{dM}\right) \exp\left(-\frac{\delta_c^2}{2\sigma^2}\right) dM. \quad (3.5)$$

The time evolution of the Mass function is completely contained in δ_c , which start out high since the largest overdensities are the first to collapse and with time it moves down.

3.2 Excursion Sets

The PS-model (3.5) as described above has unfortunately one flaw, only half of the mass is accounted for! This can be seen by substituting $\delta_c = 0$ in equation (3.3) this should give all the mass of the Universe however it gives only half. The physical reason is that by smoothing at scale R and then counting everything all mass above δ_c , we neglect everything that is larger than δ_c only on scale larger than R . These regions should be accounted for equation(3.3).

A possible solution, as given by Bond et al (1991), is by smoothing the field with a whole set of radii and for each radius keeping track of the value of δ for every smoothing radius. If started out with a very large radius by homogeneity of the Universe, delta is zero. Letting the smoothing radius decrease, at one point some overdense regions at radius R can upcross δ_c , letting the radius decrease further then different regions might also begin to cross the barrier, however some regions that have crossed the barrier can drop below the barrier again and subsequently upcross it again at an even smaller radius. It is exactly this behavior that was not accounted for in the original PS-model. Since the first upcrossing represents the largest sphere of matter around point \mathbf{x} that has collapsed, any other upcrossing at smaller scale should not be counted



as an object. This is the very well known *cloud-in-cloud* problem, and a correction term is in need for this double counting.

Mathematically the problem is described by the chance that a random walk process starting at zero first crosses the object barrier at a certain distance from the origin, see fig(3.2). However doing this calculation is difficult, especially for gaussian and top-hat filters as these retain the memory over all the previous radii, meaning that to calculate the crossing probability depends on all the previously calculated probabilities. A different way to tackle it is by using the sharp \mathbf{k} -space filter, this has the advantage that the next calculated value in the random walk only depends on the last one calculated. Such a random walk is called a Brownian random walk and probabilities for such systems are known. Namely the distribution of trajectories that at resolution scale R have not pierced the barrier at δ_c is, see 3.2;

$$\frac{dP_s}{d\delta} = \frac{1}{\sqrt{(2\pi\sigma)}} \left[\exp\left(-\frac{\delta^2}{2\sigma^2}\right) - \exp\left(-\frac{(2\delta_c - \delta)^2}{2\sigma^2}\right) \right] \quad (3.6)$$

The shape of this distribution is show in figure(3.2) and integrating this from minus infinity to δ_c yields the total survival probability i.e. the fraction of trajectories that are not yet absorbed by the barrier at δ_c at radius larger than R_f (or at lesser σ as R_f and σ may be interchanged via eq(3.2))

$$P(\delta < \delta_c | \sigma(R_f)) = \int_{-\infty}^{\delta_c} \frac{dP_s}{d\delta} d\delta = \frac{1}{2} \left[1 + \operatorname{erf}\left(\frac{\delta_c}{\sqrt{2}\sigma}\right) \right] - \frac{1}{2} \left[1 + \operatorname{erf}\left(\frac{-\delta_c}{\sqrt{2}\sigma}\right) \right] = \operatorname{erf}\left(\frac{\delta_c}{\sqrt{2}\sigma}\right). \quad (3.7)$$

Therefore $1 - P_s$ is the probability that the trajectory already was absorbed and comparing this result to eq(3.3), we see that this has yielded exactly a factor two for the distribution of objects with mass $>M$ ($F(> M)$), and in the same language the differential of this fraction is the rate at which trajectories first up-cross (read objects!) the halo barrier. So the random walk treatment of successive smoothing the initial gaussian random field has yielded the correct prefactor. In the same manner as the previous section, F can be differentiated and plugged into eq(3.5) to obtain

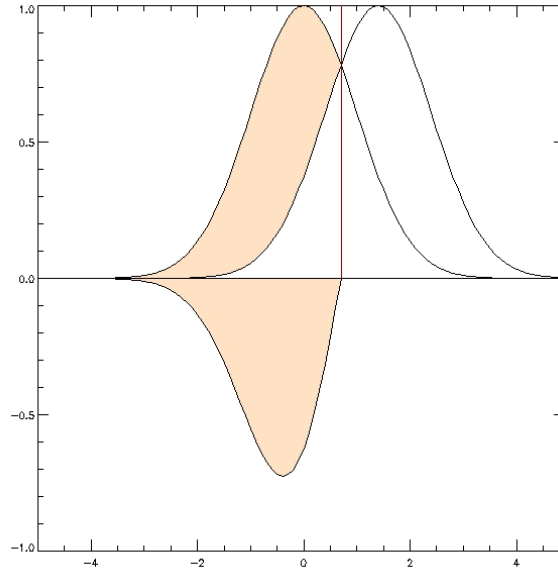


Figure 3.1: The survival distribution

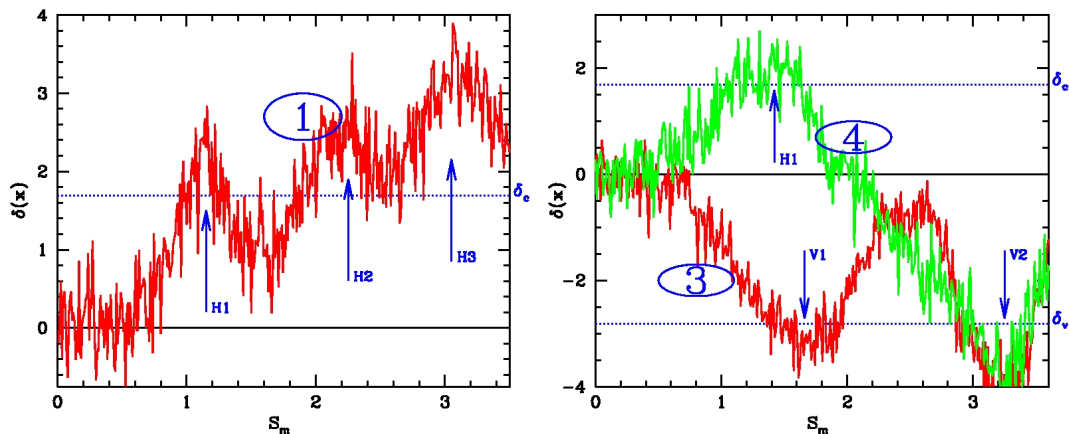


Figure 3.2: The right hand figure shows an excursion set track in the *cloud-in-cloud* mode. The resolution is plotted versus density contrast. As resolution is the inverse of scale, the radius decreases to left to right. The merging evolution around this point can be understood if one would sweep the horizontal line from the top downwards. The barrier is then first up-crossed at the peak located at H3, meaning that a halo of that particular scale has collapsed. Thereafter the next up-crossing is at H2, which means that by then the H3 clump has merged into the H2 clump. Successfully, the H2 clump merges with the H1 clump. The left hand side shows, two excursion set tracks in the two barrier problem in the case of voids. The red one represents the *void-in-void* mode and evolves in the same manner as the *cloud-in-cloud* mode on the right. Where first a small void at V2 forms, which is later on is contained in the void at V1. The green line however shows a mode which is unique to voids. Here the void more or less evolves like the V2 void of the red track, but when the collapse barrier has sunken to the point that it crosses at H1 the void has collapsed.

the number density distribution of haloes, which gives the Press-Schechter formula with correct factor two. Further extensions of this formalism can be made by incorporating different kinds of barriers, which can grow differently according to the geometry of the fluctuation, most notably the ellipsoidal collapse model Sheth & Tormen, or the cosmological background, or the overall growth rate may depend on larger scales. For example a halo in a void develops slower than one situated inside a large overdense region, this can all be incorporated in the barrier shape and time-evolution of it.

3.3 The Void Distribution

In this section we turn the attention to the hierarchical evolution of the void population. Sheth and van de Weygaert(2004) (hereafter SW04) showed how to incorporate the hierarchical void evolution in the excursion set model. A short overview of the main characteristics of this model is presented below.

Just as for clumps we can identify a void when it has sufficiently grown, in order to call it an object. For haloes this choice was made by considering the object as a spherical top-hat perturbation and calling it an object when the linear extrapolated value reached an overdensity of $\delta_c = 1.69$. Similarly for voids the most natural choice for this threshold is when the linear extrapolated underdensity has reached a value of $\delta_v = -2.81$.

So one could expect that the void distribution can simply be predicted by just plugging in

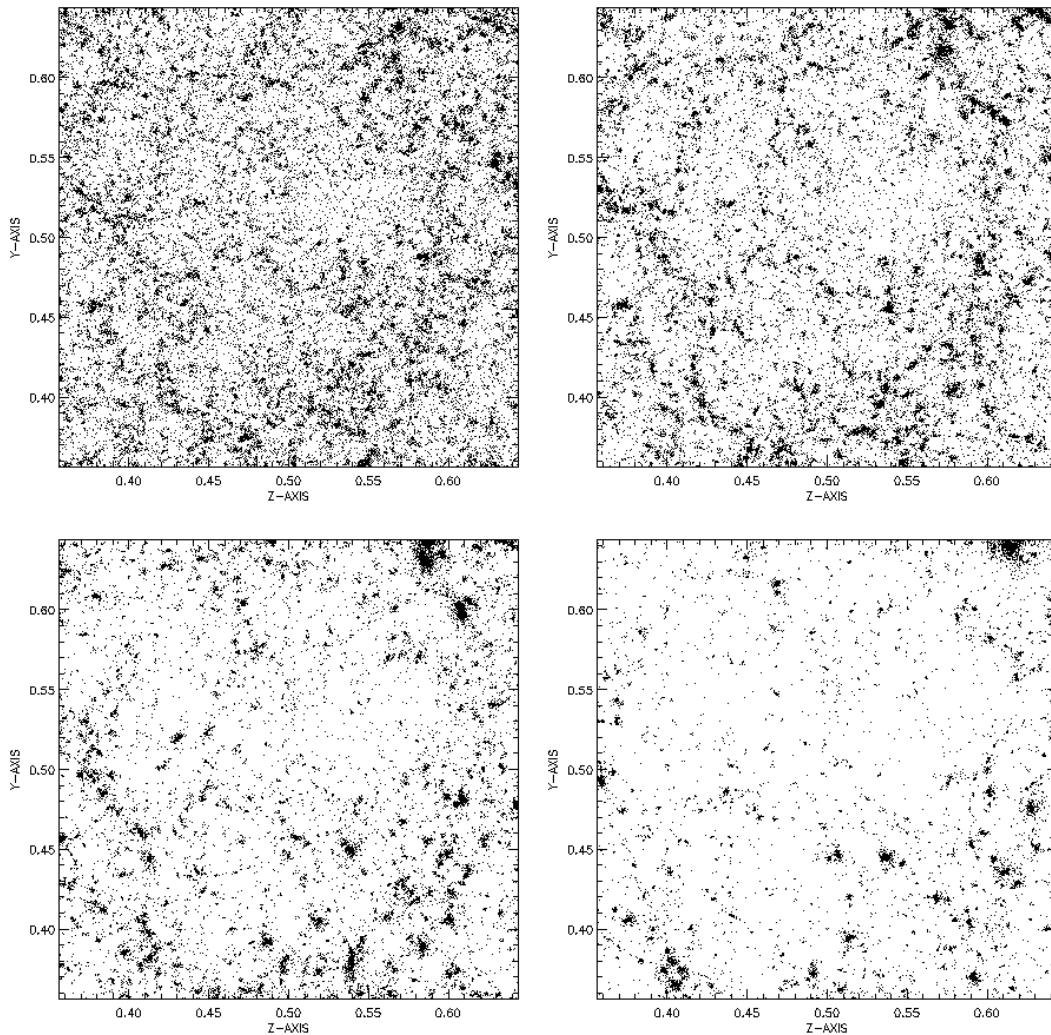


Figure 3.3: A zoom in on a region within a larger void, this shows that there are various underdense region a substructure within a large voids. These smaller voids have build up in the larger voids which is clearly seen in the last picture. This build up is called the void hierarchy and is accounted for in the excursion set model with the *void-in-void* mode.

the void threshold, δ_v , in equation(3.5), however this can not be justified, as a fundamental difference arises between the evolution of voids in comparison to that of haloes. In a hierarchical model small structures form earlier than larger ones and smaller structures merge to form larger ones, i.e. large structures are never independent from the smaller ones, as it are the latter that are the predecessors of the former. This evolution for haloes, the *cloud-in-cloud* problem, was solved above by correcting for the various up-crossings that may have ocured at larger scales.

A direct translation of this problem can be made for voids and is called the *void-in-void* problem. In terms of excursion tracks this is a walk that crossed the void-barrier more than once at a two given scales, and only the largest down-crossing has to be taken into account, an example of such a track is depicted in the right picture of figure(3.2). This thus represents a void which has formed by the merging of smaller voids, which is just what to expect in a hierarchical structure formation scenario.

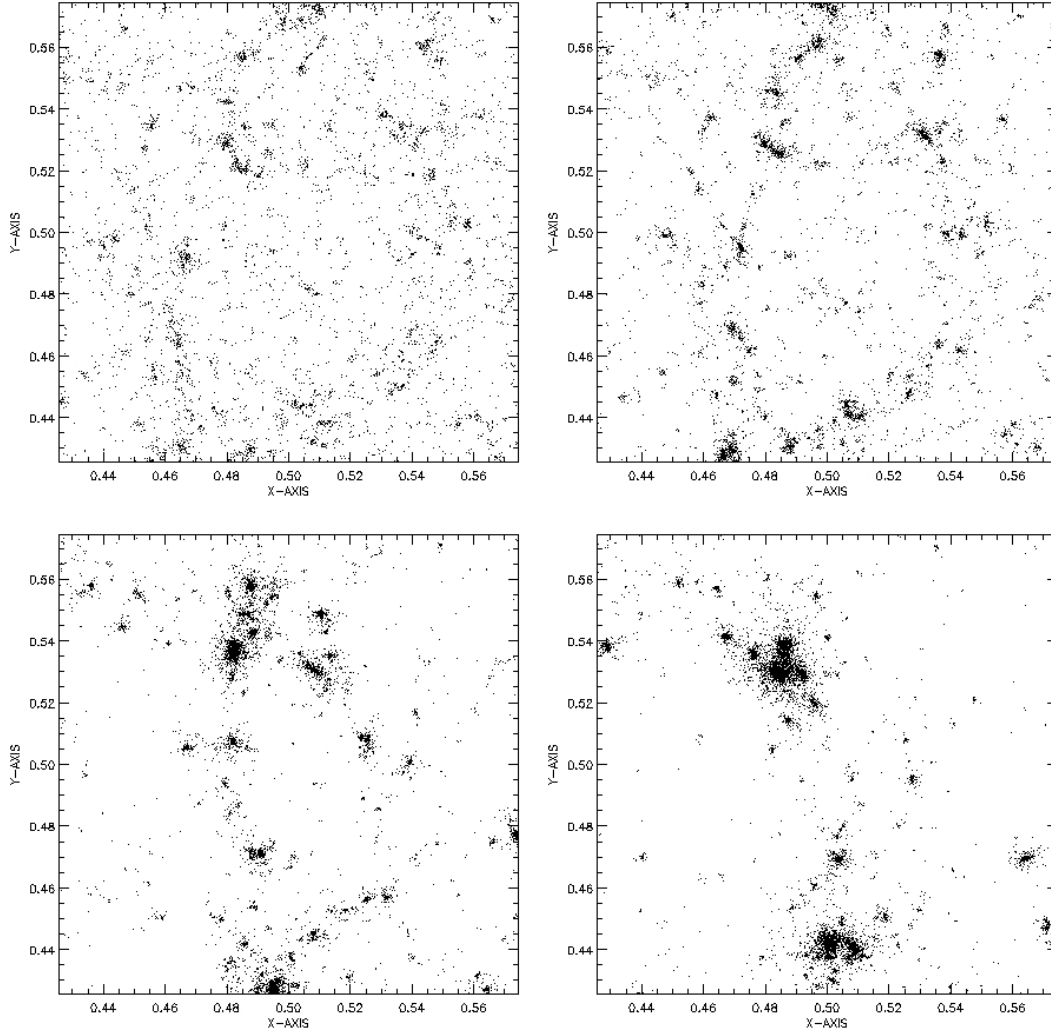


Figure 3.4: The plots show a four consecutive snapshots of a region in a larger simulation of a small scale void which has collapsed into a filamentary structure.

The difference occurs when tracks cross both barriers, that is the halo and the void barrier. Consider a small halo which forms in a large void, the excursion track would first cross halo-barrier and the track would cross the void barrier at larger scale. As the large scale void has on average less amplitude it would emerge later and by then a halo would have completely collapsed and except that it would experience less or no afterward merging (starvation), the clump would be unaffected by the fact that it is embedded in a large void. This is called the *cloud-in-void* and such a track has first an up-crossing at small scales and at larger scales a down-crossing of δ_v . In stark contrast is the situation of a small-scale void embedded in a large overdense region. Here the small void would form but at a certain later time the large overdensity would begin to collapse, taking with it the smaller void. This process is called the void-collapse and it is associated with a *void-in-cloud* excursion track, this is also shown in figure(3.2) with the green track. It is characterized by first having a down-crossing at small scales of the void-barrier and thereafter at a larger scale an up-crossing of the halo-barrier.

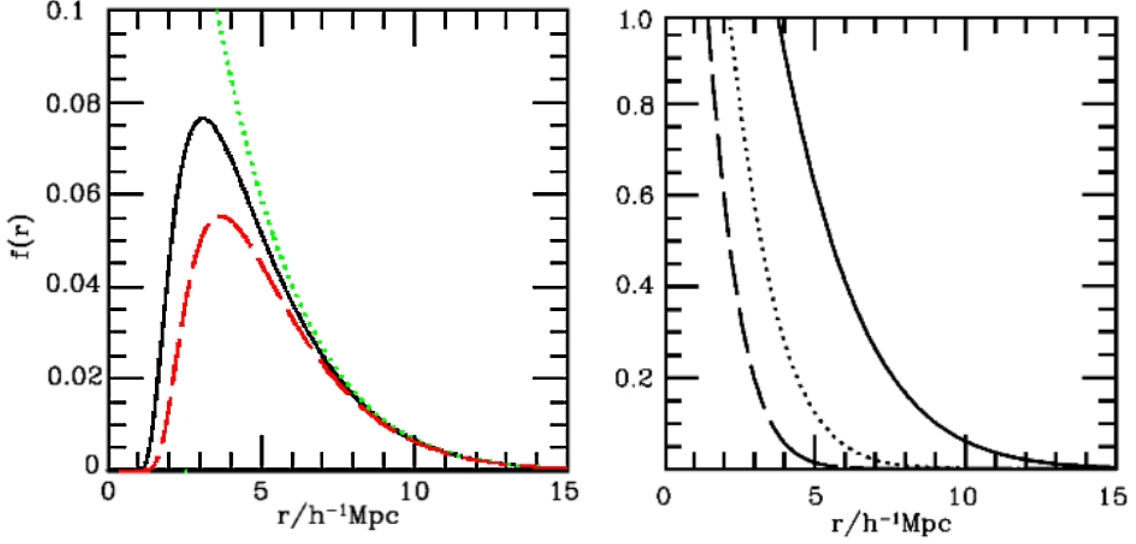


Figure 3.5: The left figure shows the void distribution, for three different choices of δ_c . The green corresponds to a choice of infinity, thereby ignoring the *void-in-cloud* mode. This immediately shows the divergent small scale tail, as also known from the Press-Schechter formula. The black and red line represent a choice for the collapse barrier of respectively 1.69 and 1.06. According to the spherical model these are the linear extrapolated overdensities for which the halo will be either fully collapsed or would just begin to turn around. Only the small scales are affected by these choices. The right figure shows the fraction of volume taken in by voids larger than R . The three different lines are for three different times, resp. $z=0$ (solid), $z=0.5$ (dotted) and $z=1$ (dashed). Voids always fill the Universe as for all the three times they cross unity.

This qualitative description of excursion tracks shows that any model of the void-distribution should take the *void-in-void* as well as the *void-in-cloud* into account, and instead of having a one-barrier random walk problem it has become a two-barrier problem. Here the only tracks of interest are those that first down-crossing the void barrier AND that did not had any up-crossing of the halo-barrier at larger scales. Up-crossings may thus only occur at smaller scales than that of the void-scale, because that would just be the *cloud-in-void* situation, which leaves to a certain extent both the void and the halo unaffected.

SW04 calculated the probability of this conditional first down-crossing and retrieved an approximation for the void mass distribution;

$$\frac{dF(\sigma)}{d\sigma} = \sqrt{\frac{\delta_v^2}{2\pi\sigma^2}} \exp\left(-\frac{\delta_v^2}{2\sigma^2}\right) \exp\left(-\frac{|\delta_v|}{\delta_c} \frac{D^2 \delta_v^2}{4\sigma^4} - 2\frac{D^4 \sigma^4}{\delta_v^4}\right), \quad (3.8)$$

where D is the *void-in-cloud* parameter

$$D = \frac{|\delta_v|}{(\delta_c + |\delta_v|)}. \quad (3.9)$$

If D goes to zero than the second term on the right vanishes, which leaves us with the same formulation as above for haloes. With eq(3.8) plugged into eq(3.5) we can obtain the void number density, f_v ;

$$f_v = -2 \frac{\bar{\rho}}{M} \sqrt{\frac{1}{2\pi}} \left(\frac{\delta_v}{\sigma^2}\right) \exp\left(-\frac{\delta_v^2}{2\sigma^2}\right) \exp\left(-\frac{|\delta_v|}{\delta_c} \frac{D^2}{4\nu} - 2\frac{D^4}{\nu^2}\right) \frac{d\sigma}{dM} \quad (3.10)$$

The shape of the distribution is shown with the left side of figure(3.5) and it shows that the void distribution is characterized by a peak, this in contrast to the halo distribution which diverges at small scales. The reason for this difference has to do with the asymmetry between the *void-in-cloud* and *cloud-in-void* process. Three choices of the *void-in-cloud* parameter are shown one which ignores the void collapse mode. That is one where $D \rightarrow 0$, this resembles thus the distribution of haloes as it ignores the halo-barrier, which reduces it to a one-barrier problem, and by symmetry of the random walk this means that it has the same shape. Also shown are two different choices of δ_c , with δ_v fixed at -2.81. The lower of these two is a choice for δ_c of 1.06 (turn-around of a clump) and upper one is for a value of 1.69. These choices are inspired on the spherical model and respectively represent the moment of turn-around of the encompassing overdensity and the other is the case where the overdensity is fully collapsed. As may noted from the two graphs for a lower choice of δ_c the *void-in-cloud* parameter increases, thereby increasing the chance that a small void is collapsed away, thus lowering and shifting the void distribution to larger scales. Also note that the large voids are insensitive to the choice of this parameter.

From the void distribution one can obtain the fraction of space filled by voids, by including the fact that void has grown about a factor 1.7 when it reaches the barrier. This is shown in the right side of fig(3.5) for the three redshifts, indicating that void always fill the Universe. Further extension and implications of the models are described in SW04.

Chapter 4

Void N-Body Simulations

In this chapter we want to study the evolution of large voids and are in particularly interested in the surrounding of a void. As WK93 showed these large voids can have a large impact on their surrounding. Several methods have been developed to study large voids, and some of these will be discussed below, however first we shall briefly describe why special methods have to be used to simulate voids.

The study of void evolution with N-body simulations has a large problem. Due to the Lagrangian nature of these codes the density field is represented by particles. These particles can be considered as a Monte-Carlo sampling of the underlying continuous density field. As voids get more underdense in their evolution, particles stream out of the void. Therefore, one naturally loses mass resolution, in the sense that local fluctuations are represented by only a few particles.

Moreover since one has less particles to represent the field, inside a void one is more prone to shot-noise. Usually calculations are performed on a Eulerian grid, therefore one has to interpolated back at a grid. Unfortunately, if there are too less particles or worse no particles in the fixed interpolation volume of a grid point one loses information, i.e. the field is not continuously sampled anymore. To overcome this problem one needs to simulate a void, which is represented with sufficient particles. Note that this shot-noise problem inside voids could be overcome if a more proper interpolation scheme is used, see Pelepusy et al, Schaap & Weygaert(2005) and A.

For the statistics of the void population in a N-body simulations one needs to have a large volume, and as argued at the highest possible mass resolution. This approach was recently taken by Colberg et al.(in prep), by analyzing the void population out of large simulations. In particular those that were run by the Virgo consortium. However if one is interested in the evolution of a individual void, one can not resort to select one from such a large simulations, because the mass resolution is in general too small.

Several solutions are available to overcome this problem. One can select a large voids from an unconstrained simulation and resimulate this void at higher mass resolution, see Klypin(2001). Gottlöber (2003) used such an adaptive mesh refinement technique to study the structure of voids in a Λ CDM Universe. In this scheme the void is simulated at high resolution, while its surrounding is simulated at ever decreasing mass scales. Another approach taken by Goldberg & Vogeley in prep. is to simulate a void by treating the inner regions of a void as a lower dense Universe. In this way one puts the simulation box in the internal regions of a void and one can gain an order of magnitude in mass resolution. Both of these methods have good resolution inside the void, however both neglect the outer boundary of the void.

Dubinski et al.(1993) also studied the evolution of voids with N-body simulations. Their initial fields were configured to have spherical dips at various locations and depths. With this approach they were able to analyze the void hierarchy However these fields were highly sym-

metrical and idealized and are not Gaussian random fields. In the following section it is shown how a field can be made, which has the desired object, yet fully embedded in a Gaussian field, including its statistics.

In this chapter we will study the void evolution with constraint N-body simulations of the dark matter component. In approximately the same approach as was taken by WK93. They studied the evolution of a single constraint void in various cosmological structure formation models, particularly the standard cold dark matter (SCDM), hot dark matter (HDM) scenarios and power law models. The voids had different initial depths, varying from 1,2 and 3 σ_0 dips at the same $10 h^{-1}\text{Mpc}$ scale. In this same manner three power law simulations of constraint voids were run at 2^3 more particles and in a twice larger box, thus effectively at the same mass resolution as WK93. However our simulation box is larger and therefore we are able to make a study of the interaction of a large void with its surrounding. First we shall briefly explain how the initial field was set up. Then we will briefly describe the global evolution of the constraint voids. Finally we shall see how the global evolution of the voids relates to the collapsing void population.

4.1 The Initial Conditions

The initial fields here were made with a Hoffmann-Ribak method Hoffman & Ribak (1991), van de Weygaert & Bertschinger (1996) for generating constrained Gaussian fields, Bertschinger (1987). A Gaussian random field is uniquely characterized by its power spectrum. This spectrum determines the variance of the ensemble of wave amplitudes, for each frequency. The phases of such an initial density field are randomly distributed. The scales represented in a simulation depends on the amount of particles and the size of the box. The largest mode represented in a simulation is the fundamental wave, which has a wavelength twice the boxlength and the smallest wavelength is the Nyquist frequency which is given by the boxlength divided by number of particles. These two wavelengths give the comoving scales that are represented in the initial density field.

Then given a initial power spectrum and a transfer function, which depends on the constituents of the simulated Universe, the power spectrum of the random Gaussian field is given. Then a realization can be made by constructing in Fourier space. Each independent wave has a random phases and an amplitude, that is a random variate taken from a normal distribution with variance as given by the power spectrum.

The constrained realization can be summarized as doing the following. Given a random realization as above can one impose a constraint on such a field. For example, that the field should take a certain value at a certain position, $f(r_i) = c_i$. One could make a lot of realizations, until this condition is satisfied. However this is practically not feasible if the constraint becomes somewhat more complexer.

An more efficient way is to begin with a unconstraint realization, \tilde{f} , and try to impose the constraints, Γ , on this field. Thus one wants to replace in the field certain features with the desired features imposed by the constraints. So what to remove and what to insert? If the constraint is a function of the field at a certain location r_i , then perhaps the first guess would be to evaluate the constraint on the unconstrained field, which yields, \tilde{c}_j . Then replace this found

	Ω	n	Boxsize	N_{part}	H	R_c	δ_c
SimI	1.0	0.0	100	128^3	70	7.0	-3.0
SimII	1.0	-0.5	100	128^3	70	7.0	-3.0
SimIII	1.0	-1.5	100	128^3	70	7.0	-3.0

Table 4.1: The table shows the simulation parameters of the large void evolution.

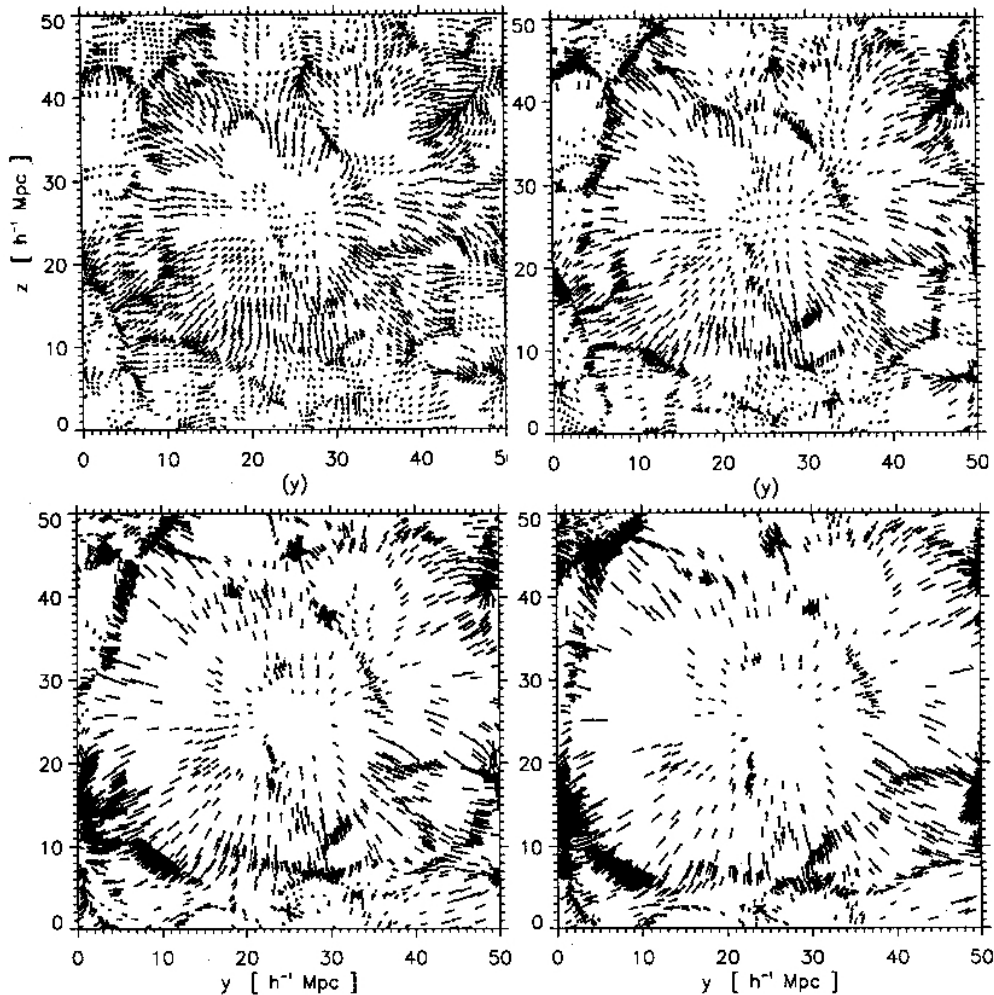


Figure 4.1: The figure shows a the velocity field of 3σ CDM void as made by WK93. These show central slices of the through the box at expansion factors $a=0.2, 0.4, 0.7$ and 1.0 . It clearly indicates the outflow pattern out of the void. At earlier times this outflow pattern is irregular though definitely present, while at later times it completely dominates the velocity field.

value, with the value of imposed by the constraint, c_j . Unfortunately, the result would not be a random Gaussian field, because values at position r_i are not independent from those at r_j .

Therefore, one also needs to remove the correlated contribution of the unconstrained field. This can be evaluated with the constraint functional. And replace this with the correlated values of the desired constraint. These correlations of the constraints are called mean fields and they represent the average field over all the fields that obey the constraint, i.e. $\langle f|\Gamma \rangle$ (see also Bardeen et al. 1986). Van de Weygaert and Bertschinger (1996) showed that this can be evaluated as follows;

$$\bar{f} = \langle f(r)C_i \rangle c_j (\langle C_i C_j \rangle)^{-1} \quad (4.1)$$

Here is f the Gaussian random field, and C_i are the constraints, which take on the value c_i . Then the constrained field, f_c is given by the following equation;

$$f_c(r) = \tilde{f} - \bar{f} + \bar{f}, \quad (4.2)$$

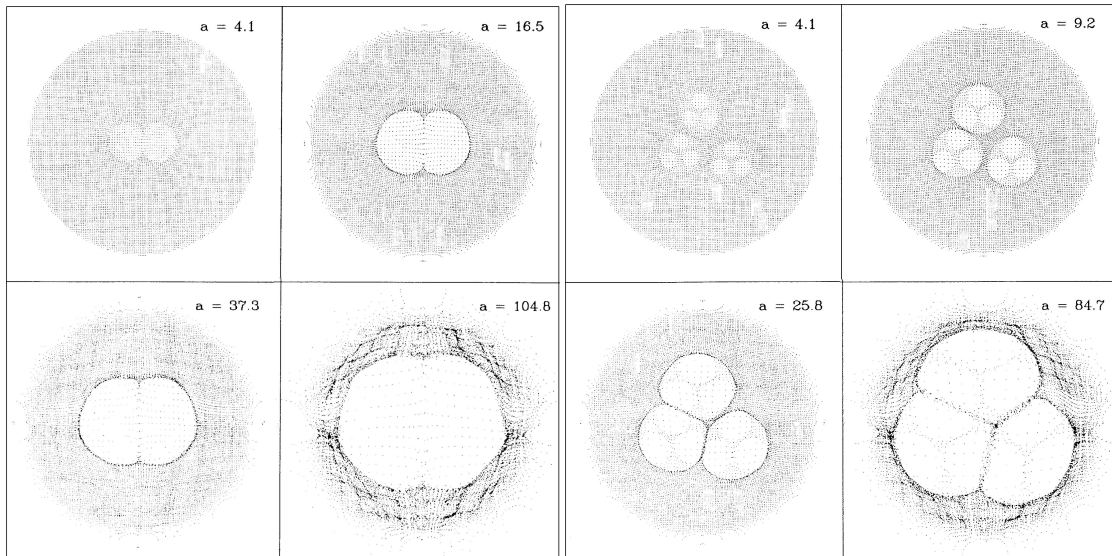


Figure 4.2: The left images show the void merging process between two voids. The voids are positioned such that initially they just meet. Then as the voids expand, matter piles up in between these voids and form a wall. Eventually these voids merge to form one ellipsoidal void, which in time becomes more spherical. Furthermore the wall that separated the voids gradually fades away. The right image shows a build up scenario of a large void from smaller voids. It shows a two level deep hierarchy of voids and each level is distributed at the nodes of an equilateral triangle. It shows that voids merge to form large voids and as the previous generation gradually fades away within the larger void.

Here \tilde{f} is the mean field of the value of the functional evaluated on the unconstrained field, i.e. \tilde{c}_j .

4.1.1 The Powerlaw Voids

The specifications of the simulations and constraints put on them are shown in table 4.1. We imposed one constraint on the initial field. Namely we required that each powerlaw void would have the same dip in the center of the field. That is the void seed in the powerlaw models have the same underdensity $\delta_{in} = -3.0$ and at the same smoothing scale, $R_g = 7.0 h^{-1}\text{Mpc}$. This value was chosen in order that the void would go non-linear at the present expansion factor. As the linear extrapolated underdensity has to reach a value of -2.81 in the spherical case. The three simulations have resp. the following spectral index, $P(k) = Ck^n$ with n equal to 0.0, -0.5 and -1.5. Further cosmological parameters that are used are also given in table 4.1. These are approximately the same as a SCDM structure formation model. All of the simulations have the same initial random phases. The details of the simulation method can be found in the appendix B.

4.2 Global Void Evolution

In figures 4.3, 4.4 and 4.5 the voids are plotted at six different timesteps. The particles are selected from a central slice out of the simulation box. The particles are indicated with the white dots, while the smoothed density field is shown with white/blue/black colors. The density field was smoothed with a Gaussian filter, at a filtering scale of $R_g = 4.0 h^{-1}\text{Mpc}$. And the contour levels are chosen such that they always run from the highest to the lowest density value.

Now we will compare the voids from the three different simulations. The early density fields at for example an expansion factor 0.05 look still very similar. This indicates that the smoothed field at this expansion factor is still linear and therefore does not change its topology. Though the particles already show a markable difference. As expected the $n=0.0$ and $n=-0.5$ show much more small scale clumping in the particles, compared to the $n=-1.5$ simulation. However at $a=0.15$ the $n=-1.5$ shows a clear filamentary pattern, which grows even more in the following times steps. This is in contrast to the $n=0.0$ simulations that remains clumpy throughout the simulation, although roughly the large scale spatial patterns in each simulation can be readily identified between each other. This originates from the trivial fact that the simulations have the same phases and only differ in the amplitudes.

The above characteristics can also be seen in the smoothed density field. Although initially they are almost the same, however the morphology clearly differs in later steps. As can be seen in the $a=1$ smoothed field, the $n=-1.5$ has long filaments embedded in fast underdense regions. This is not the case in the topology of the $n=0.0$ field. This is much less opened up, and is also far more clumpy. The $n=-0.5$ shows a behavior somewhat in between the other two.

The constrained voids in the simulations are seen in the center of each slice. It shows the evolution as described in chapter 2. The voids expand and while in SimI the edge is very clearly visible this is much less so for the void in SimIII. That is because the formation of a sharp edge is very much dependent on the initial profile of the void. If this is shallow, as in the $n=-1.5$ is the case, then no sharp edge will form. The evolution of these radial density profiles was thoroughly studied by WK93, and here we refer to this article for the global evolution of the void.

The void merging evolution can be compared to the generic evolution as shown in figures 4.2, from Dubinski et al. (1993). These figures show respectively the void merging and hierarchy evolution in an $n=-1$ structure formation model. This generic evolution applies to the voids in the constrained simulations too. For example figure 3.3 shows a zoom of the central region of the $n=0.5$ void. Comparing the last plot to the generic void hierarchical case in figure 4.2 shows approximately the same spatial distribution. There are three subvoids, that have merged to form one larger void. This evolution can also be seen in the slices. Most notable is that indeed these subvoids are still visible in the $a=1$ slice, for all spectra. At various other locations in the slices one can see this merging pattern. The dips as identified in $a=0.05$ slice can be followed and show that they end up in larger structures.

However much in contrast to the large scale behavior, is that of the small scale voids. Note that these small scale voids are not visible in the smoothed density field, but can be better identifiable in the particle distribution. Much of the small scale voids are not present in the slices at $a=1$. Therefore in the next section we will try to identify whether these small scale voids also show the merging pattern as described above.

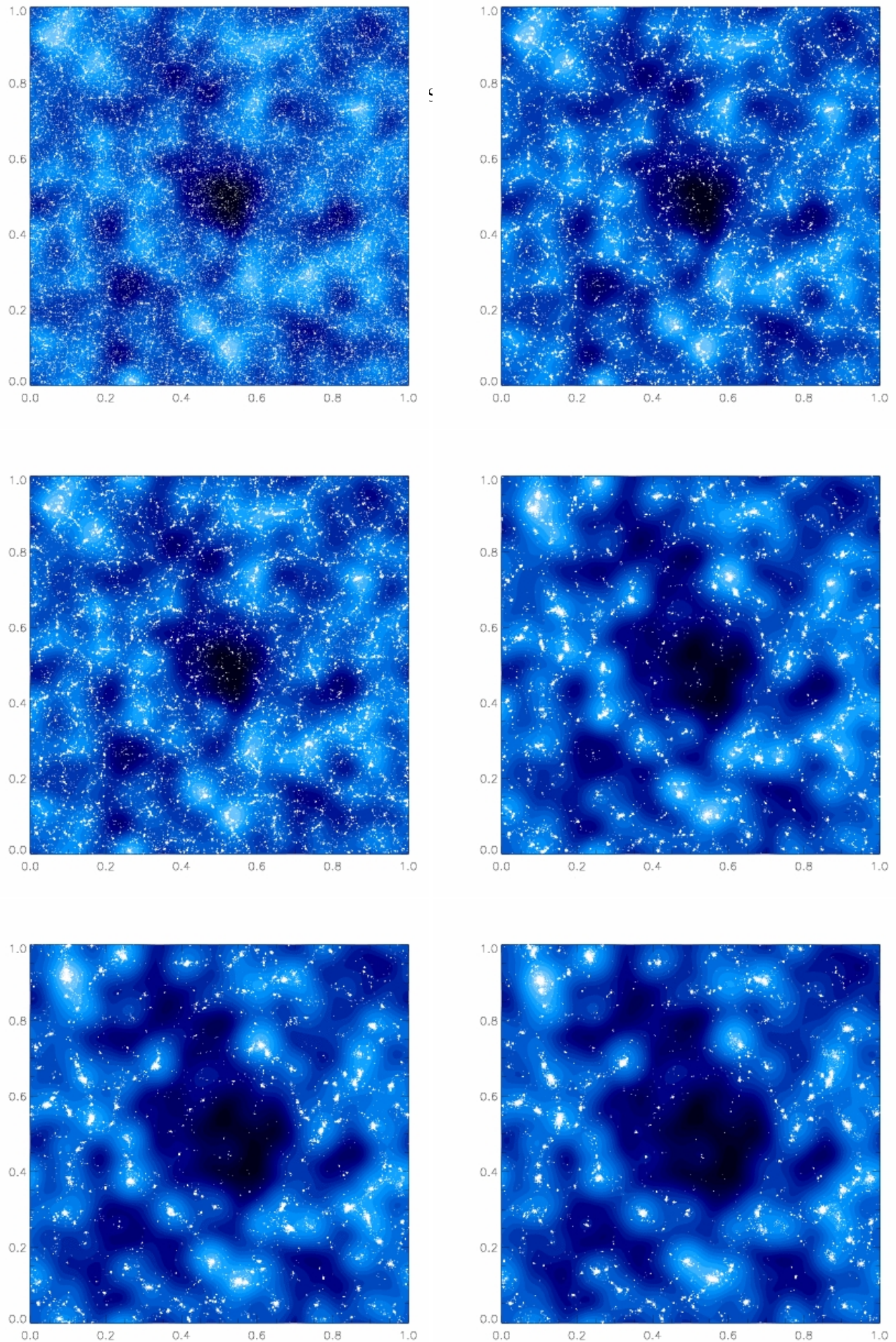


Figure 4.3: The figures show the particles and the smoothed density field at six different time steps. It shows the simulation are from the $n=0.0$ power-law model. These are resp. 0.05, 0.15, 0.35, 0.55, 0.75 and 1.0. The slice is of $10 h^{-1}\text{Mpc}$ thick and shows the density field which is smoothed at a scale of $4.0 h^{-1}\text{Mpc}$.

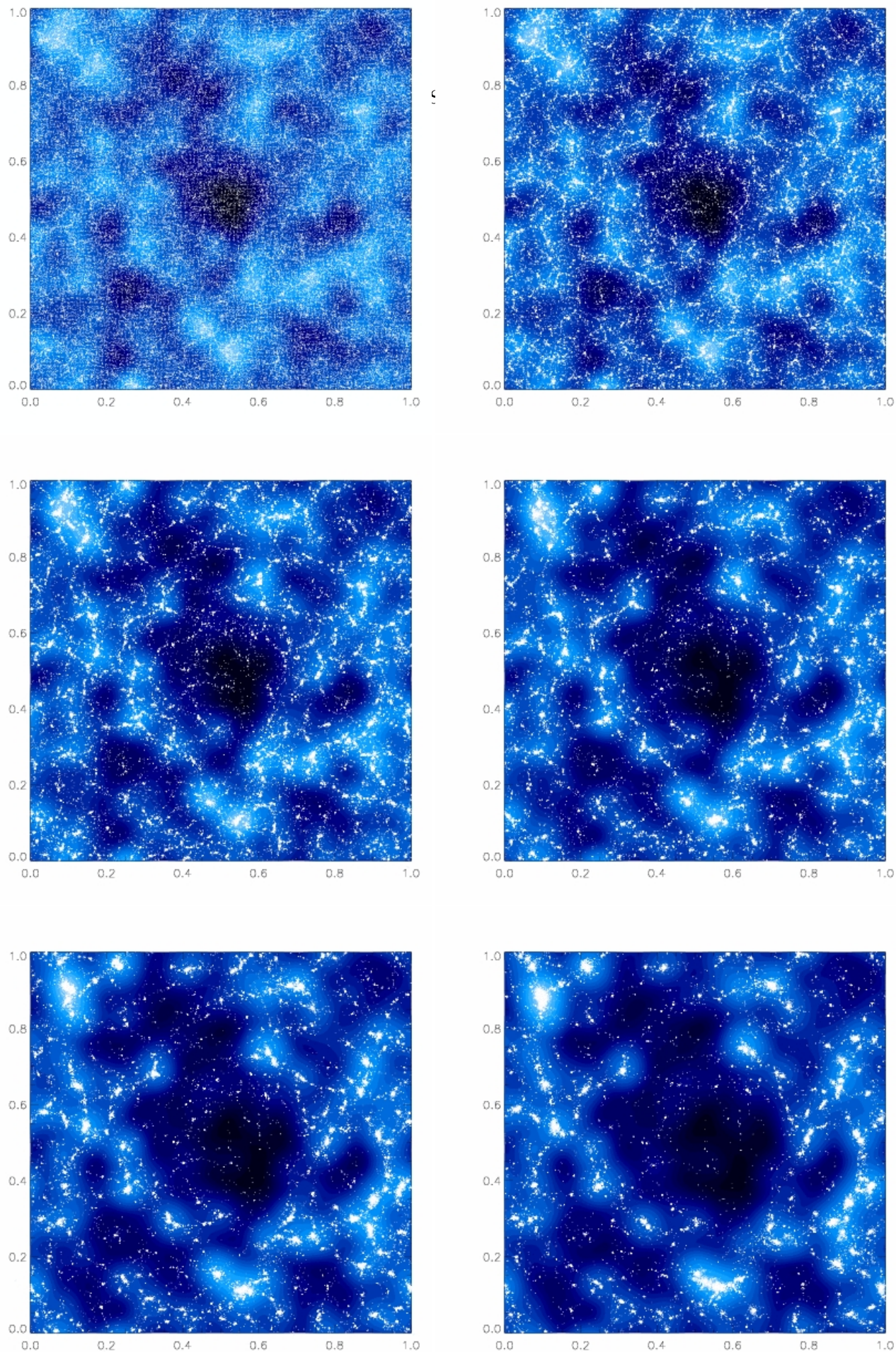


Figure 4.4: As in figure 4.3

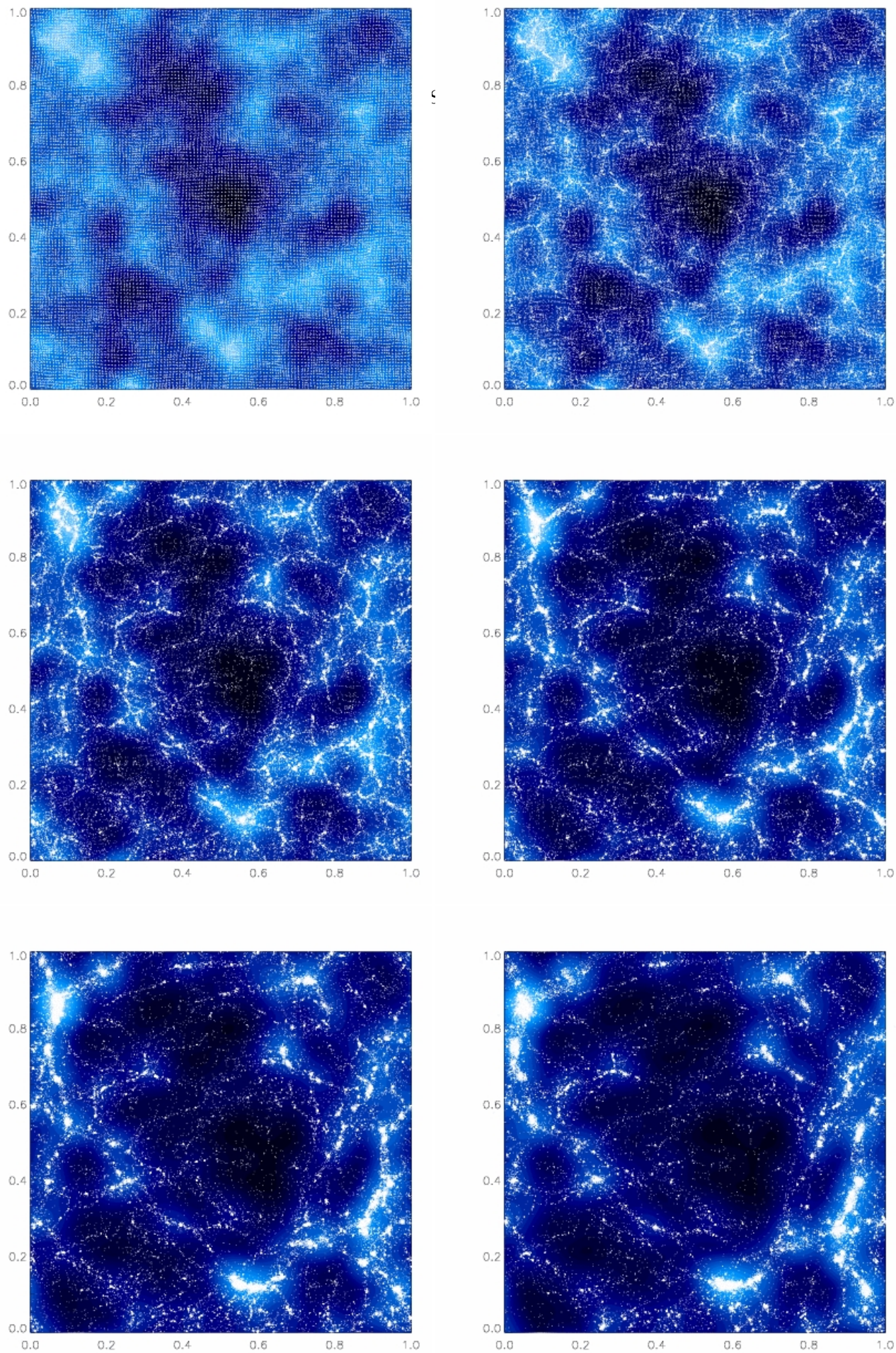


Figure 4.5: As in figure 4.3

4.3 Void Collapse

Since it was visible that the voids located near the central parts at earlier times show an expected merging pattern. Here we will focus in on the edge of the void as it seems that this has a major impact on its surrounding. Therefore we will make various zooms on the edge of the large scale voids.

For instance figure 4.6 shows a zoom of the lower edge of the $n=-0.5$ constrained void. The large scale behavior of this regions seem to be comparable to that described by the void merging pattern in left image of figure 4.2. In the upper regions the constrained void expands and meets another void that expands from the lower regions upward. These form a wall like structure in the middle section of the images. this is thus readily comparable to the generic void merging mode.

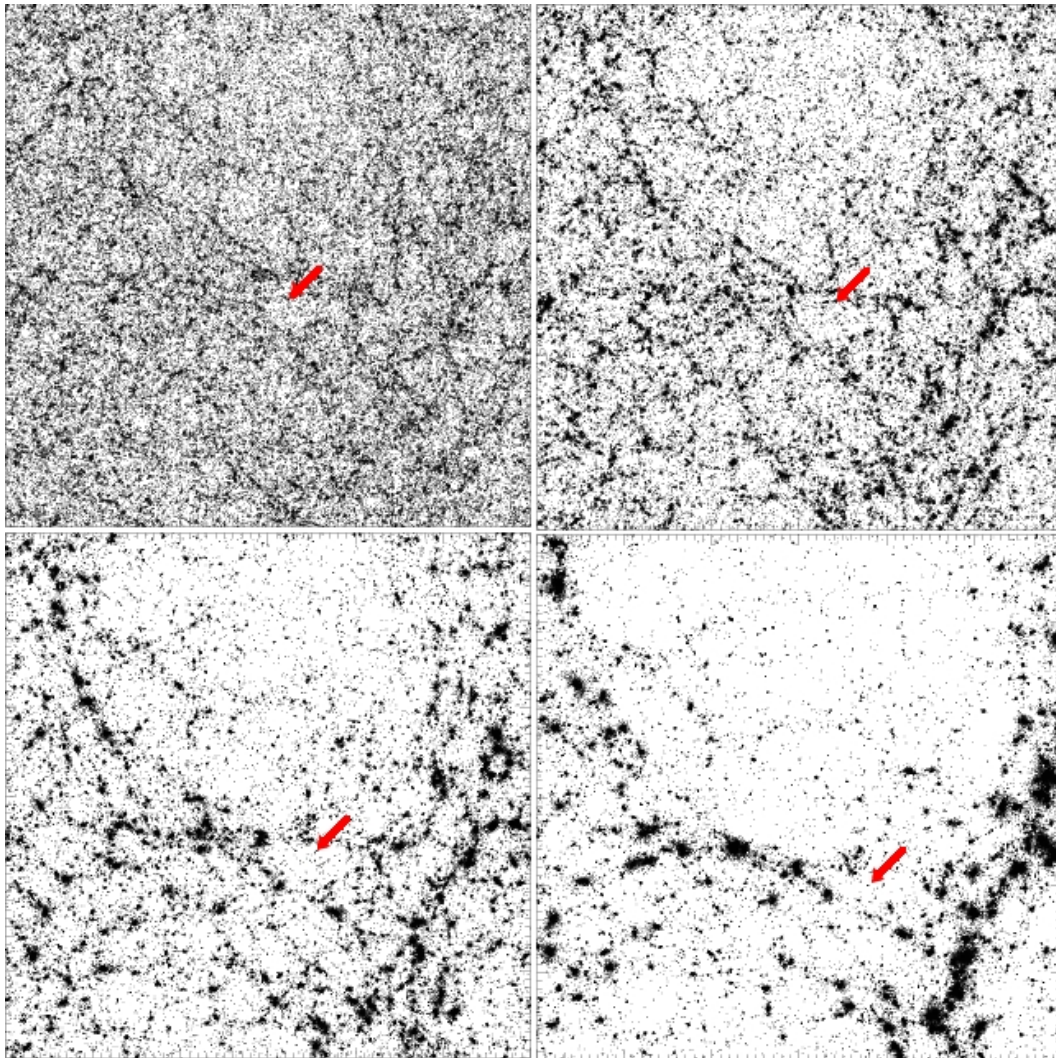


Figure 4.6: The figure shows a zoom on the lower boundary of the constrained void at four different expansion factors, resp. 0.1, 0.25, 0.5 and 1.0. The slice is of $1/5$ thickness and it the width is $60 h^{-1} \text{Mpc}$, centered on the lower edge of the constrained void.

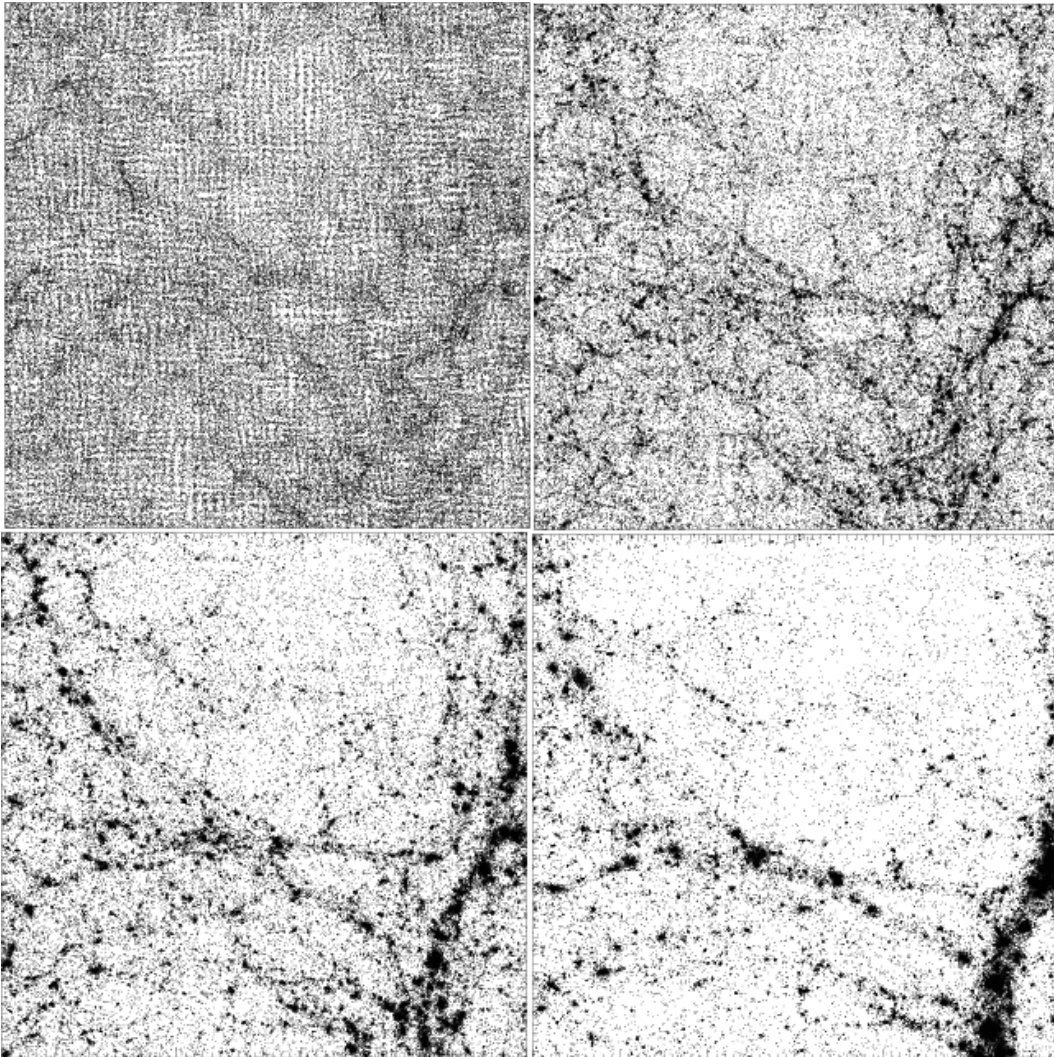


Figure 4.7: As figure 4.6 now for the $n=-1.5$ case

Much of the small scale structures initially located near this region, eventually end up in the wall. This includes the smaller voids as well as the small scale clumps. An example is indicated with the red arrow. As it is forming inside the wall like structure. The void is at the same time being influenced by the collapse of this wall. This can clearly be seen in the fact that it gets sheared and torn along the direction of the wall or void boundary. The same behavior can be seen in figure 4.7, which shows the same region but then for the $n=-1.5$ case. Indeed the same small scale void is stretched out in an anisotropic fashion.

In figure 4.8 the central left side of the $n=0.5$ void is plotted, the collapsing void population is less visible here. In order to see whether these are present, the field was smoothed with a Gaussian filter of $1.0 h^{-1}\text{Mpc}$. Then the simulation box was searched by hand to find a minimum. This was done in the following manner, first a small square region was selected in the slice particles. This region was centered on the void at the moment that the small void was most clearly visible. This was our initial guess of the void position.

Subsequently the 3 dimensional density field was searched. This was done by plotting the

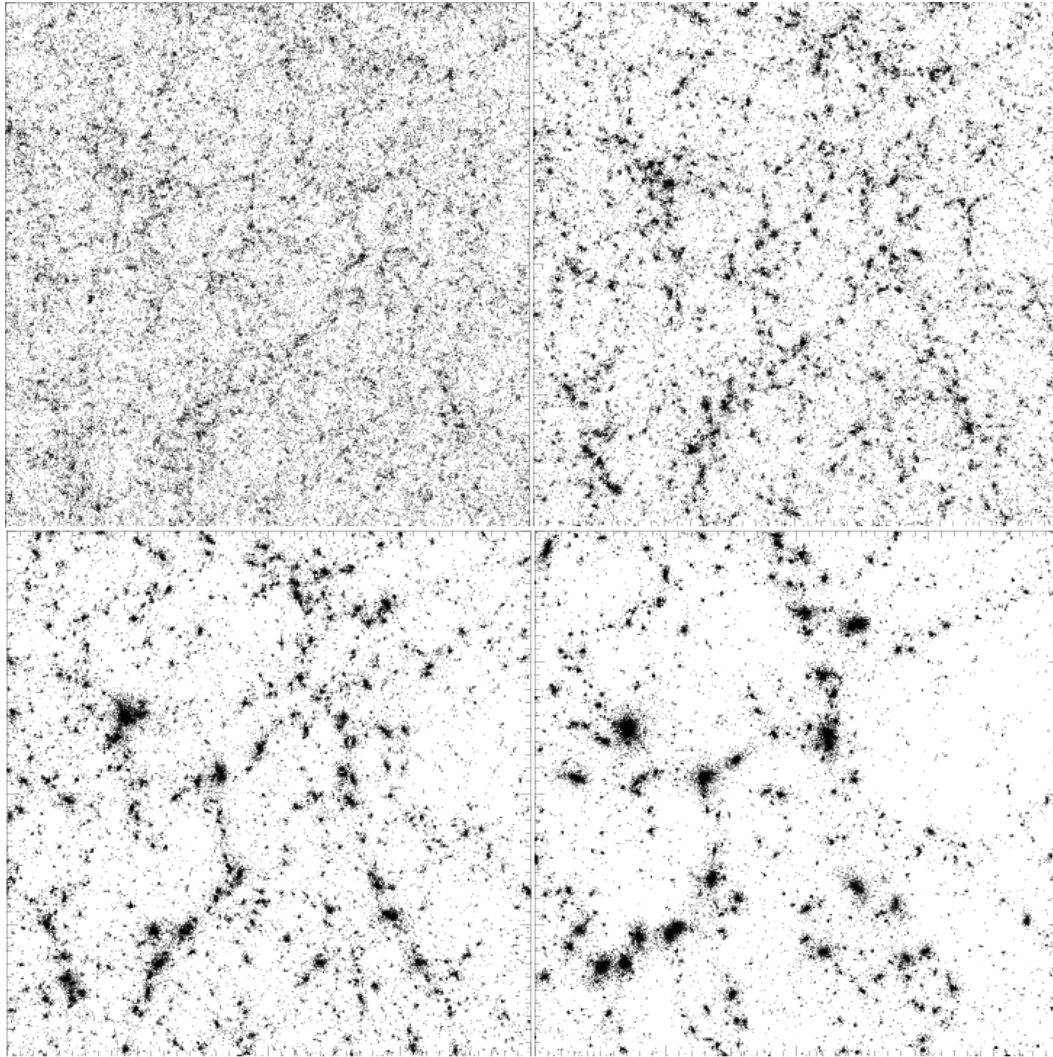


Figure 4.8: The figure shows a zoom on the left side of the large void edge. At the same expansion factor as in figure 4.6.

xy, yz and xz planes out of the selected density cube, with the same size of the selected square. Then for each slice the minimum region of the void was indicated by hand, if this was not in the center of the slice then the cube was shifted to get it centered. Then the next plane was searched for a minimum and shifted again if necessary, this process was continued until all three planes had a clear defined minimum all centered inside the slice. These particles were selected and the center of mass of these particles was computed for each expansion factor. In this way the Lagrangian flow of the void could be traced, and then for each time step the density and particle slices centered on this track were plotted. The result of such a procedure is shown in figure 4.9. This small void was identified in approximately the region as shown in figure 4.8. The figure shows xy, zy and xz planes at six different output steps, $a=0.05, 0.15, 0.3, 0.55, 0.8$ and at 1.0. The smoothed density field and particles are shown. At the earliest output files the void is clearly identifiable in the density field, as a minimum in the field and particles. Note that the colors are rescaled every time to show the change in morphology. As can be seen in

the second output file the smoothed field has not changed that much, indicating that at $1.0 h^{-1}\text{Mpc}$ the field is still linear. This is in contrast to the particles, which show a definite growth of small scale clumps. Then approximately at the third output file the topology begins to change slightly. This is most clearly seen in the xy and xz planes, as there is a clear contraction in the x direction. This process continues in the following slices, and the last slices show that the void in the xy and xz plane has ended up the filamentary structure the runs from topside to the bottom side.

The evolution of the yz plane is somewhat different. The density field shows a kind of closing of the minimum. This same can be seen in the particle distribution, which also indicates to an isotropic contraction toward the center of the void. Still, in the last slice of the yz slice a clear minimum in the particle and density field remains visible. This evolution can be understood, when the large scale evolution of the constrained void is also taken into account. As the void was identified on the central left rim of the large void. This would explain the contraction in the x direction, while at the same time leaving the yz plane unharmed. Because the zy -plane is roughly perpendicular on the direction of the void expansion. Thus we conclude that the void collapsed in a rather anisotropic fashion in the x direction. In particular it collapsed into a wall like structure, which formed due to the expansion of the large void.

Thus in summary the evolution of the large void has a definite impact on the small void population in its surrounding. This was shown by the zooms on the edge of the void, and by tracing the evolution of one of such a collapsing edge-void. At least a part of the collapsing void population were identified in this analysis. Eventually the statistics and evolution of the whole void population has to be followed. Then we can not resort to by the hand selected voids. And another objective manner to identify the void population has to be used. In the next chapter we will focus on developing our own void finder, which is tested on voronoi models and LSS simulations.

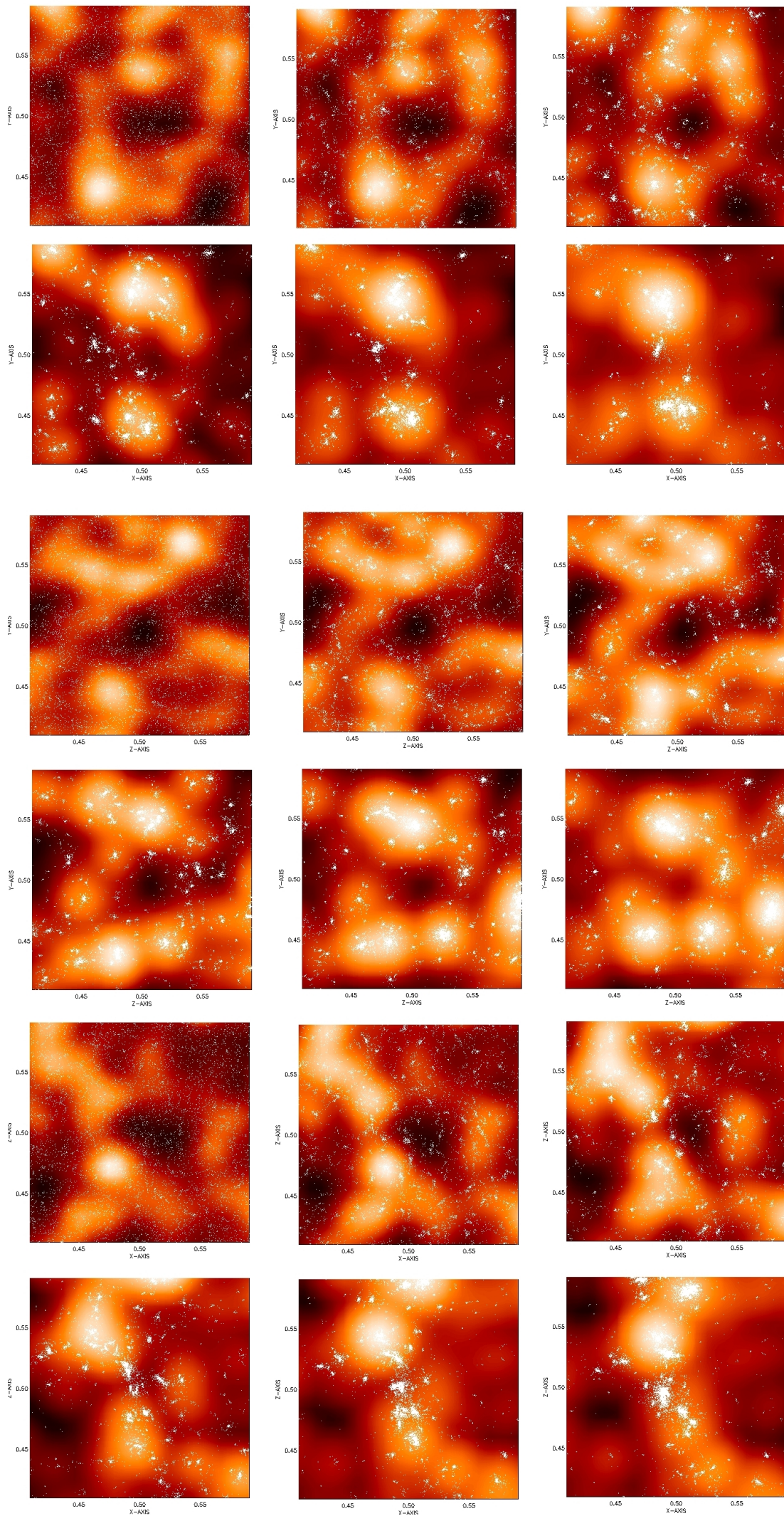


Figure 4.9: See text

Chapter 5

Segmentation by overflow

A problem with the previous analysis is that the voids were selected by just zooming in on an interesting region of a selected slice out of the simulation box. What we need is a objective manner to select our regions, so that the void population can be analyzed. Since the object of interest are voids, the best way to select our regions is with a void-finder. There exist a number of void-finding algorithms. Currently the most commonly used versions are based on the ‘VOIDFINDER’ algorithm developed by El-Ad & Piran (1997). A modification of this scheme has been introduced and extensively applied by Hoyle & Vogeley (2002). Various alternatives have been developed over the years, a recent example is the algorithm used by Colberg et al (2005). This method did seek to take into account the possible variation in shape of voids by basing itself upon the fitting of underdense ellipses.

Here we introduce a new void finding algorithm, the *watershed transform*, which has been especially devised to be able to detect the substructures in the distribution of galaxies and therefore assess the void hierarchy we seek to study in this work. The watershed algorithm offers several advantages with respect to other void finders. Basing ourselves upon the description of advantages of the transform by e.g. Beucher & Meyer (1990), we may mention the properties of

- the watershed naturally placing the *divide lines* on the crests of a field, and although a void boundary might be distorted the watershed transform will detect the boundary of a void.
- the transform naturally produces closed contours. Therefore, as long as the minima are well chosen, the transform will not be sensitive to local protrusions between two adjacent voids.
- The watershed works directly on the topology of the field. Thus it does not rely on a geometrical predefined shape. So the voids found can have every shape.
- In the case of an ideal smooth density field, it will find the possible voids in parameter free way. And no predefined values have to be introduced.

Before presenting the fundamentals and implementation of our watershed algorithm we will first describe in some detail the characteristics of other void finders. With the watershed algorithm stemming from the field of *mathematical morphology* and its application to *computer visualisation* problems we will subsequently introduce the fundamental concepts underlying the watershed algorithm. In particular we will include a short introduction into *Mathematical Morphology* (MM). After having described the definition and theory of the watershed transform, we will discuss shortly how we translate this into the analysis of cosmological density fields. Because the watershed algorithm is based upon the analysis of a continuous “*intensity*” field while we seek to analyze the discrete point distributions yielded by cosmological N-body simulations or

those of the galaxy redshift surveys we will shortly describe the techniques we use to translate these discrete datasets into properly representative continuous cosmological density fields. This has proven to be a far from trivial issue. Conventional algorithms, such as the described TSC method, tend to dilute the geometrical or topological intricacies as well as the presence of internal hierarchical (sub)structures. Finally, in the work described in this report we have restricted ourselves to a meticulous two-dimensional analysis. Given the considerable body of work on the watershed technique has been devoted to two dimensions, we will shortly discuss our efforts towards extending the description to a full three-dimensional method.

5.1 Void Detection

Concerning the first method, it can be summarized as follows; given a particle distribution, which could be either galaxies in a redshift survey or particles from a N-body simulation. Then these particles are subdivided into wall and void-galaxies/particles. The particles are tagged as wall galaxies according to a scheme based on the distance and number of neighbors. Here the main quantities that discern the two types are n , the number of galaxies within a distance l . If a particle has a more than n particles within range l than it is tagged as a wall galaxy. Field galaxies are those that do not oblige this rule.

Subsequently, voids are found by matching “empty” (empty meaning no wall galaxies) regions with ever decreasing empty spheres. Every time an empty sphere is found it can either be a new void or belong to another larger void. In the former case this means that the sphere is the largest and first empty sphere that fits into an empty volume. In the latter case this new sphere is a refinement on a larger and previous found void region. This new sphere falls either totally within the previously identified void or on its edge. If it is on the edge then this new region is added to this empty region.

As the radius decreases the initial sphere grows by iteratively adding smaller spheres to its outer surface. This process must be truncated at some small scale the obtained, and the found regions are the voids. It is important to note that in this particular iterative scheme the seed for a particular void is the largest empty spherical region that can be fitted into it.

A variant on this scheme was proposed by Hoyle and Vogeley (2002), instead of iterating from a large radius to smaller radii, they immediately fit to every empty cube cell a maximal sphere. These maximal spheres are merged to form the voids. The merging criteria here is; if two spheres have more than a certain amount of overlap then spheres are merged.

The other void finder method that was recently proposed can be explained as following; the first step in this method is to interpolate the particles to a grid (particularly Nearest Grid Point), so to make a density cube. Subsequently the field is smoothed using some adaptive smoothing technique. The next step is to find the minima in this density field, and onto each minima an ellipse is fitted. The ellipse is required to have a maximum density within the fitted volume. This scheme used a value of at least $\delta = -0.8$ for the internal density.

Then adjacent ellipses are merged according to the distance between their centers. The line section connecting two centers can be subdivided into three parts a central part where both ellipses overlap and two sections on end of this line only covered by one region. Then two ellipses are merged only if the middle section is longer than either two of the end-sections. This method closely resembles the method of Hoyle and Vogeley (2002). The seeds for this scheme are the largest underdense ellipses that can be fitted onto a minimum.

Both methods have their own benefits, i.e.: each have a clear interpretation of what the results will be, secondly the first can be easily implemented on a redshift survey. While the second is tailor-made for density field from N-body simulations. However we think that both methods avoid a more subtle issue. As Dubinski et al. (1996), Weygaert & van Kampen (1993) showed and as also visible in figure ??, large voids are never empty. This is due to the merging history of a void, therefore any void is expected to have subvoids. One has to deal with this

fact and subvoids have to be merged. Both methods use a merging scheme to overcome this, however it is based on distance not on the density.

Another problem is that small voids and outskirts of larger voids are never perfectly spherical. As both methods are based on a spherical or elliptical regions. Therefore they are not able to follow the small scales. And they are not able to find the boundary. We expect that for void merging ensemble the strength of this boundary between two empty regions is a vital criterion to define the edge of a void.

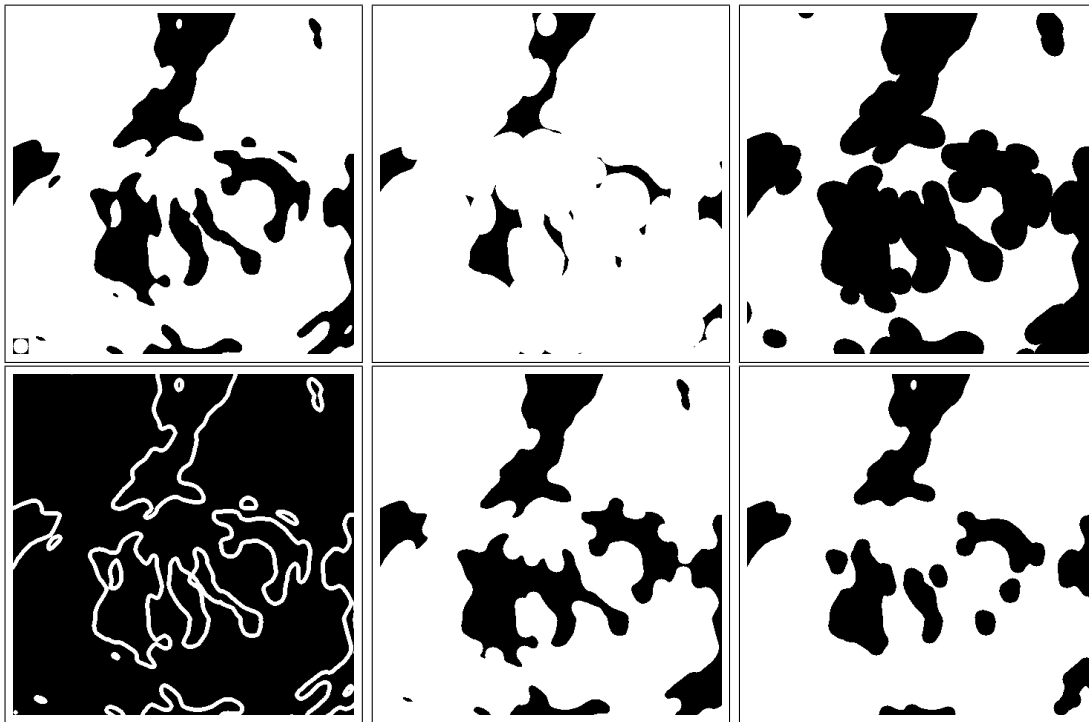


Figure 5.1: The image shows the effect that morphological operators have on an image. The test image is shown in the upper right corner, also the structuring element is shown in the lower left corner of this image. Then from left to right the eroded and dilated images are shown, and in the lower row the gradient, opening and closing are presented.

5.2 Introduction to Mathematical Morphology

Mathematical morphology(MM) is a field of image analysis which aims to characterize an image by its geometrical structure. It deals with concepts from algebra (set theory, lattice theory) as well as geometry (translation, distance, convexity). It has been used in various branches of other sciences such as material science, medical imaging, pattern recognition, etc. The basic operators are erosion and dilation, for binary images these are Minkowski addition (\oplus) and subtraction (\ominus) with a certain set A over the entire image. These two operations can be understood as probing an image with a certain shape or ‘structuring element’ A , by resp. answering the question whether it is contained or has overlap with a certain set in an image;

$$\begin{aligned}
 X \oplus Y &= \{x + y \mid x \in X, y \in Y\} \\
 X \ominus Y &= \{h \mid y + h \in X \text{ for all } y \in Y\} \\
 \text{dilation with } A : \delta_A &= X \oplus A \\
 \text{erosion with } A : \epsilon_A &= X \ominus A
 \end{aligned}$$

Figure(5.1) gives an example of an erosion and dilation of a binary image. These two operations have a number of properties, they are invariant under translation and invariant under a global scaling, they are increasing (meaning if $X \subseteq Y$ then $\delta(X) \subseteq \delta(Y)$), and they can be considered each others dual in two ways. Firstly in the sense of the complemented set, meaning erosion of a set is the same as dilating the complement and vice versa. Secondly, in the sense of the adjunction relationship;

$$Y \oplus A \subseteq X \iff Y \subseteq X \ominus A.$$

Note that applying these operations in general discard information. Because only if the sets X, Y and A are convex and similar the application of an erosion, followed by a dilation gives back the same image. In fact the consecutive application of an erosion and a dilation yields two new operators; an opening and a closing. An opening is erosion followed by a dilation and a closing is defined as a dilation followed by erosion;

$$\begin{aligned} \text{opening } \lambda_B &= \delta_B \epsilon_B = [(X \ominus B) \oplus B] \\ \text{closing } \phi_B &= \epsilon_B \delta_B = [(X \oplus B) \ominus B]. \end{aligned}$$

These operators are increasing, idempotent (applying the operator twice yields the same output) and they are respectively anti-extensive ($\lambda(X) \subseteq X$) and extensive ($X \subseteq \phi(X)$) (In fact these are THE conditions that define a morphological operator!). Figure(5.1) shows the effect of an opening and a closing on a binary image. We see that an opening amends caps, removes small islands and opens isthmuses, while closing closes channels, fills small lakes and partly the gulfs. Another combination of an erosion and dilation is when the first is subtracted from the latter. This gives a morphological gradient as is also presented in figure 5.1.

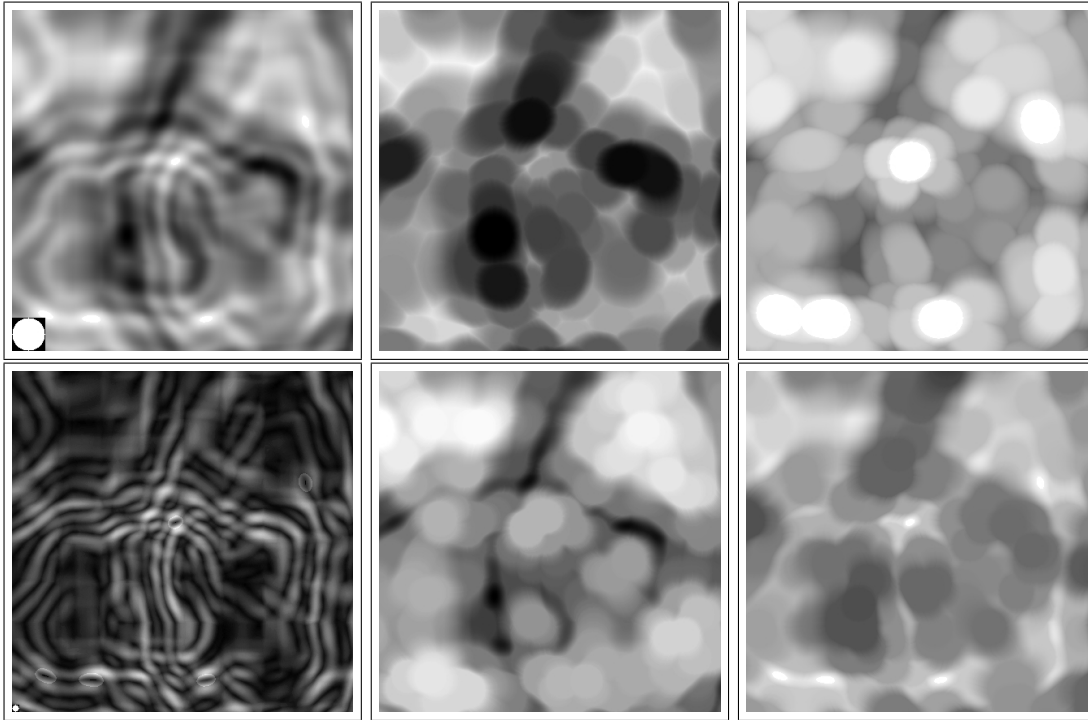


Figure 5.2: The same as figure 5.2 only now for a grayscale image.

5.2.1 Grayscale Images

The operators as described above can be generalized to grayscale images using lattice theory. A complete lattice is a set \mathcal{L} , for example grayscale images, which has a partial ordering ' \leq ' such that every subset of \mathcal{L} has a supremum and infimum. For example, all the grayscale images ordered by their pixel value can be considered a complete lattice, or all the subsets E of the power set, $\mathcal{P}(E)$, ordered by inclusion are a complete lattice. In the complete lattice framework MM studies the operators from \mathcal{L} into \mathcal{L} . Of particular interest here is the application to grayscale images, which will be used in the next section. A grayscale image is a function $f : \mathbf{Z}^n \rightarrow \mathbf{Z}$,

where $f(x)$ is the gray-value at vertex x . A grayscale image can be considered as a stack of decreasing sets, such a set or section, may be simple retrieved as follows;

$$S_i(f) = \{x \in \mathbf{Z}^2 : f(x) \leq i\}$$

If the image is considered a landscape then the section can be seen as the support of the surface which lies above a gray-level i . The image f can then be reconstructed by stacking all these sets on top of each other. In this framework the erosion/dilation of a grayscale image is the erosion or dilation applied to all the sections. Given a set B (flat element) then;

$$\begin{aligned} f \oplus B &= \sup\{f(x-y), y \in B\} \\ f \ominus B &= \inf\{f(x-y), -y \in B\}. \end{aligned}$$

As can be seen from figure(5.2) erosion shrinks positive peaks (white), while peaks that are smaller than the structuring element disappear completely, furthermore valleys are expanded (black). The duality of the operators can be readily noticed from the dilation image, as it does the same as erosion, but instead on the black levels. Again from the erosion and dilation other operators can be constructed, such as opening and closing (figure 5.2), but also the morphological gradient. This has the same description as above; it is the dilation minus (i.e.: '-' for functions and '/' for sets) the erosion. All these grayscale operations are shown in figure 5.2. This gradient operator is often used in object detection, because an object is often associated with a change in grayscale w.r.t the background. Various other operations/filters can be defined with openings and closings, among them are for example granulmetries (e.g. a sequence of erosions with increasing scale), and distance transforms.

5.2.2 Distances

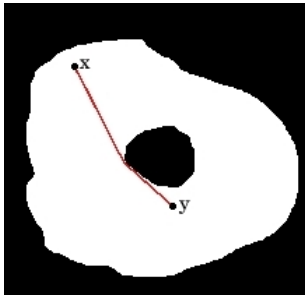


Figure 5.3: This geodesic path has the infimum length of all the paths connecting x and y which are included in the white set.

The notion of distance is a very useful concept for understanding and defining mathematical operators. Here we will first consider the geodesic distance on a set. In the next section we will introduce another distance; the topological one. Let $X \subset \mathbf{Z}^2$ be a set and x and y two points in X , then the geodesic distance $d_X(x, y)$ is the length of the shortest path included in X and connecting x and y , see figure(5.2.2). In the same manner the distance between two subsets A, B in X can be defined as the minimum length of all the paths between the elements of A and B . An application of this distance gives for example the distance function; for every point y in Y compute the distance to the complement of Y and ascribe this to point y . This produces a stack of sections, and each section at level i is given by the erosion of Y with the disk of radius i . An example of a distance function is given in

figure(5.2.2), where the distance is indicated by the red coloring.

This distance can now be used to segment the image, using the definition of *zone of influence*. Suppose there are n connected subsets, $Y_i i \in [1, n]$, in the set X . The geodesic zone of influence $z(Y_i)$ of a subset Y_i is, the set of all the points that are strictly closer to Y_i than to any other subset Y_j with $j \neq i$, i.e;

$$iz_X(Y_i) = \{y \in X, \forall j \neq i, d_X(a, Y_i) \leq d_X(a, Y_j)\} \quad (5.1)$$

The boundary between two sets is then given by the set that is in X and not in the union of all the zones of influences, $IZ_X = \bigcup_n iz_X$. This is called the SKIZ; the skeleton by geodesic zones

of influence.

$$\text{SKIZ}_X = X \setminus \text{IZ}_X \quad (5.2)$$

The relation between the SKIZ and the distance function is shown in fig.(5.2.2), the SKIZ is indicated with the white divide lines, and note that these lines exactly follow the ridges of the distance surface. The extension of the SKIZ to grayscale images, the *watershed transform*, will be presented in the next section. But first an intuitive approach to the watersheds transform is presented, before using the distance.

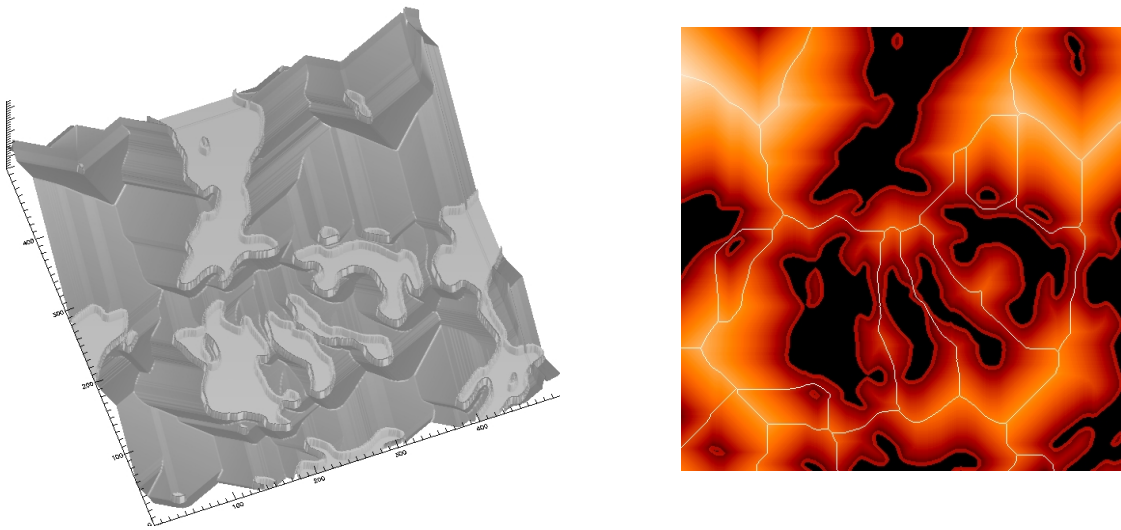


Figure 5.4: These two images show respectively the distance transform and the resulting segmentation. The binary image is the same as in figure 5.1.

5.3 Watersheds in image segmentation

Image segmentation deals with the detection of objects by subdividing an image into regions or objects. One can roughly take two approaches in image segmentation the first is based on detecting discontinuities. The other searches for similar regions by some sort of criteria, as for example one does when one applies a threshold to an image or region growing algorithms. The watershed transformation (WST), is defined in the context of mathematical morphology. It is one of the primary tools for image segmentation, because it incorporates several aspects from other segmentation approaches. These are mainly region growing (a conditional searching method starting at some seed) and graph based edge detection. The method was originally proposed by Digabel and Lantuejoul(1978) and further developed by Beucher and Lantuejoul (1979). For the interested reader the book by Gonzalez and Woods provides a nice introduction to image segmentation and particularly to the WST, while Beucher & Meyer(1990) and Beucher(1993) give a good summary of the transform, its applications, and discuss the extensions to the formalism. Some examples where the WST has been applied are; detecting tumors in medical images, detection of cells in microscopic images, automatic detection of anomalies and flaws of products in assembly lines, and many more.

The basic idea behind the WST comes not unsurprisingly from geography, where watersheds are the divide lines of separated domains that attract rain, say a lake or river. To understand the principle idea behind the transformation it might be easier to imagine the landscape being pierced at the places where water collects, i.e. the local minima. Subsequently this landscape

is slowly being emerged into water and then the water begins to flood from the minima, this water will fill up the basins. At the points where two floods meet a dam is build, so to avoid two floods from two different minima to merge. This process continues until the whole landscape has been flooded. Then only the all dams remain, which still stick out above the waterlevel. At this final point each region enclosed by a dam contains exactly one of the pierced minima. These are called catchment basins as they receive water from only one minima, the dams are called the watershed lines. This process is illustrated with the set of images in figure(5.4).

5.4 The watershed transform, continuous case

The watershed transformation simulates this immersion process, by regarding the image as a topographical surface that is pierced at the minima. The outcome of the transformation is a new image where the area of one catchment basin is labeled according to a number associated with a minimum. All the watershed lines are given also one unique label. For the continuous case (see Roerdink & Meijster and Meyer(1994)) a formal definition of the transform can be given with a distance measure defined over the image. Assuming that an image f , is real twice continuously differentiable function on a connected domain D . The topographical distance between two points p and q in D is defined as

$$T_f(p, q) = \inf_{\lambda} \int_{\lambda} \|\nabla f(\lambda(s))\| ds. \quad (5.3)$$

Basically meaning the shortest path of all paths between to points is the one that has follows the steepest slope. Then using this distance measure the definition of a catchment basin and the watershed boundary is:

Definition 1 (Watershed Transform) *Let $f \in C(D)$ have minima $\{m_k\}_{k \in I}$, for some index I . The catchment basin $CB(m_i)$ of a minimum m_i is defined as the set of points $x \in D$ which are topographically closer to m_i than any other regional minimum m_j :*

$$CB(m_i) = \{x \in D | \forall j \in I \setminus \{i\} : f(m_i) + T_f(x, m_i) < f(m_j) + T_f(x, m_j)\} \quad (5.4)$$

The watershed of f is the set of points which do not belong to any catchment basin:

$$Wshed(f) = D \cap \left(\bigcup_{i \in I} CB(m_i) \right)^c \quad (5.5)$$

Let W be some label, $W \notin I$. The watershed transform of f is a mapping $\lambda : D \rightarrow I \cup \{W\}$, such that $\lambda(p) = i$ if $p \in CB(m_i)$, and $\lambda(p) = W$ if $p \in Wshed(f)$.

This definition explains exactly what the output of the transformation will be; on the crest/the watersheds of the image the transform assigns the label W , and each catchment basin points are labeled with it's unique label $i \in I$ associated with minimum m_i .

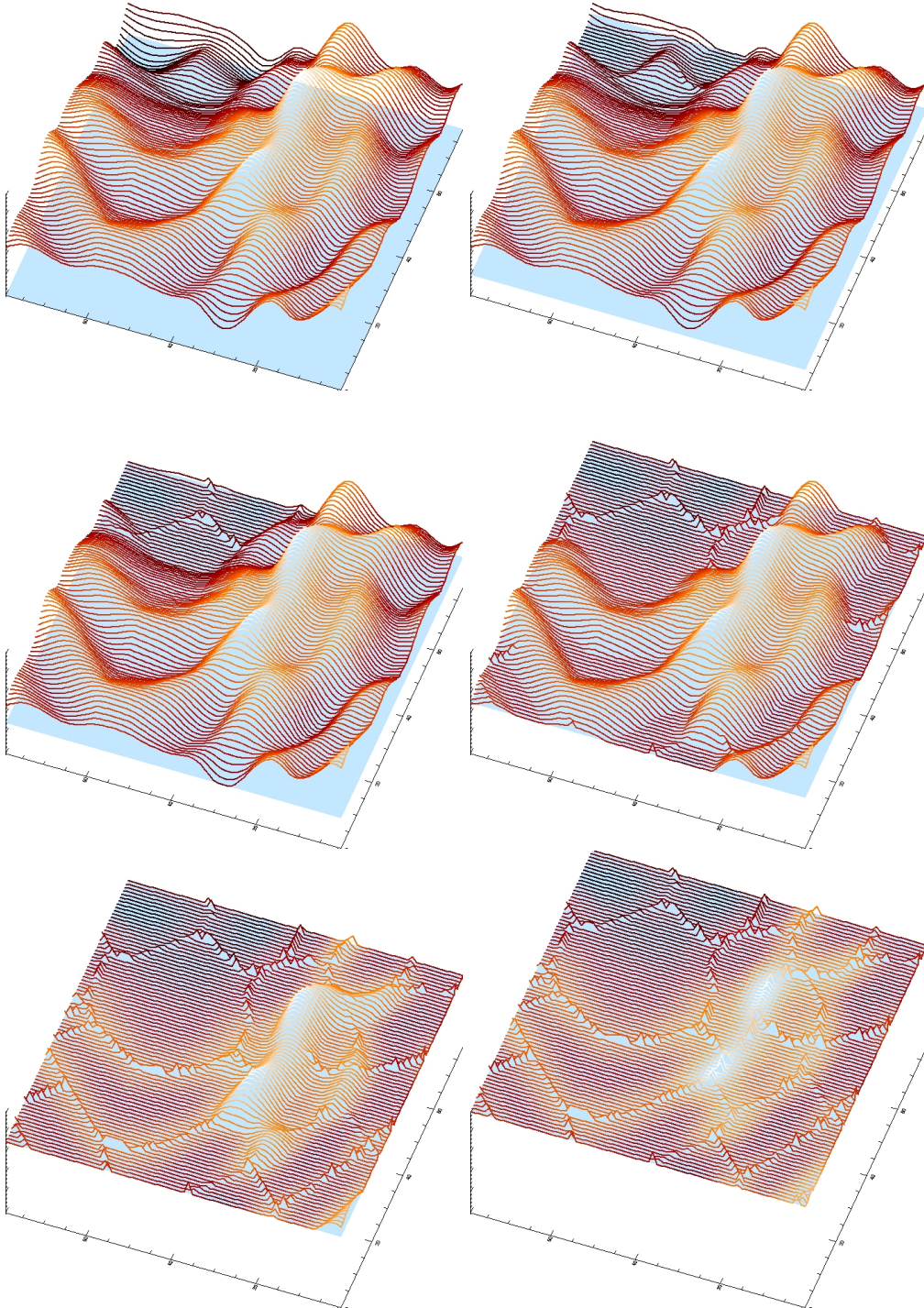


Figure 5.5: These figures show the principle of the watershed transform. The first picture is the surface that will be segmented. From each local minimum a flood will start and as two floods meet a dam is constructed. This process starts at the deepest minima and as the water level rises the dams slowly walk upward over the crests of the mountains. In the final image one is left with water and dams, that indicate the final segmentation.

5.5 The watershed transform, discrete case and algorithms

In the discrete case however the situation becomes a little more complicated and the results can depend on which particular algorithm is used. Various kinds of algorithms exist in the literature. They can be divided into two groups; those that simulate the immersion process and the second aims at the detection of the watershed lines via the distance.

The definition of the algorithmic watershed by immersion was given by Vincent & Soille(1991). Here a recursion is defined over the gray levels from the lowest h_{min} to the highest level h_{max} . Starting at the lowest level, to each minimum its zone of influence is appended. First note the complemented set of a section $S_i(f)$ of an image f , Z_i , is defined as;

$$Z_i(f) = \{x \in \mathbf{Z}^2 | f(x) \leq i\}, \quad (5.6)$$

and we define a minimum as a plateau of altitude, h , from which it is impossible to reach a point of lower altitude. At each particular threshold, i , two things may happen; either a new minimum may be encountered at level i or a new set of points are found, which can be connected to one or more minima. If it is connected to two or more minima, the region that belongs to a particular minima in this set is determined with that iz of these points.

Definition 2 (Watershed by immersion) *If $W_i(f)$ is the union of the catchment basins at level i and let m_{i+1} be the minima at level $i + 1$ then;*

$$W_{i+1} = [\text{IZ}_{Z_{i+1}}(Z_i)] \cup m_{i+1} \quad (5.7)$$

If D denotes the domain of f ;

$$Wshed(f) = D \setminus W_{h_{max}} \quad (5.8)$$

Another definition, which is also commonly used as the basis for watershed algorithms, is the definition of the watershed by topographical distance. The goal of these algorithms is not to simulate the immersion process, but to find the vertexes that are connected to a minimum via the shortest path with respect to all other minima. These algorithms are related to the graph theoretical problem of the shortest-path forest and the algorithms resemble Dijkstra's algorithm of shortest path problems.

Here the goal is to find for each node, the shortest path that connects to its nearest root node. In this framework an image can be seen as a connected digraph (meaning every node is reachable from every other node, and each arc is an ordered pair of nodes). The pixels are the nodes and the arcs are defined by the pixel-connectivity (usually 4- or 8-connectivity). The shortest path is found by traversing the graph and keeping track of the walking cost, which needs to be minimized. As noted above for a grayscale image, seen as a surface, the shortest path/geodesic is related to the topographical distance. The geodesics of a surface are in fact the paths of steepest descent, i.e. the path which a droplet of water would take if it flows down the surface. The cost it takes to traverse a path in the graph must be a non-negative increasing function. First define the maximal slope linking two pixels, p and p' as

$$LS(p) = \max\left(\frac{f(p) - f(p')}{dist(p, p')}\right), \quad (5.9)$$

then the cost of walking to a neighboring pixel is defined as;

$$\begin{aligned} cost(p, p') &= LS(p) * dist(p, p') & f(p) > f(p') \\ cost(p, p') &= LS(p') * dist(p, p') & f(p) < f(p') \\ cost(p, p') &= \frac{LS(p) + LS(p')}{2} * dist(p, p') & f(p) = f(p') \end{aligned}$$

Comparing this to the continuous case, yields the following definition of the watershed by topographical distance;

Definition 3 (Watershed by topographical distance) Let the topographical distance along a path $\pi(p_1, p_2, \dots, p_n)$ be the sum of the cost

$$T^\pi(p_1, p_n) = \sum_{i \leq n} \text{cost}(p_i, p_{i-1}) \quad (5.10)$$

, then the topographical distance is the infimum distance over all the paths connecting p and q . The definition of the catchment basin and the watershed lines are the same as in Definition (1) using this distance measure.

Several problems can occur with the implementation and usage of the watershed algorithm, two of these problems will be treated below. The first is the plateau problem. Another problem is the oversegmented outcome of the transform. As often too many insignificant watershed lines are produced.

5.5.1 Plateau problem

In the above definition we quietly assumed that the image is lower complete, however images are in general not lower complete. None lower completeness means that there are plateaus, i.e. where many connected pixels have the same value. At the occurrence of plateaus the above definition of topographical distance can not properly deal with these regions, as there is no ordering relation between the pixels. However, the general idea is that, two floods should divide a plateau on the medial line. The medial line can be seen as the set of points which lies closer, in the geodesic sense, to minima i then to minima j . This is just like the SKIZ on a binary images, but then applied to the plateau.

So when applying the WST one should be aware of this problem and one can either solve this by making the image lower complete using the distance function. Alternatively, the geodesic distance can be incorporated within the algorithm itself.

5.5.2 Oversegmentation

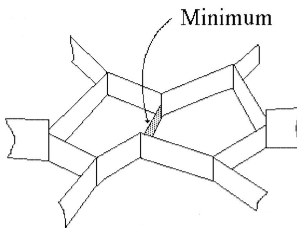


Figure 5.6: The concept of hierarchical watershed is shown. Not all divide lines produced by the watershed may be relevant. These can be taken out if they are lower than some criteria, and the significant sheds remain.

When an image is noisy and has much pixel by pixel variation, many local minima can arise that are not relevant. Meaning that they do not correspond to any object or vice versa too many minima correspond to one object. If the watershed is applied on such an image, the result will be a segmentation characterized by numerous small catchment basins and divide lines. These are often not desired and one needs a way to get around this problem. Basically there are two ways to deal with this problem; *the watershed by markers* and *the hierarchical watershed*.

Concerning the first method, the solution is to “simply” pierce the surface at only the relevant minima, called markers. This may seem odd, as too find an object, one first has to know where it is. But in fact in object recognition one always needs prior information, in order to extract the desired object. In the case of the watershed by markers, one only needs a rough position of the object/minima. All other minima need not to be taken into account in the flooding procedure. If there is a background then this only needs one unique tag number for it.

Depending on the algorithmic implementation the superfluous minima are either just overflooded from the neighboring catchment basin without a dam being build between them. Or in other cases, before starting the flood, a homotopic alteration of the image is done. In such

a procedure all the irrelevant minima are filled up, i.e. they become plateaus and thus they are ignored in the flooding procedure. This is called swamping or reconstruction by a marker function.

The other solution is to take the oversegmented image and reapply the watershed on the segmented image again. The basis for this process is, that although the images contains many irrelevant lines the relevant watersheds will be present in the oversegmented image. Then by repeatably applying the transform one tries to over flood the irrelevant ones. This process results in a successive simplification of the image, and is called the watershed hierarchy.

Usually the scheme of this method is as follows; first apply the watershed on a image. Ascribe to each pixel, associated with a particular catchment basin, the value of the minimum grayscale value in that catchment basin. This yields a mosaic image and for further refinement the watershed can be reapplied to the gradient of the mosaic image. This will result in a segmented image with same boundaries as the previous on, except the boundaries which are associated with smallest change in gray level have disappeared. This process can be iterated upon, until the desired image is obtained.

In the previous scheme only at the difference of two basin minima is looked upon, but it can be generalized to other parameters. This can be done by constructing an adjacency graph. Such a graph connects each basin with its neighboring basin via the boundary between the two basins. Then according to some parameter defined upon the boundary or the basin, two neighboring basins can be united. This will yield a new mosaic image, and again it may be iterated upon.

5.6 Discrete point distributions and continuous density fields

The watershed method discussed here only works on gray-scale images, therefore the point distribution (galaxies/particles) need to be interpolated on a grid. In N-body simulations the point distribution is a Monte-Carlo representation of the underlying density field. To each particle a certain amount of mass associated, and thus the density is proportional to the number of particles in a given volume. Then the problem of interpolation is choosing a volume-shape that bins these particles in such a way that there are enough particles in the bin in order to suppress the shot noise. In fixed grid methods one has to choose a fine enough grid to retrieve the most information out of the underlying field. But a very fine grid will maximize the noise. Especially, in low density regions one is sensitive to this noise, since there are very few particles that represent the field.

Besides TSC there are various other interpolation techniques, SPH and DTFE are examples of these techniques. In chapter 6 will analyze the watershed technique on TSC method. While in chapter 7 we will apply the method on a DTFE reconstructed density field.

5.7 Extensions to three dimensions

Here we only use the 2D version of the algorithm, but the above discussion is valid in any dimension. And the watershed method has been extended to the 3dimensional case. We expect that the advantages and behavior of the 2D case as will be discussed below, also applies to the 3D case. However the extension to 3 dimensions will be left for future work.

Chapter 6

Segmentation: the Kinematic Voronoi Model, a testcase

Our goal is to use the watershed transform as a void finder. Considering the advantages of the transform (see also Beucher and Meyer(1990)), the watershed transform could have several advantages with respect to other void finders;

- The watershed naturally place the divide lines on the crests of a field, and although a void boundary might be distorted the watershed transform will detect the boundary of a void.
- It naturally produces closed contours. Therefore, as long as the minima are well chosen, the transform will not be sensitive to local protrusions between two adjacent voids.
- The watershed works directly on the topology of the field. Thus it does not rely on a geometrical predefined shape. So the voids found can have every shape.
- In the case of an ideal smooth density field, it will find the possible voids in parameter free way. And no predefined values have to be introduced.

To test the watershed method it will be applied to kinematic voronoi model. In this models one knows where the voids are. Therefore the voronoi model is the ideal testcase for the watershed method.

6.1 Kinematic Voronoi Model

The kinematic voronoi model is a non-linear model of structure formation, where voids are the organizers of the foam. It assumes that the cosmic foam resembles a 3D voronoi tessellation, and each voronoi cell center corresponds to an individual void. Furthermore a voronoi tessellation exists of faces, edges and nodes. These would correspond to the walls, filaments and clusters in the galaxy distribution.

The physical motivation for this model is as follows (see also SW04 and Colberg in prep.). Suppose that the initial density field consisted of minima that are of almost same depth and have approximately the same distance. Due to their underdensity the particles in the voids feel an outward force, and the particles will evacuate the void. As the void have the same depth the particles of neighboring voids will approximately meet half way between two minima. As more and more particles accumulate this will form a plane between two voids, the face of a voronoi cell.

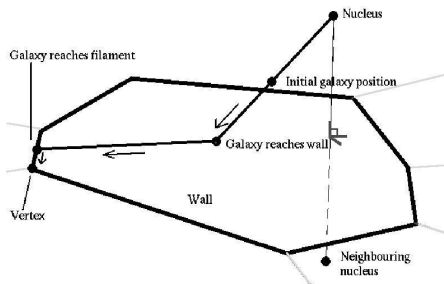


Figure 6.1: The figure shows a voronoi edge, that bisects space between two neighboring nuclei/voids. It also shows the trajectory of a particle in the kinematic voronoi model. Sequentially the particle evacuates the voids, collides at a face, leaves this wall towards the nearest filament and finally ends up at a vertex. Courtesy: Jacco Dankers

as time continues more and more particles have evacuated the void, decreasing the cell filling factor, and increasing the amount of particles in the clusters/nodes.

In the plane the particles will still experience a transverse force. Because the outward force of two voids does not completely cancel each other out. Only at the line connecting two voronoi cells, the forces are in exactly the same and opposite direction. The other particles in the plane will move away from this point, and thus move to the edge of the plane, see figure 6.1. Eventually the particles reach the edge of the void and again the particles will evacuate to a node. This thus provides a natural explanation for the existence of a cosmic foam made up of voids, walls, filaments and clusters.

A realization of such a model can be seen in figure 6.1. It shows slices through four different boxes of $141 h^{-1}\text{Mpc}$ size. Each box has 180 voronoi cells and 128^3 of particles. In each realization the nodes are in the same position, and only differ in cell filling factor. This decreases from right to left and top to bottom. This represents the evolution as described above. Logically,

6.2 Watershed on the Kinematic Voronoi Model

Although the watershed can be extended to 3 dimensions, and has been proven successful in segmenting 3D medical images. In this papers only the 2 dimensional version is used. In principal going to 3 dimension only involves a change of the connectivity from 2d neighboring pixels to 3d voxels. The 3 dimensional case will be left to future work. We expect that the discussion here, can be directly translated to the three dimensional case. As the segmentation in 3 dimensions does not introduce any new situations.

The watershed only works on a density field, therefore the intensity of the particles has to be interpolated to a fixed grid. This is done using the triangular shaped cloud method, TSC. For the description of this method, see chapter ???. The interpolation was done on two different resolutions, resp. a 64^3 and a 128^3 grid. An example of the outcome of such an interpolation is shown in figure 6.2. For the 128 cubed grid it also shows the particles that are associated with this particular density slice. The density field clearly shows the filaments and nodes as also can be seen in the particle distribution.

However the voids are dominated by noise, as seen by the many islands inside a large zero density ocean. It is evident that the typical void density is too low to be well represented by the interpolated field. Because the typical particle distance is larger than the grid length and therefore the TSC method can not make a smooth field. This thus basically shows that in underdense regions it is very important to use interpolation techniques (SPH or DTFE) that can adapt its kernel to the local environment. In any case the TSC field will not be better than any other method, and therefore it proves as a worstcase scenario for the segmentation method.

Applying the watershed transform directly on the density field, results in a very oversegmented tessellation, see figure 6.2. As described above in section 5.5.2 the significant watersheds are present. These correspond to the divide lines on the red/green filaments, which connect the cluster and surround the voids. Unfortunately, many of the voids are subdivided into small patches. And it is evident from figure 6.2 that the sole cause of this oversegmentation is the noise present in the voids. This noise causes pixel by pixel variation, which in turns results in the appearance of many minima inside the voids. Each of these act as independent flooding

sources for the watershed transform, and these minima then cause the superfluous watershed lines.

For the kinematic voronoi it is known that these minima are not significant, as there is no substructure present within these voids. In this sense the voids in the kinematic voronoi model are the extreme case as in real simulations of structure formation there will be substructure present. This structure, is both due to the hierarchical build up out of smaller voids and thus also due to noise component. If the interpolation method is able to extract substructure inside voids. Then the results of figure 6.2 suggest that watershed method will also detect these. This can be considered as well as an advantage as disadvantage of the watershed segmentation method. The advantage being that one is able to track the build up of voids, which is dynamically very

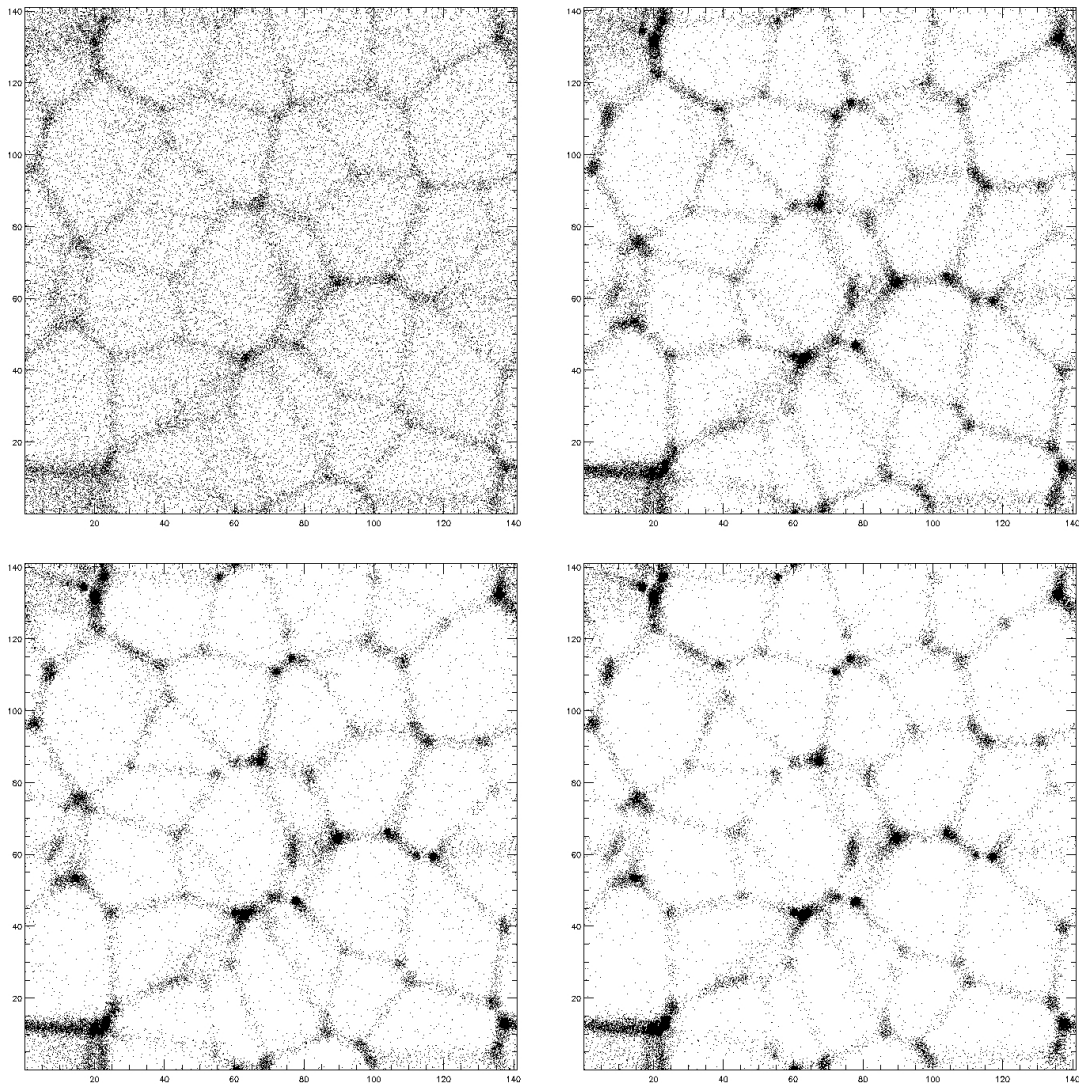


Figure 6.2: These figures show the particles out of a slice through a four different particle distributions. Each slice is at the same position in the box and of the same thickness. The particle realizations are made via the kinematic distributed voronoi model. These differ only in the cell filling factor, which decreases from left to right and top to bottom.

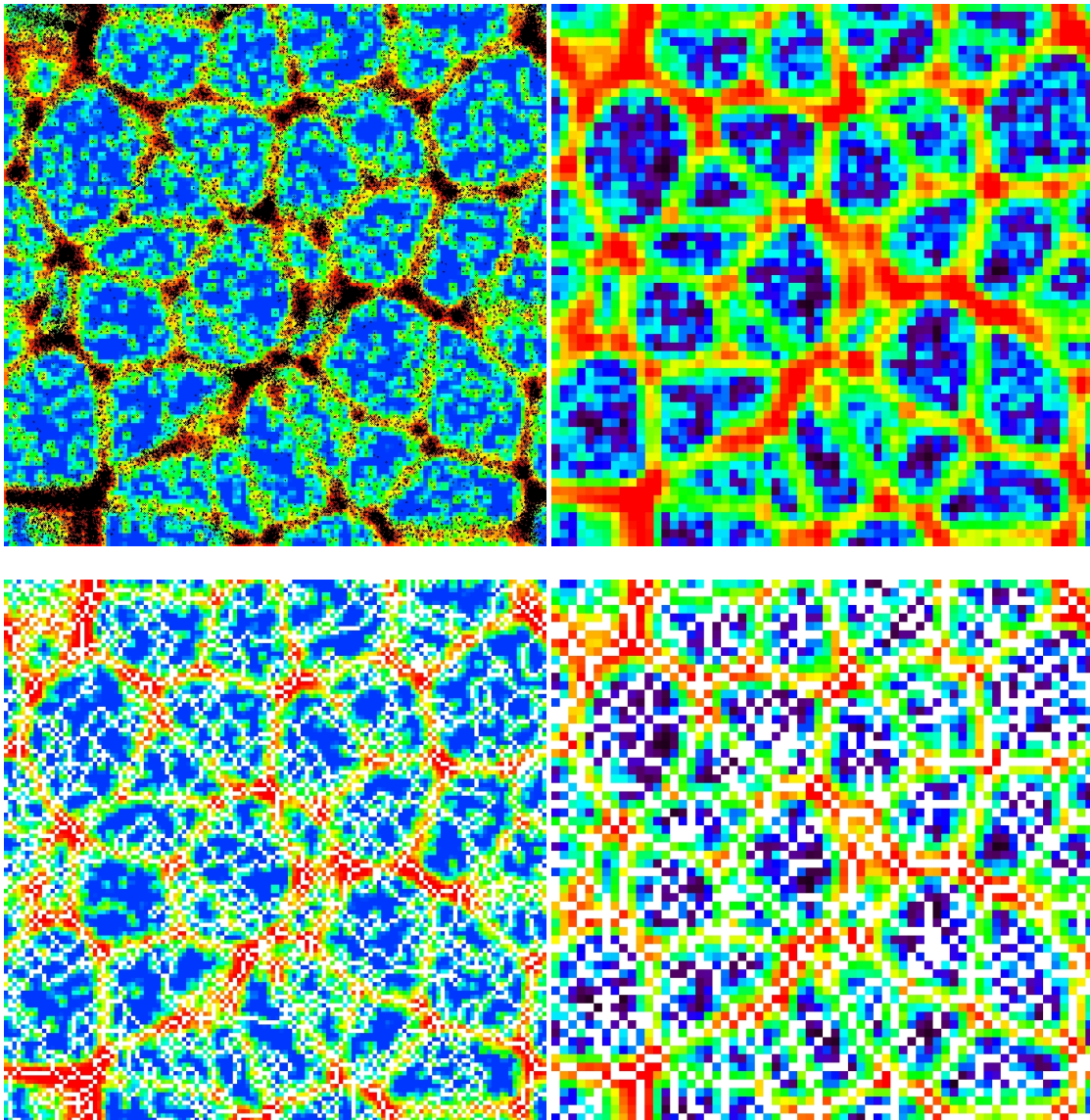


Figure 6.3: The top two images show slices of the interpolated density field at two different resolutions resp. 128 cubed grid and 64 grid. The particles are from the third voronoi model plotted in figure 6.1. The interpolation was done via the triangular shaped cloud method. For the highest resolution the particles that approximately contribute to the slice are over plotted as well. The bottom row shows the resulting oversegmented segmentation after applying the watershed transform.

interesting. On the other hand, if one is interested in the void population the catchment basins of the subvoids have to be suppressed. This last applies ofcourse always to the noise component.

6.2.1 Smoothing

To eliminate the noise the following method is presented. As can be seen in figure 6.2 the noise in the voids has a large salt and pepper appearance. It has been shown that a morphological filtering by openings and closings is very efficient in removing this kind of noise. Therefore before

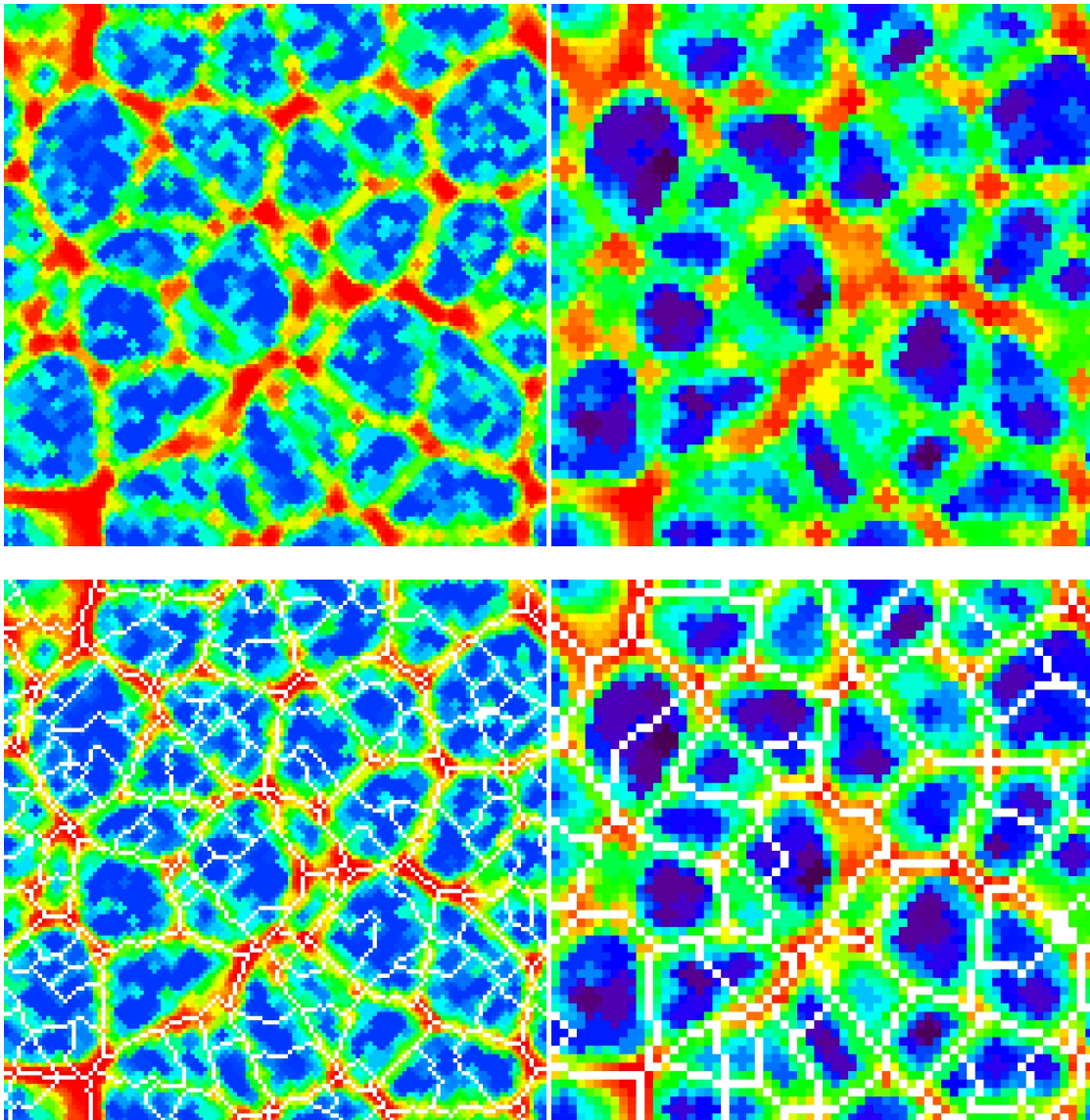


Figure 6.4: The top figures shows the smoothed density fields with a one pixel radius structure element. The left image corresponds to the 128 grid image and the right image to the 64 grid as is also shown in figure 6.2. The improved segmentation that results after this smoothing is shown in the bottom pictures for the fields.

applying the watershed, the density field is morphologically smoothed with an opening and a closing of a disk of one pixel radius. This can be seen in figure 6.2. A large part of the noise has been taken out, and subsequently the segmentations are already much better. Still there remain some divide lines within the voids, that have to be taken out as well.

A possibility is to use a larger structure elements that can eliminate more noise. However the trade off of a larger filtering is that the useful information is also lost. This can be seen fig.(6.2.1), these show the particles, the filtered density field and the segmentation of the 128 grid field. The filtering radius increases from left to right, respectively from 1.5 pixel radius (box of 9 pixels) to 2 and 3. Although with each step more of the oversegmented lines vanish, also

some of the weaker divide lines between voids are lost as well. Moreover some of the smaller voids have completely disappeared as they are filled up. This is especially well seen in the last image. Another effect, that a large smoothing will have is that the accuracy of the divide lines diminishes. This effect can also be seen in the middle part of the last figure where some divide lines are shifted with respect to the particles. So although the oversegmented lines have vanished with more smoothing, it causes an under-segmentation of the real underlying density field. In figures 6.2.1 the same effects can be seen in the 64 grid density field, and they are more pronounced due to the coarser resolution. Therefore a large smoothing can not be regarded as the optimal way to get rid of the oversegmented lines.

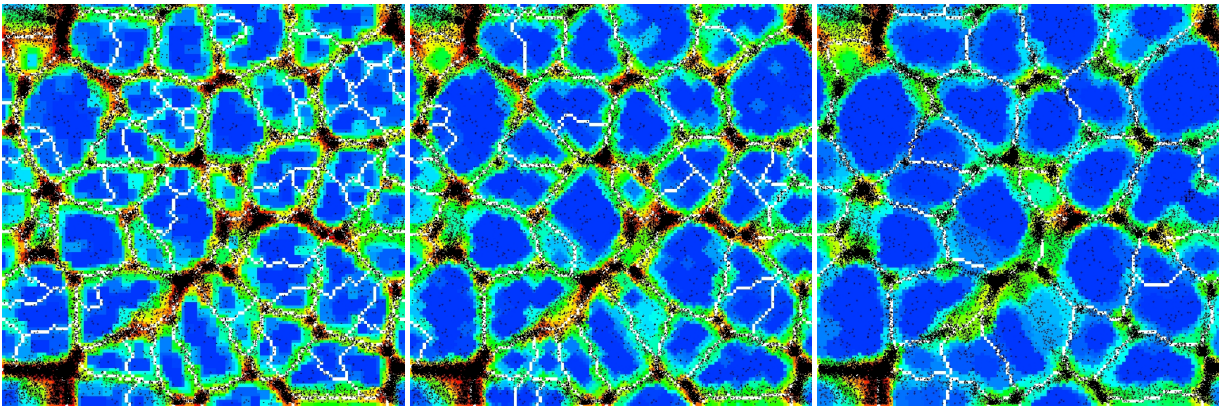


Figure 6.5: The effect that smoothing has on the 128 resolution density field is plotted. From left to right the structuring element increases from resp. 1.5, 2.0 and 3.0 pixels radii. Also plotted is the segmentation and the particles. Comparing these to figure 6.2 concludes that, while the oversegmentation vanishes, unfortunately also some of the real divide lines are lost as well with the smoothing.

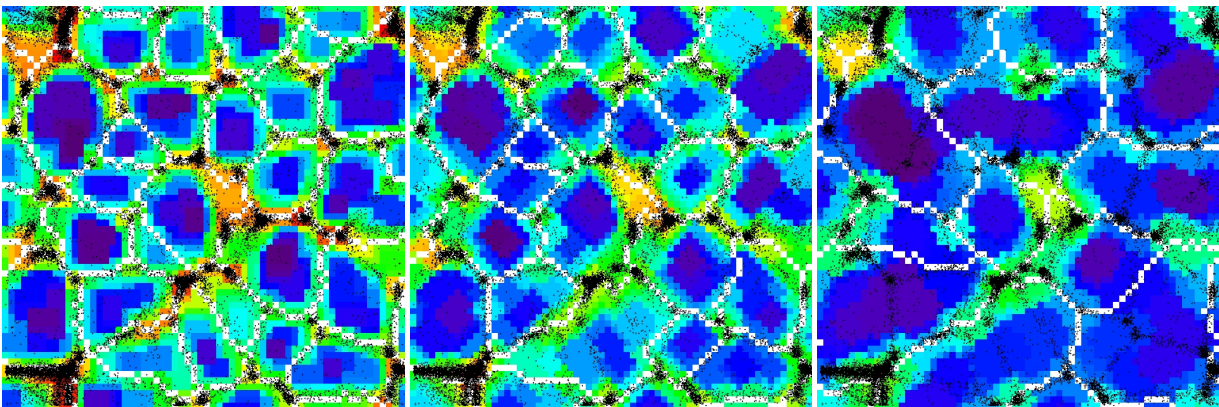


Figure 6.6: This shows the same sequence of images as in figure 6.2.1, only then for the 64 grid density field. The drawback of a large smoothing radius is clearly indicated. As with every step more and more of the true divide lines vanish. Finally yielding in the last image a segmentation that has hardly any correspondence with the particles.

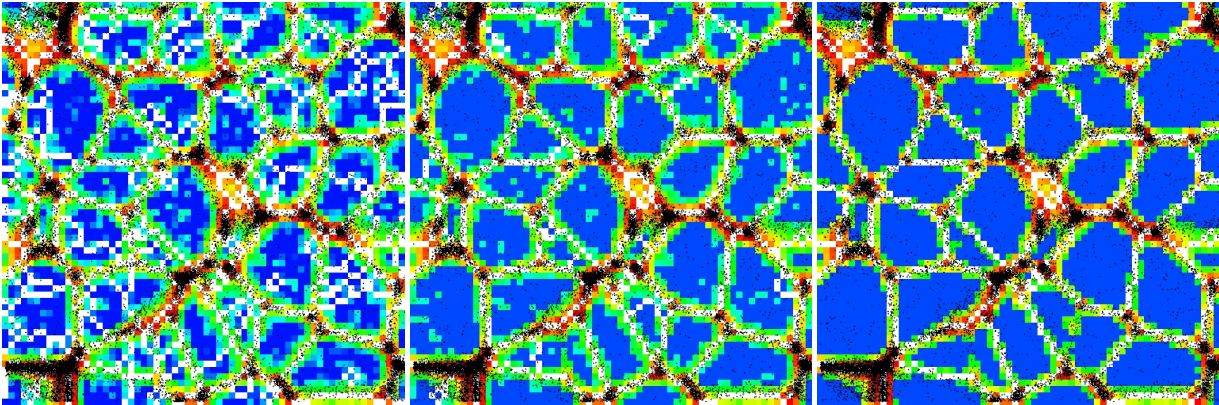


Figure 6.7: The 64-grid density field is plotted, which is truncated at three increasing density levels. As indicated in figure 6.2.2 these are at $\delta\rho$ of 0.05, 0.1 and 0.2. Comparing this to the original segmentation of 6.2 shows that thresholding is quite effective in removing oversegmentation. The last figure shows that the threshold can not be chosen too high, as the true divide lines may break up too.

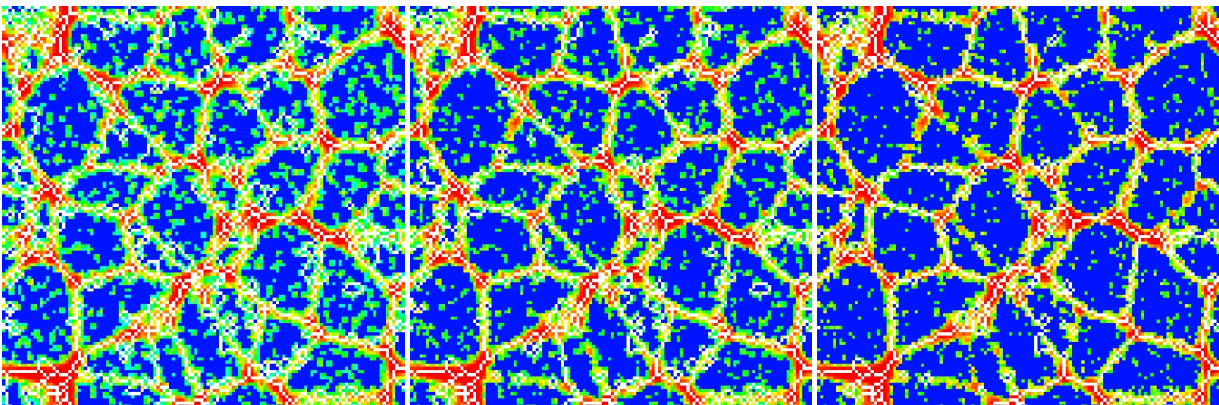


Figure 6.8: The truncation series is plotted but then for the 128 grid. Again thresholding yields already much better images if compared to the original. But still due to pixel-by-pixel variations in the denser areas, the segmentation is not optimal yet. Also the break up of filaments occurs as with the 64 grid field.

6.2.2 Thresholding

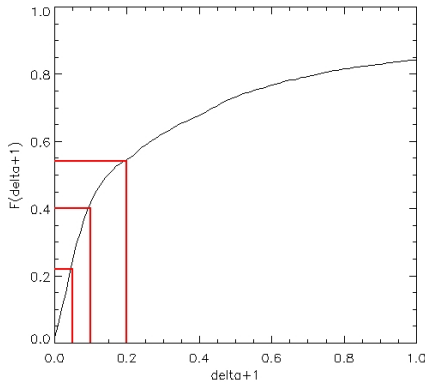


Figure 6.9: The figure shows the cumulative probability function of the density field (64-grid). The red lines indicate three thresholds at a $\delta\rho$ of 0.05, 0.1 and 0.2. The volume that is taken away can be read of from the y-axis, and this approximately corresponds to 20, 40 and 50 percent of the density field.

As the voids are more prone to noise, just by the fact that in these regions there are far fewer particles, and therefore there are far fewer particles to average over. Can it therefore be possible to throw away part of the density field, so to get a cleaner field? A simple and perhaps crude way to do this is by thresholding the image and hope that part of the noise component is removed. In this way it is expected that the surplus of minima in voids have merged into one contiguous minima region. Therefore the flooding will start out on a higher grayscale level, and the unified minima will act as unique flooding source. In some sense this can be regarded as a swamping of the low level regions, much like is done in marker based segmentation.

For the thresholding procedure, the density field of figure 6.2 is used again. The cumulative distribution of the density (only 64 grid) and the threshold values are shown in figure 6.2.2. These thresholds remove everything below a $\delta\rho$ of 0.05, 0.1 and 0.2. And as indicated with the red lines in figure 6.2.2, this approximately corresponds to 20, 40 and 50 percent of the field. The effect that this has on the segmentation is seen in the following series of images figures 6.2.1 and 6.2.1. Again the density field, the particles and the segmentation are

plotted.

From the resulting segmentations we conclude that thresholding is quite effective in removing the oversegmented lines. As the last figure of 6.2.1 already shows approximately the correct segmentation. However, some of the real divide lines are broken up by the threshold, causing an unintended percolation into a neighboring void. Which resulted in the unification of the voids into one catchment basin. Clearly, to avoid this from happening the threshold should be chosen conservative. The trade off is then that not all the noise minima are unified.

6.2.3 Thresholding and Smoothing

The results of the previous two section suggest that perhaps a mild thresholding followed by a smoothing can remove most of the noise components in the density field. Yet leaving the filaments unharmed and preventing the voids from merging. The results of such a procedure is shown in the following set of figures ???. These figures show the best segmentations possibly obtained with a combination of thresholding and smoothing of the density field. This was done for both resolutions, for comparison the particles are plotted aside the segmentations, also the nuclei of the voronoi cells are plotted.

The results can be summarized as follows. Firstly the method has retrieved NEARLY all the voids in the two dimensional density field. Where this is not so, this was due to small contrast of the edge with to respect to the void particles. In case of the low resolution field not all small voids where resolved and therefore could not be found. This fact is a failure of the interpolation method, again indicating the need of a well defined field.

Secondly the oversegmentation problem has been minimized substantially, though could not completely be suppressed. Especially in narrow regions the void-finding method has a tendency to split voids up in to several pieces. This is due to noise, causing the appearance of fiducial filaments between two neighboring edges. These closings can be clearly seen in the density fields.

Considering these two results, we note the following; In order to get the best results of the watershed void identification method, it is important that the noise in low density areas is minimized. As this may cause the formation of many minima and spurious closings. Moreover as filaments are the boundaries of the voids, the interpolation method needs to be able to resolve these anisotropic features. The only density interpolation methods that are able to do this is DTFE and SPH. Pelupussy (2004), Schaap (2005) & Schaap & van de Weygaert (2005) compare the DTFE method with SPH and TSC interpolation methods. They conclude that DTFE is superior in reconstructing the density field in voids and resolving anisotropic features as filaments. On the basis of these studies it has become clear that the best representation of the density field is that defined by the DTFE method. It has been shown to be highly successful in retaining the substructures in the cosmic matter distribution, while at the same time keeping close to the anisotropic morphology of the cosmic web. Moreover, through its interpolation it manages to suppress the shot noise in the low-density regions, and has been successful in detecting the typical and theoretically expected " *inverse tophat shape*" and " *superhubble flow*" of voids in N-body simulations.

Here only a 2D slice was considered to find voids. Ultimately, the watershed method has to be extended to 3 dimensions. On this account we want to note that this might give an advantage and a disadvantage. Considering the oversegmented lines originating from artificial closings. This will probably be less of a problem, because it is in 3 dimensions more difficult to form closed cavities by noise alone. While in 2 dimensions it is more easier to separate an underdense region into two or more different parts. On that same account one probably has to be more careful with percolation due to thresholding. Besides these two points, we do not expect any further complications.

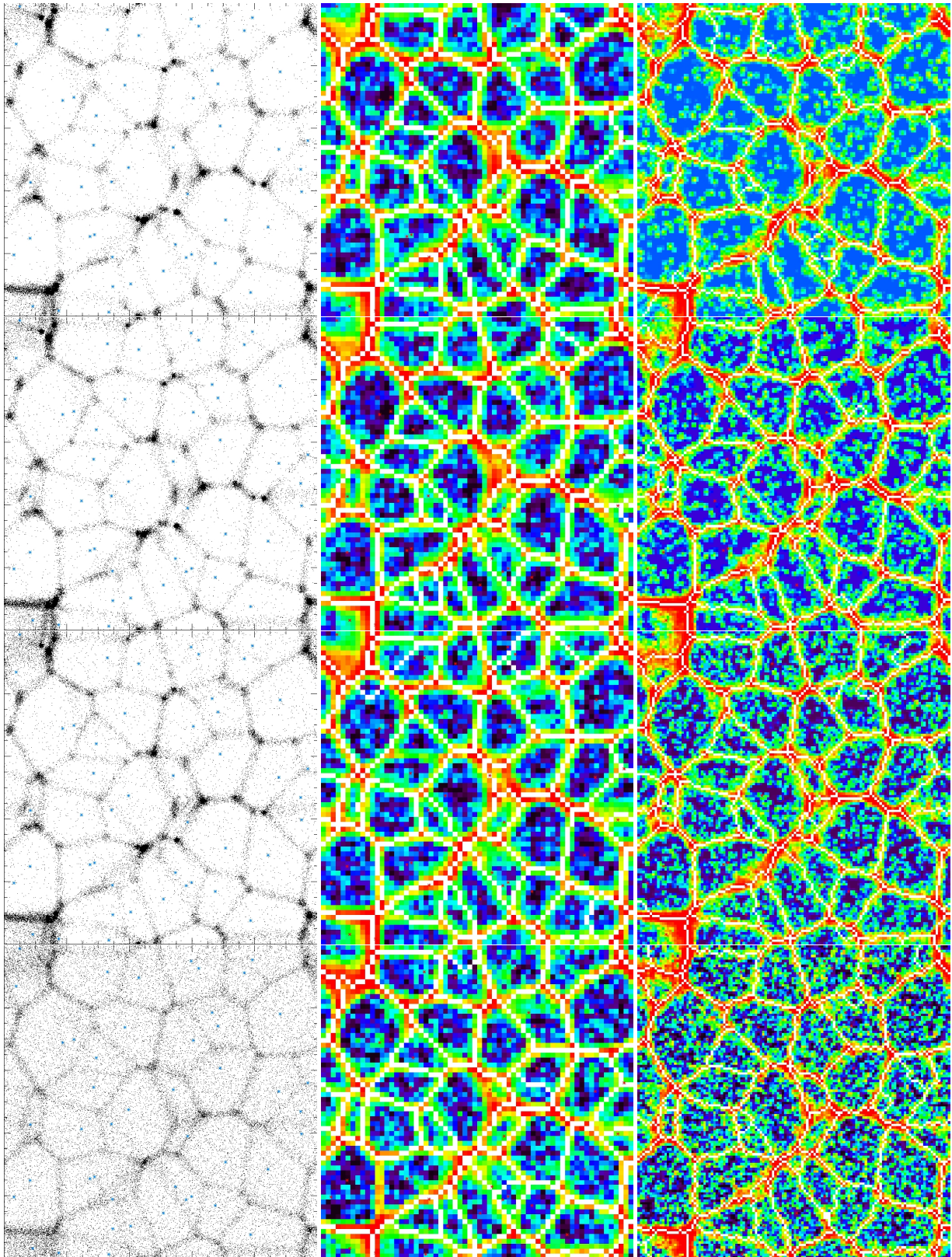


Figure 6.10: The truncation and smoothing series is plotted but then for both resolution. Again thresholding yields already much better images if compared to the original. But still due to pixel-by-pixel variations in the denser areas, the segmentation is not optimal yet. Also the break up of filaments occurs as with the 64 grid field.

Chapter 7

Segmentation, the “real” world

In this section we describe an application of the WST to a Λ CDM Universe density field slice, these were kindly made available by W.Schaap. The simulations were made by the VIRGO consortium, and in particular here the Λ CDM GIF simulation set from Jenkins (1998) and Kauffmann (1999) were used. The simulation box has a size of 141 Mpc h^{-1} and contains $(256)^3$ number of particles. All of the important parameters of the simulation are shown in the table 7. Note that this closely resembles the values of the concordance model. In this model about a third of

Model	Λ CDM sim.
Boxsize	141.3 Mpc/h
Particles	256^3
Γ	0.21
Ω	0.3
Λ	0.7
H0	70 km/(Mpc s)
σ_8	0.9
Mass	$1.4 \times 10^{10} M_{\odot}/h$

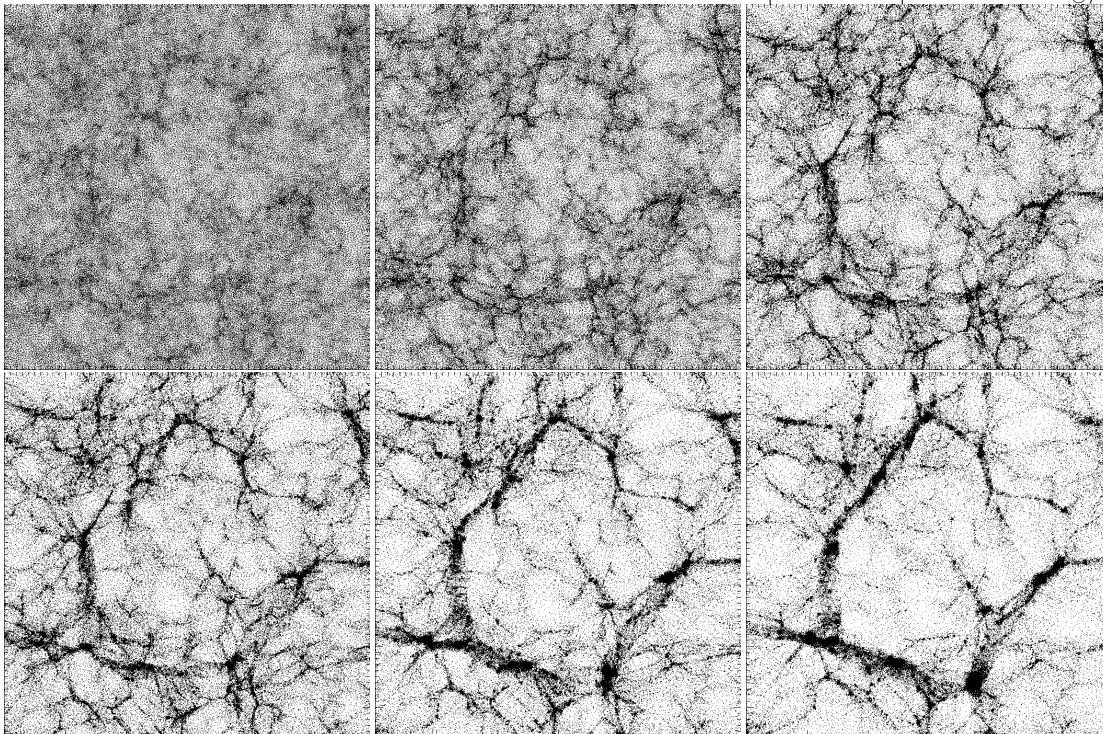


Figure 7.1: The figure shows the formation of a large void in the GIF simulation. It shows a zoom on middle section of slices shown in figure 7.

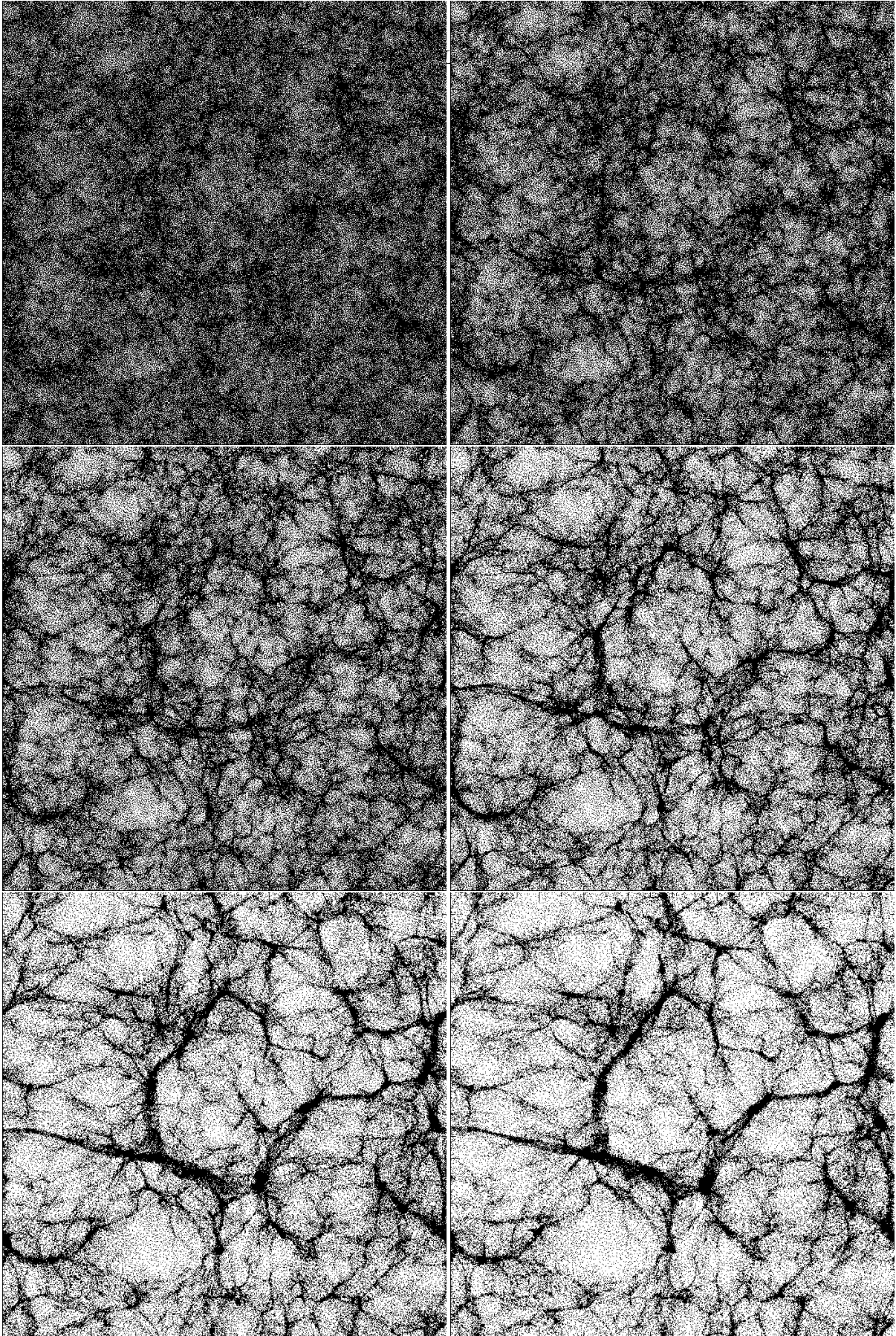


Figure 7.2: These slices show the particles out of the GIF Λ CDM simulation on six different time steps. They represent a slice of 5.6 Mpc h^{-1} thickness in the middle of the box, which is of 141 Mpc h^{-1} in size. The redshifts of these slices are from left to right and top to bottom, resp. $z=10, 5, 3, 1.5, 0.42, 0$. The evolution of the large scale structure can be readily traced.

the energy density is contributed by ordinary matter and dark matter. The other 70 percent is dark energy with the index of the equation equal to minus one, so that it is true a *constant*. Furthermore a hubble parameter h of 0.7 and a spectrum normalization parameter of 0.9 were used for these simulations. The parameters are thus more or less in agreement with recent findings of Bennet et al. (2003), 2dFGRS consortium and the SDSS people.

7.1 GIF density field

The interpolated field was made using the Delaunay Tessellation Field Estimator (DTFE) (see Schaap & van de Weygaert 2000) of the output particles at $z = 3$. The field was obtained by extracting a thick slab of particles around the density slice position. Then the delaunay triangulation was constructed and subsequently these triangles were used to interpolate back on the nodes of the slice. Figure 7.3 shows the density field of the simulation at three slices in the middle of the box. These slices are resp. perpendicular to the y,z and x axis and have a resolution of 512 by 512 nodes (xz - and xy -slice) and 1024 by 1024 nodes (yz -slice).

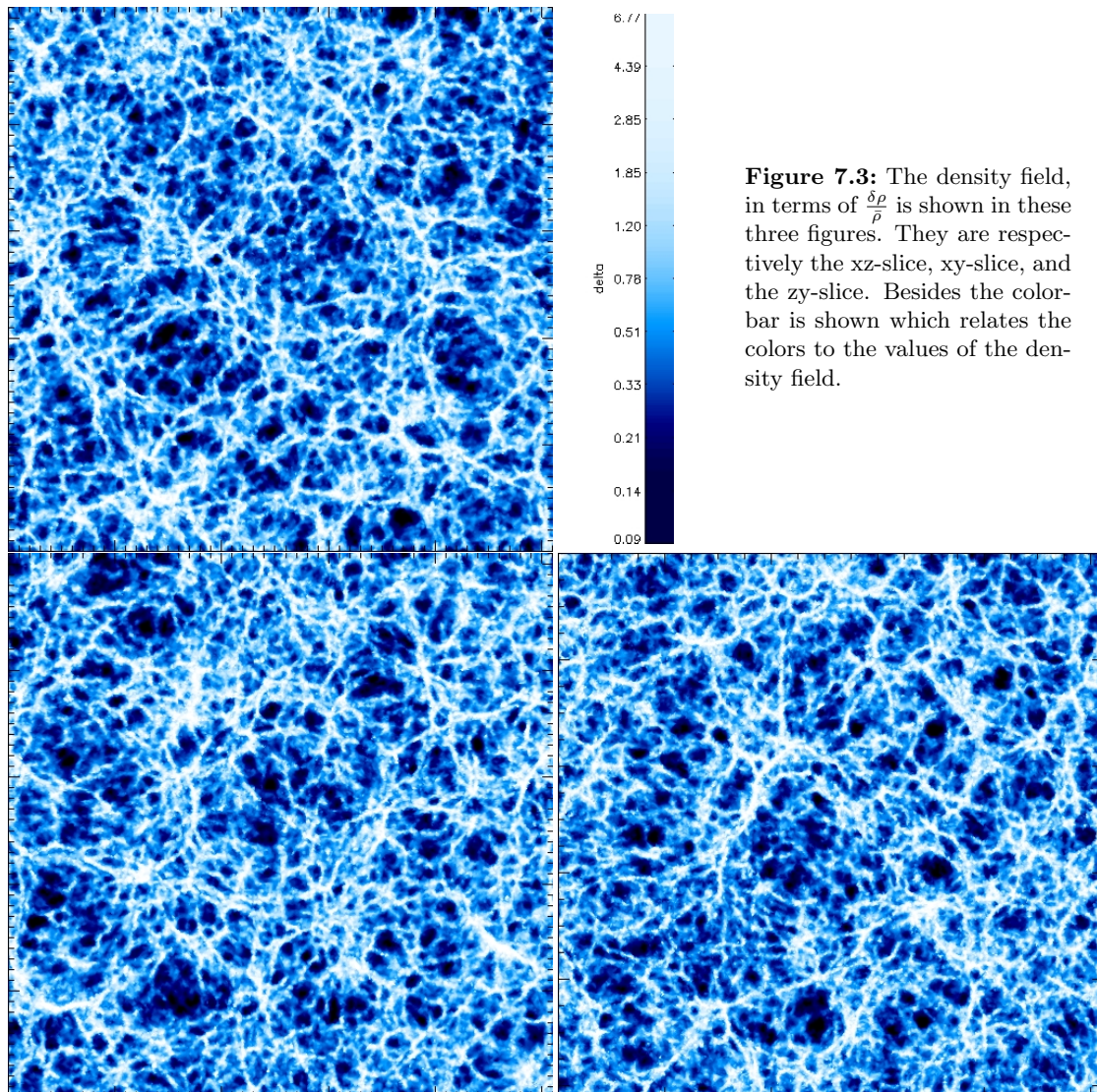


Figure 7.3: The density field, in terms of $\frac{\delta\rho}{\rho}$ is shown in these three figures. They are respectively the xz -slice, xy -slice, and the yz -slice. Besides the color-bar is shown which relates the colors to the values of the density field.

To illustrate the void hierarchy in this simulation and the capability of DTFE in retrieving the density field over the whole density range. Figure 7.4 shows the void hierarchy in four consecutive zooms on a patch of the yz -slice. The first image shows the entire density field, but truncated at about a $\delta\rho$ of unity. This basically shows all the overdense regions present in the slice. Furthermore it shows that underdense regions are almost connected into one region. This is topologically analogous to overdense islands in a large underdense ocean. Thus the voids are delineated by a tenuous foam often perforated by gaps, which gives the field an erratic appearance. A careful look even reveals larger non-empty voids, that are outlined by large coherent filamentary chain of islands, which surround regions of smaller islands. These voids have abundant amounts of small substructure within them. Most likely due to the fact that these large voids are still in the early linear stages at $z = 3$. And as such they would still contain lots of substructure, this has not evacuated the largest voids yet. Examples of such large filled voids can be seen inside the region delineated by the orange box. At the lower left corner, upper right and the lower right corners the first imprints of three large voids can be seen.

Important Note: When analyzing isolated 2d slices out of a 3d field projection effects may create fiducial smaller voids. As these smaller voids can be produced by cutting through substructure on the edge of large voids. In reality, i.e. three dimensions, these may be fully connected to larger underdense regions which lie above or below the plane. This consideration has to be kept in mind while looking at these images

The next image on the right shows the zoom on the region outlined by the box of the previous image. With this zoom the threshold was further decreased to a value of 0.7. Although, the difference between the previous image and this one, is not that staggering. There is a slight tendency for various islands to connect themselves. This in turn divides the larger void up into smaller ones. See for example the void in the orange box. The ellipsoidal shaped void is split up in an upper and lower void. This process is more clearly seen in the next zoom, which is accompanied by a further decrease of the threshold to 0.3. The upper and lower void are further split up into even smaller voids delineated by even weaker walls. This can followed into the next zoom. No thresholding was applied on this image, only the contrast was boosted by a decrease of the gamma value of the colormap. This in order to show more details at lower density values inside the voids. The image shows the larger upper voids. The void is split up into three subvoids and numerous smaller voids at the boundary.

7.1.1 Grey levels

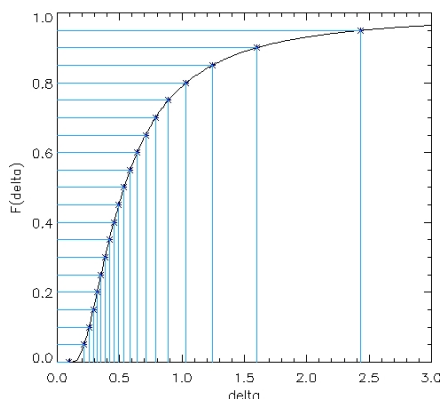


Figure 7.5: This figure shows how the gray levels were chosen. Each the bin in the gray level distribution represents an equal amount of fraction volume in the fluctuation field.

In almost all cases the watershed algorithms can only deal with grayscale images. However, the density field obtained after interpolation is continuous, as it can take every value between zero and infinity. Therefore a binning of the density field into discrete levels is necessary. Many different choices exist for the binning of the density field. For example one may choose linear or logarithmic values to bin the density field.

In our case we have chosen to bin the field according to its cumulative distribution. This ensures that every bin represents equal amount of area in the figure. The advantage of this, is that it gives good resolution for the inner regions of voids and in particular to its substructure and boundaries. The disadvantage is that there are far fewer levels for the overdense regions. However these high values can all be considered as collapsed regions, therefore they take in negligible amount of space. And since the goal is to segment

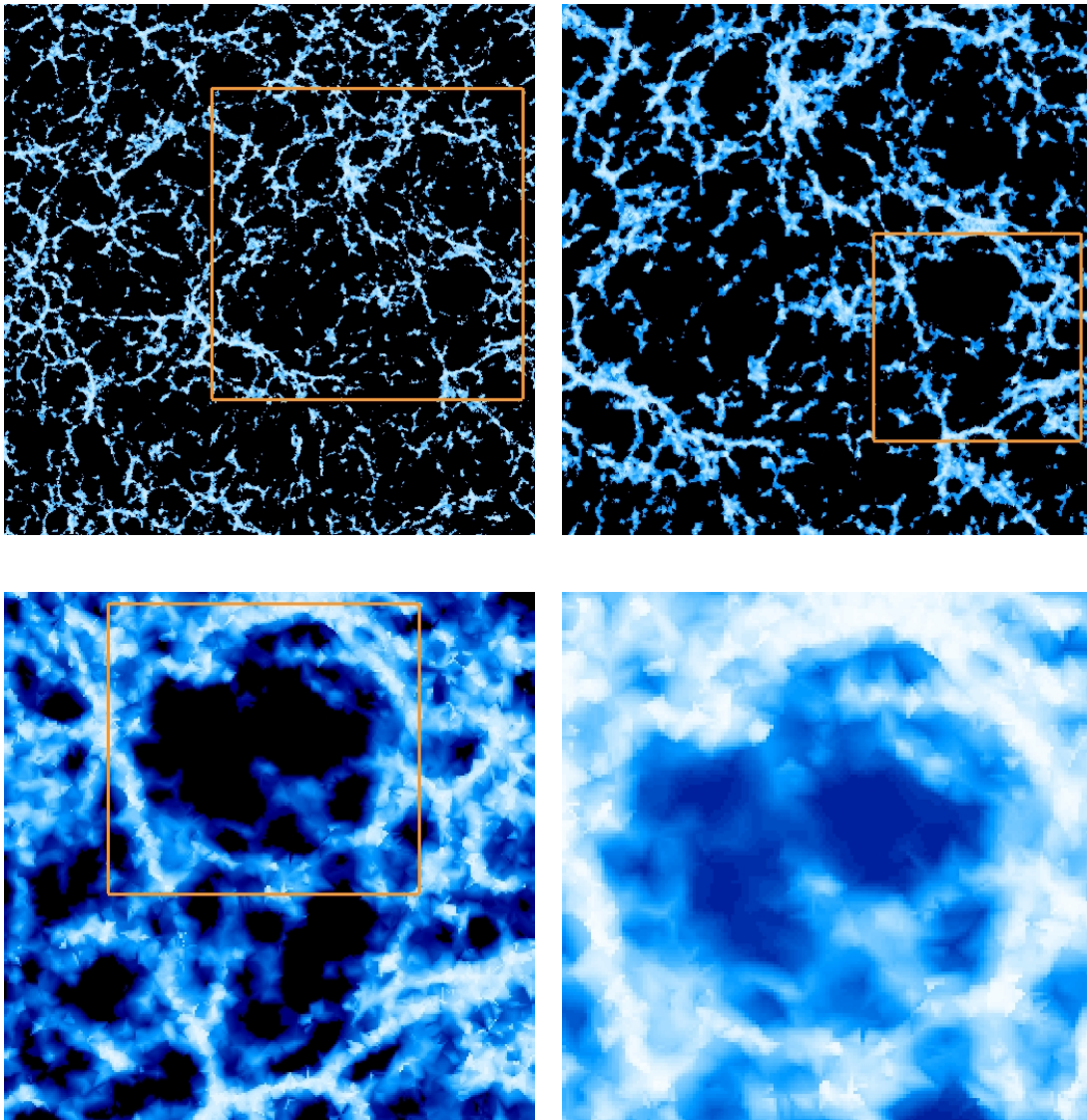


Figure 7.4: The images show the void hierarchy in the yz -slice of the GIF-simulation by means of thresholding and zooming. The color coding is similarly to figure 7.3. Each zoom is indicated with an orange box in the previous image. The first image shows the entire slice, thresholded at the average density, the two following images are thresholded at resp. $\delta\rho$ of 0.7 and 0.3. While the last image is not thresholded, only the contrast is enlarged to lower density values.

these images, it is therefore not necessary to have much resolution at these high levels. In this way we regard a binning via the cumulative distribution as a good choice for the watershed transform.

7.2 GIF Watersheds

We have applied the watershed on the xy -density field, with the gray values as shown above and the standard IDL-package watershed algorithm was used. The result of this is shown in figure 7.6 in the upper left corner. In order to show in more details of the segmentation, we focused on

a blow-up of the middle section of xy-field. The following discussion about this region however does apply to the whole image. Furthermore in order to boost up the contrast, a rainbow color scheme was used. In this scheme the yellow color represents the average density of the Universe, while everything below yellow, i.e. green, blue and darker, is underdense. The ‘warmer’ colors correspond to overdense regions.

The upper right shows the tessellation projected on top of the original image. It confirms the above finding that the watershed method produces oversegmented results. The question is what produces here the oversegmented lines? Two facts can be immediately seen from this figure. Firstly, there are many small watershed regions consisting only of few pixels. Secondly, even though the segmentation is very jiggly, many of the true divide lines are present. A fact which was already was noted above, in the hierarchical oversegmentation section and the kinematical voronoi section.

Clearly, the next goal is to remove these insignificant watershed lines. This is done in the same manner as described above. Indeed many of these very small watershed regions seem to correspond to places where random pixel by pixel variation has produced a local minimum, i.e. this can be considered noise. Therefore a simple removal of spurious minima, defined by only one pixel by morphological smoothing should give a good improvement.

The result of this smoothing is shown in the lower left image of figure 7.6. Comparing this result to the original image on the upper left, shows indeed that the small scale variation has vanished. Then the transform was applied on this “cleaned” image, and the resulting segmentation projected on top of the original image is shown in the lower right image. The correspondence between real topology of the density field and the newly obtained skeleton has dramatically improved by doing this simple step. As can also be seen in figure 7.2, which shows the entire segmented image. The images shows that the watersheds follow the filaments very accurately, and moreover they outline the voids. Although looking at the larger voids one is tempted to say that these are still oversegmented. As for example can be seen in the deep void in the lower left corner. The correspondence between the filaments and the watersheds will be treated in the next section, and in the following section 7.2.2 the subvoids will be treated.

7.2.1 Watersheds and the *Cosmic Skeleton*

Nearly all watershed lines seem to correspond directly to overdense filamentary structures in the density field. This ties in with the definition of the watershed, it locates the divide lines on the crests of the field, i.e. the filaments. One can select a subset of the watershed lines, for example only those that are overdense. The images in figure 7.2.1 stresses this fact by overplotting the segmentation on top of the overdense field. These images are strikingly similar to the *cosmic skeleton*, as found by Novikov et al (in prep). Compare for example their figures 2 and 4 and our figure 7.2.1. Furthermore they use the length of the *skeleton* as statistical tool. This was computed for Gaussian random fields and Zel’dovich maps. They showed that the length of the *skeleton* can be used as a cosmological tool to define non-Gaussianity in the field.

In principle, in the continuous lower complete case, the WST would retrieve the same segmentation as the *skeleton* used by Novikov. This can be easily seen, by comparing the definitions of both methods. The *skeleton*, as used by Novikov et al. is defined by a walk over the ridges of the density field. This walk begins at a local saddle point and then follows the steepest path upward (or vice versa). The path is then found with the following equation of motion,

$$\frac{d\mathbf{r}}{dt} = \nabla\rho. \quad (7.1)$$

The *skeleton* can be calculated by solving this differential equation. This is very similar to watershed definition by topological distance. As can be easily seen from the immersion analogy. The dam construction starts out at a saddle points. As the flooding progresses, the dam will follow the steepest path upward, which is the same path as given by eq.(7.1). In this way these methods are comparable to each other, though by implementation they are different.

Novikov et al. retrieved the *skeleton* by solving for the curvature and the gradient of the density field. These align at the crests of the field, and in this way they connect the saddle point and maxima. This is thus a non-local definition and in this way they estimate the skeleton. However the WST is based on shortest path from a minimum integrated over the whole image. This is thus a local integral definition, while the above use the non-local definition via the derivatives. This means that there can be differences. For example the WST can place divide lines on plateaus that divide two minima, while this would not be done using the above definition for the cosmic *skeleton*. The WST always produces closed contours, which is not the case for the *skeleton*. It is therefore not straightforward to compare these two methods, but it could be a nice followup to see how these relate to each other, and how the length of the watersheds relates to this work.

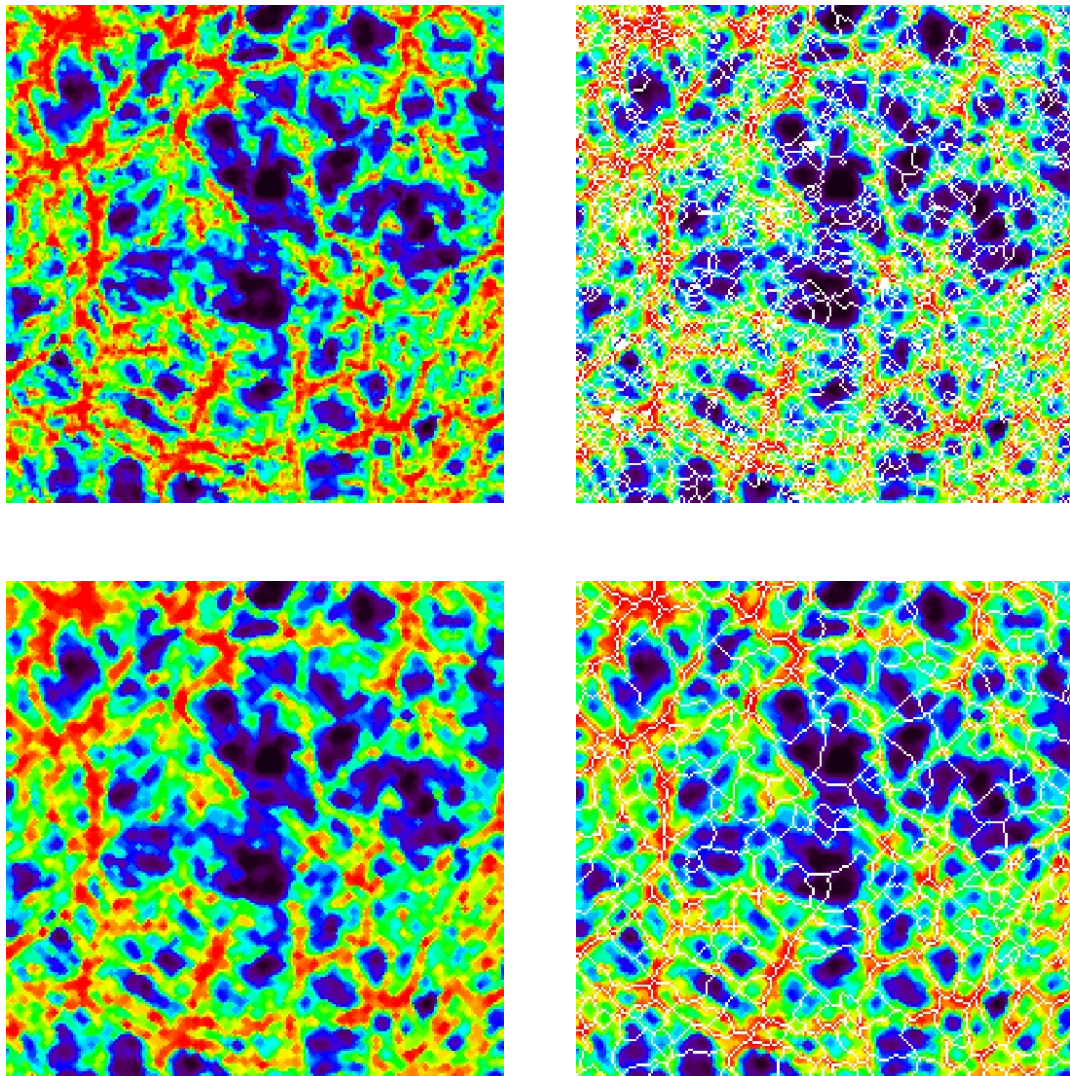


Figure 7.6: The on the left side the density field is shown, and on the right side the resulting segmentation is shown. On the top image no preprocessing was performed, while the lower density field was smoothed with a small structuring element.

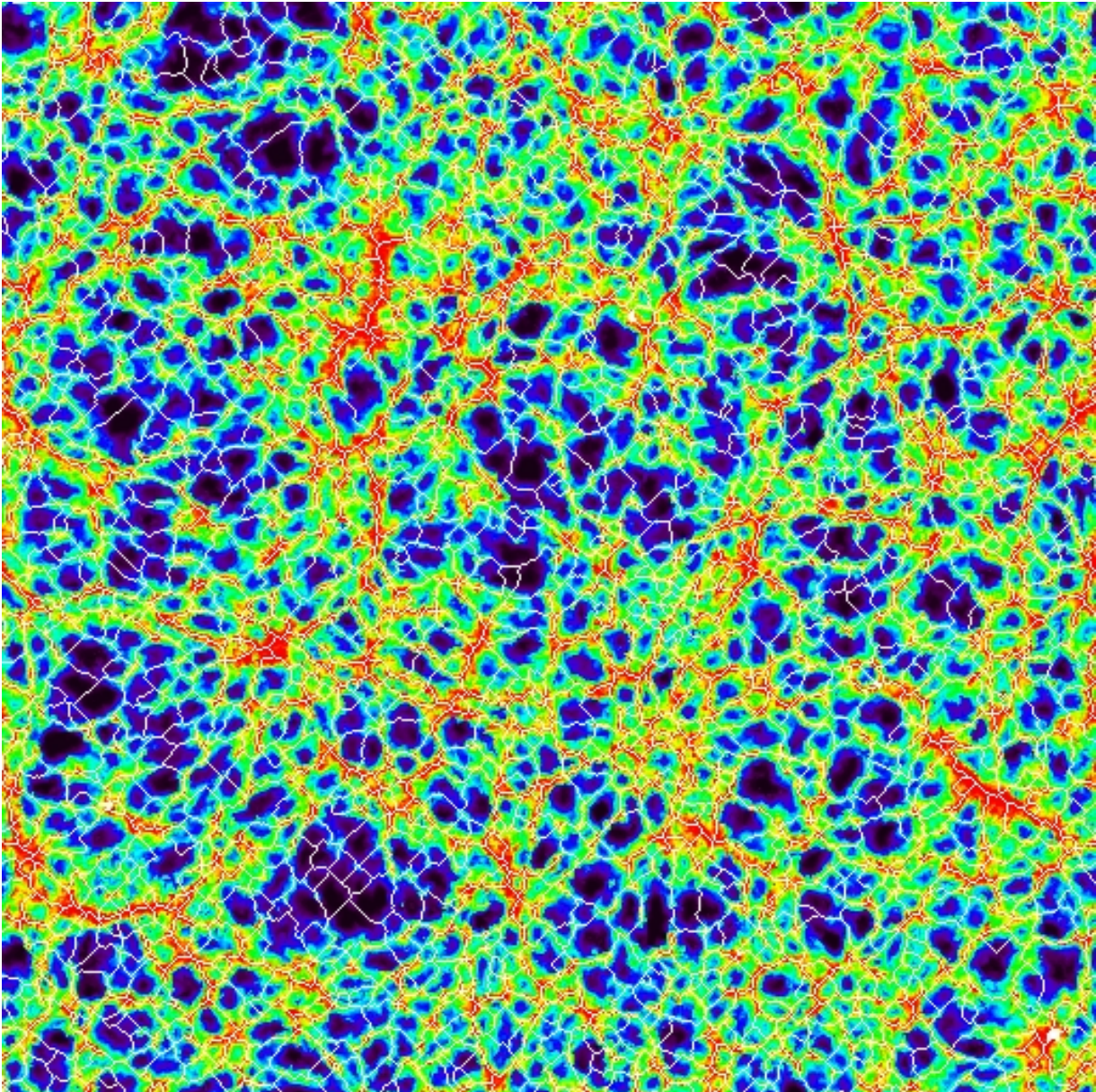


Figure 7.7: The image shows the density image segmented using the watershed transform. Before segmentation the image was morphologically smoothed using the unit disk. The cosmic foam is formed by round underdense voids and the thinly torn filaments.

7.2.2 Watersheds and the *Void Hierarchy*

As seen from the segmented image there still seems to be oversegmentation in the largest voids, as for example in the lower left corner. Only from fig.(7.2) it is not clear where these lines originate from. To investigate this further the upper left image of figure 7.10 shows a zoom of this region. The segmentation is also shown with the figure directly aside of it. In order to show more details inside the void, the levels have been decreased in the same manner as the last image of figure 7.4. Comparing both images shows that there is partly a correspondence between the

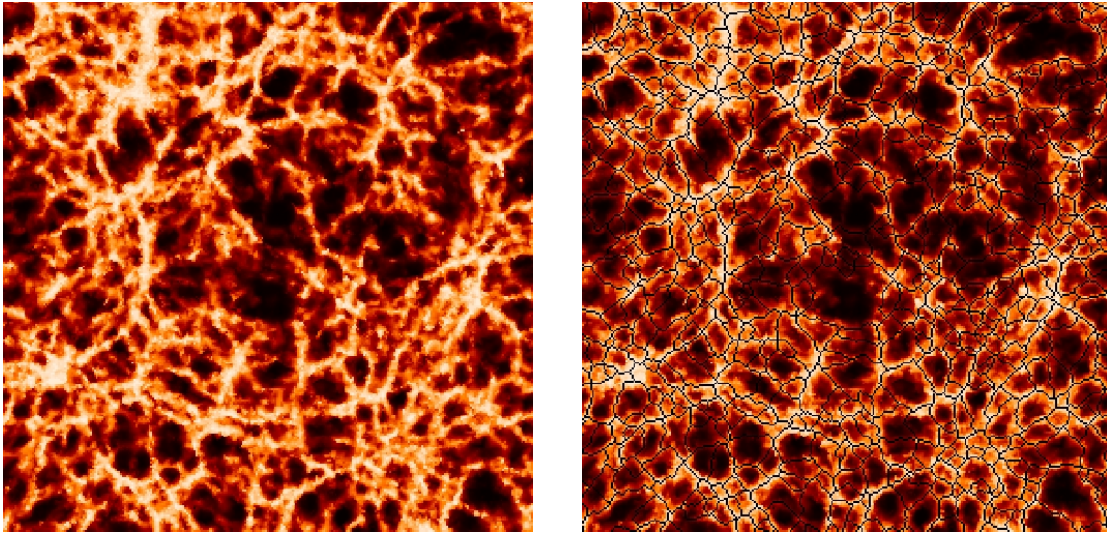


Figure 7.8: The left image shows the density field of the central void in the xy -image. And the right image indicates the skeleton that it has to represent.

substructure in the void and the “oversegmented” lines. This suggests that not only voids are found, but also some of the subvoids, as was expected from the previous chapter. This can be understood from the *void hierarchical* evolution of voids, i.e. where the previous void generation remains lingering inside larger voids.

To see if indeed this is the case, we compare the density field with the particle distribution at earlier times. The right column shows the particles selected out the $z=3$ slice, followed backward and forward in time at three different time steps. The timesteps are respectively at a redshift of 10, 5, and 1, as visible in the first, second and last row. Only at $z=3$ (third row) these particles lie in a plane, for the other timesteps they are projected onto the xy -plane. This is done in order to follow the Lagrangian evolution of the particles that represent the density field at $z=3$. In this way it is possible to follow the evolution of an object.

In the top row the particles at $z=10$ can be compared with the $z=3$ density field (as shown in the top left corner). It shows that the black patches in the larger voids indeed seem to correspond to small dips in the particle distribution at earlier times. Moreover these dips have further evolved in the $z=5$ slice, as can be seen in the second row. This process continues and they are still identifiable at $z=1$. To be absolutely conclusive it remains to be checked whether all the dips correspond to voids at earlier via the density and velocity field. For now, we will conclude that if this is the case, with the watershed method and DTFE interpolation method, we are for the first time able to quantify and follow the void merging process.

To get a good division of the density field into voids, the subvoids have to be suppressed. As seen in the previous chapter thresholding can provide a good way to do so. Because with a mild threshold the minima of the subvoids are taken out of the image and unified into one connected minimum. A first natural choice for this threshold value, is $\delta = -0.78$ or $\delta\rho$ of 0.22. As this corresponds to the shell-crossing time for voids, therefore any connected region below this level belongs to the same void. The result of this is shown in the second row of fig.(7.10) and shows that five watersheds in the center have merged.

Whether this reduction is enough or that more of the watershed areas have to be merged is arguable. For example, if one defines a void as a continuous underdense region. A visual inspection of this void thresholded at a value of 0.5 in the bottom left corner of figure 7.10, indicates that perhaps more watershed areas on the outer edge have to be merged. The two

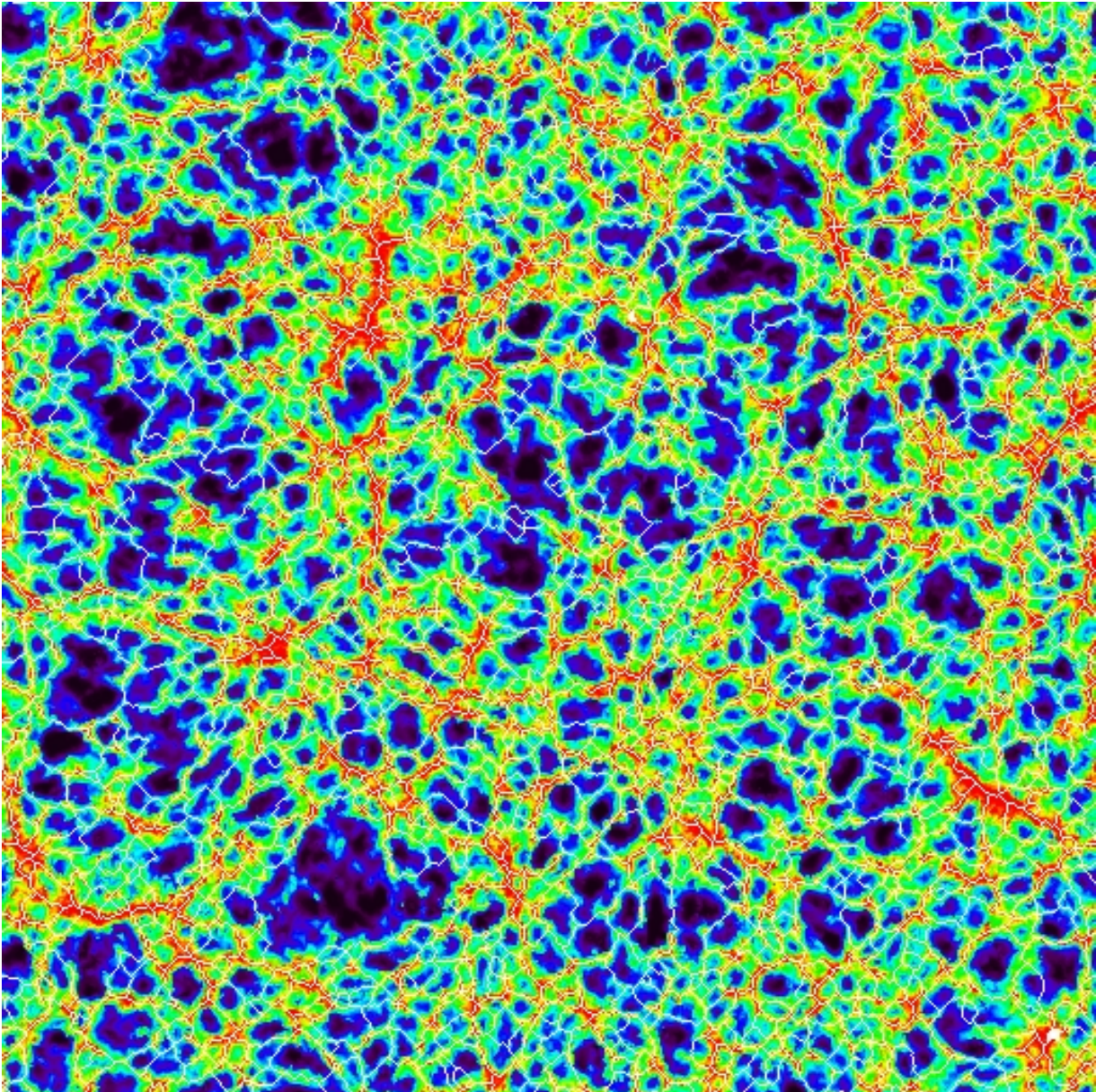


Figure 7.9: The image shows the density image segmented using the watershed transform. Before segmentation the image was morphologically smoothed using the unit disk. The cosmic foam is formed by round underdense voids and the thinly torn filaments.

bottom rows of figure 7.10 shows the behavior of the segmentation when the threshold is further increased to 0.3 and 0.5. It shows an outward merging process as more and more watershed areas are united in one underdense region. Note that this looks very reminiscent of the build up of voids in a hierarchical scenario. Finally, above a value 0.5 the voids in this regions percolate at the lower bottom and upper right corner. In fact for the large void at the central region of the slice this process starts even earlier at about a value of 0.3. Therefore in the following analysis a value of 0.3 was chosen to suppress most of the subvoids, but to keep various larger voids from

percolating. The total result of this threshold is shown in figure 7.2.2. It can be compared to figure 7.2 and this shows indeed that most of the oversegmented lines have vanished.

We realize that this choice was rather arbitrarily and that it holds no further significance, except that for this value it gives the best segmentation. In this way the implementation of the method is not optimal, and in the discussion some possible alternatives will be given. Perhaps this shows a more fundamental problem, which always applies to object recognition. In order to get a good segmentation one has to have prior information to get good results, this may be in the form of an object definition or rough location of the object sought after. This chicken and egg problem also applies here, where the prior is ill defined. However we regard this method as flexible enough that upon iteration eventually the optimal choice can be made.

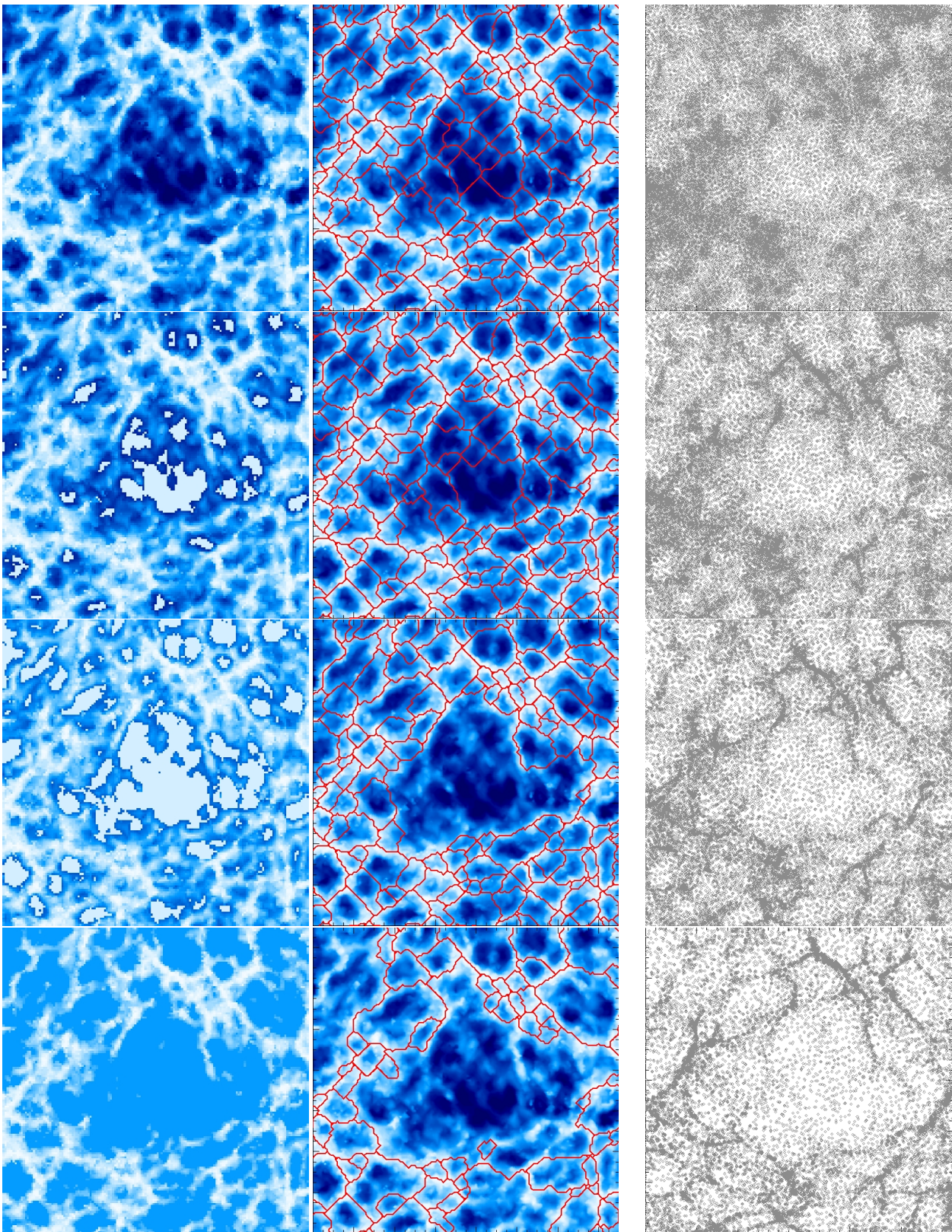


Figure 7.10: Plotted is the density field around the void present in lower left corner of the z -slice. The first column show this density field when no threshold was applied and then thresholded at a density of 0.22, 0.3 and 0.5. The middle column shows the resulting segmentations. This can be compared to the particles selected from $z=3$ plotted at four times steps.

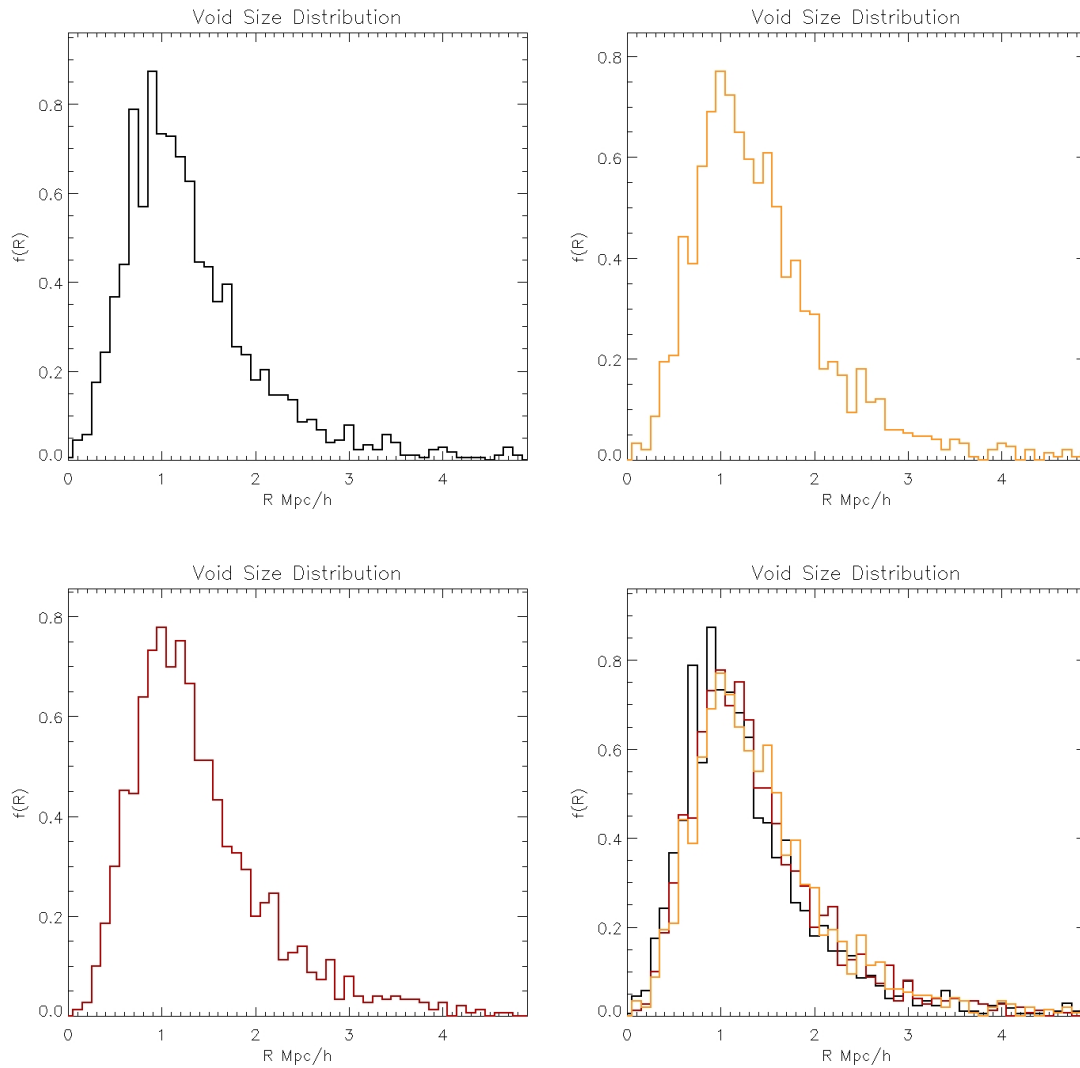


Figure 7.11: The void size distribution is plotted for all three different density fields and the combined one.

7.2.3 Watersheds and the Void Size Distribution

Now identifying each unique watershed area with a void, the void size distribution can be calculated. For each slice the segmentation was obtained in the manner as described above. Furthermore the method also finds the void surrounding, therefore only the underdense pixels are used for the voids. This prevents small voids from becoming artificially large as the fractional contribution of overdense regions is larger for these voids (see for example fig.(7.6)). For each watershed area the amount underdense pixels was counted. Since each pixel corresponds to a certain amount of surface, the area of a patch can then be calculated. Each region was then associated with a circle which has the same area. The radius of this circle was used to compute the void size distribution.

In figures 7.2.3 the void size distribution for each slice is shown. They show respectively the normalized void size distribution for x, y, z slice and the last shows all three distributions

combined in one plot. For the y- and the z-slice resp. 1504 and 1522 voids were identified, and in the higher resolution x slice 1794 voids were identified. This last high resolution slice was morphological smoothed with a disk of radius 2, so to treat all images on the same resolution scale. The void size distributions agree very well and all show a clear peaked distribution around a value of about 1.0 Mpc^{-1} . Comparing the shape of the distribution with the theoretical predicted shape, shows remarkable similarity. Eventually the goal is of course to compare both distributions. However we will not attempt to do this here and are mainly concerned with the physical properties of found voids and compare this with the theoretical expectations. At the same time this provides a check whether the void finder worked correctly.

The first question one might pose is whether all the watershed regions are fully formed voids. Firstly, we will look at the distribution of the minimum and the average underdensities of the voids. From the spherical tophat model one expects that mature voids have a minimum of about $\delta\rho$ 0.22. Above this value, voids are still in the linear phase, as they have not reached shell-crossing.

The distribution of the minimum value and of the average underdensity of the voids are shown in figures 7.2.3. The mean values of both distributions are respectively δ_{min} of 0.34 and δ_{ave} of 0.57. Although the mode of the minima distribution is at δ of 0.25, half of the distribution lies above 0.31. Obviously this does not agree with the spherical model. This could have either a physical origin, and thus has something to do with the evolution of the voids. Alternatively, it could also be due to projection effects by the slicing, and lastly it might also be due to artifacts produced by the watershed method.

Concerning, the latter is it possible that some of the minima in higher density areas are not associated with a void or with a fully grown void. In that case these patches might be voids that are still in formation and thus have a higher density and minimum. Alternatively these regions might be subvoids embedded within the more overdense parts of larger voids. Implying that they would not be taken away by the threshold at 0.3, or that part of the voids identified here are not voids yet. In this case, it might be arguable to further increase the threshold value. However as was also noted above, this might cause neighboring voids to percolate. Therefore further increasing the lower threshold is not a good option, because it may create artificially large voids. To analyze this an upper threshold will be applied and see what effect it has. A

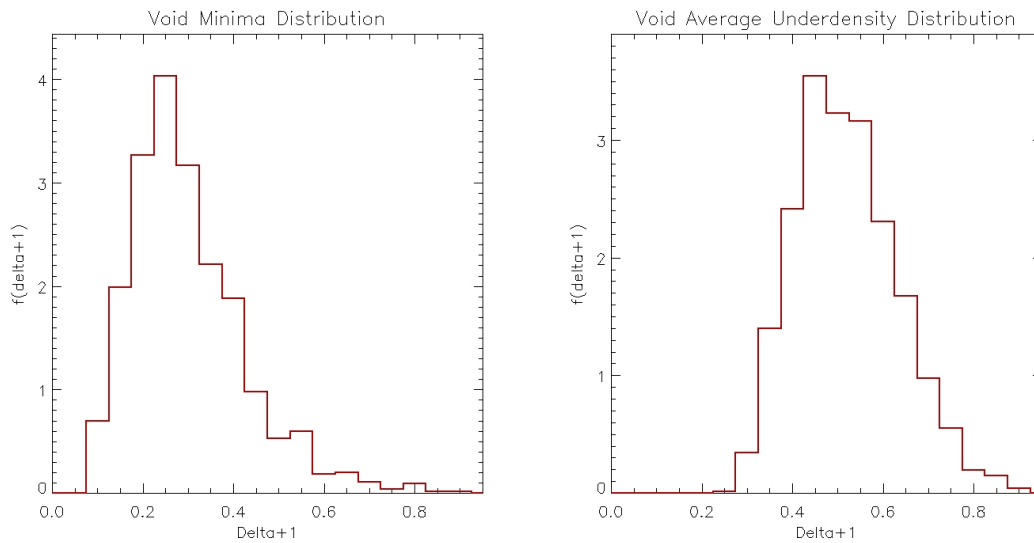


Figure 7.12: The left plot shows the distribution of minima of the voids. The right one shows the distribution of the average density of the underdense region of the voids.

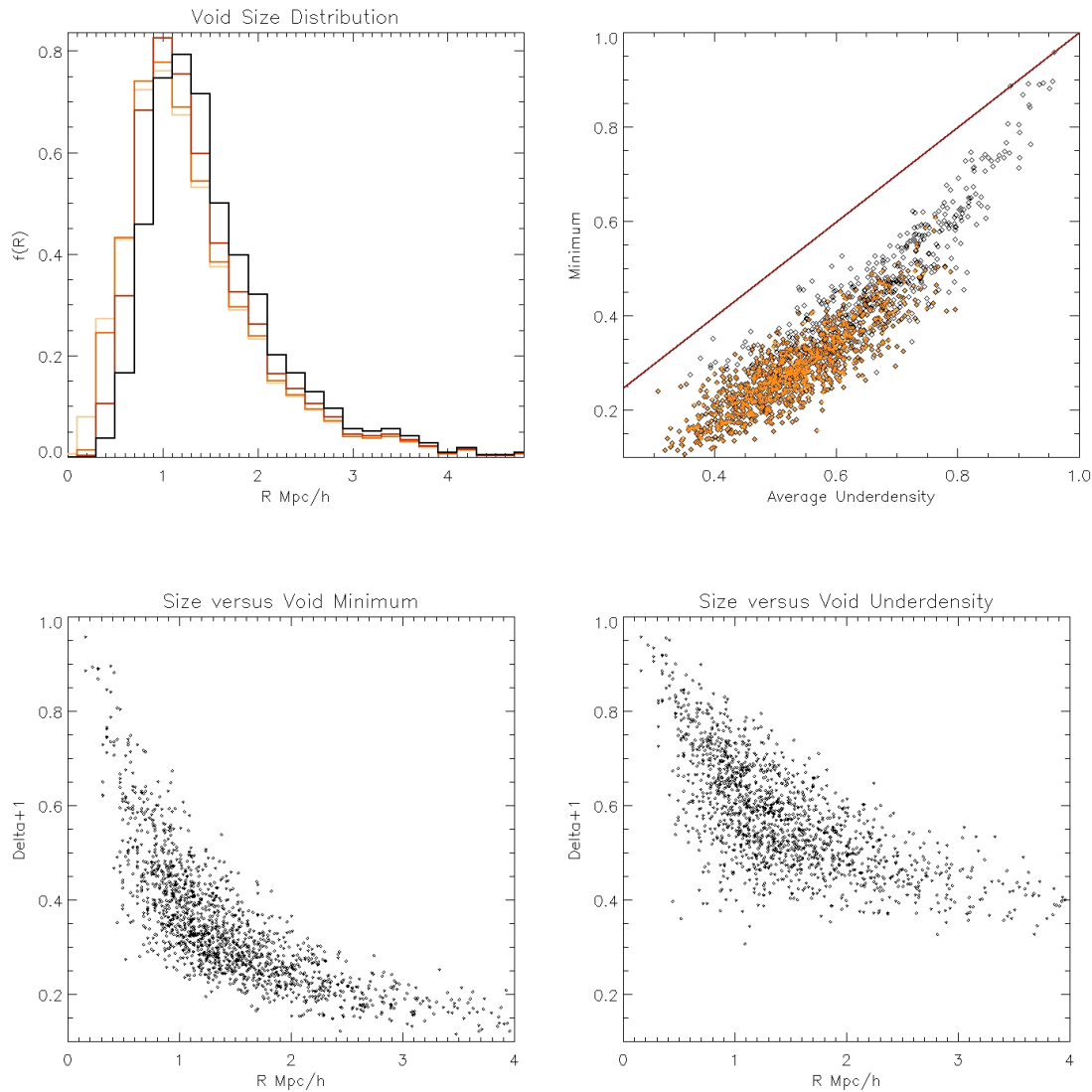


Figure 7.13: This figure shows the void size distributions when a consecutive upper thresholding is applied. Black indicates no upper threshold, red is 0.7, orange is 0.5 and yellow is 0.4. The upper right plot shows the minimum versus underdensity scatterplot, orange dots are voids larger than $1.0 h^{-1} \text{Mpc}$. The red line indicates a one to one correspondence, between both values. The lower images show respectively the scatter plots between size and minimum and size versus average underdensity.

repetitive lowering of this value from unity was applied, and if the void minimum was above this value a patch was removed. Figure 7.2.3 shows the effect this has on the void size distributions of the x-slice. Shown are the void size distribution for upper cutoffs at respectively 1.0, 0.7, 0.5 and 0.4. It shows that for a value of 0.7 the void size distribution changes only slightly and some of the smallest voids disappear. Further lowering this value, shows that more of the smaller voids begin to disappear. And only at a value of 0.4 the void size distribution seriously changes as

can be seen by the shift of the peak. This thus indicates that smaller voids are less underdense.

This can also be seen in middle plot. It shows a scatter plot of the void minima versus the void size as indicated by the black dots, also plotted is the value of the average underdensity, these are indicated by the red dots. It shows a clear and persistent trend of the voids to become less underdense as they get smaller.

This result is quite surprising from a hierarchical point of view. As the opposite trend was expected, i.e. that larger voids should be less underdense than the smaller voids. The reason for expectation is that in a hierarchical model the largest scales are the latest to appear and therefore have the least evolution. Just as supercluster are the largest overdense structures, and having the least overdensity. One would expect that the largest void are denser than the smaller voids as these are more evolved. We think that all three possible reasons as given above might be happening.

As already said above, a possible artifact of the method could be that smaller voids are still oversegmented. These could then be split up into smaller overdense patches. Which in turn could bias the smaller voids to be more overdense and have higher minima.

To study this in more detail the segmentation will be compared with the particle distribution. In that way it can be checked if all the voids selected from the density field are also present in the particle distribution. In the top side of figure 7.2.3 the particles in the lower left corner of the z-slice are plotted. These are selected out of a slice of $1.4 h^{-1}\text{Mpc}$ thick, centered around the density slice. These particles should approximately correspond to the density field (This is in contrast to grid based methods as TSC, because the particles that contribute to the field with the DTFE method can only be selected with the triangulation). On the left side, the segmentation is projected on top of the particles. Firstly note that the watershed very accurately follow the particle distribution. Showing that using a combination of the DTFE interpolation method and the watershed segmentation, the filaments and voids can be picked out of the particle distribution.

However, it also appears that a few of the watersheds are not so significant. As if one would be asked to indicate the voids in the left image, not all of the very smallest watersheds lines would be drawn. These oversegmented lines can be seen in figure 7.2.2 and correspond to small watersheds that preferentially lie perpendicular onto the isodensity contour levels. In the end these have to be removed, however this can not be done with increasing the threshold and or the amount of smoothing. Here this slight oversegmentation has to be taken as an artifact of the present method.

Another explanation might be that this trend is caused by the fact that we are considering only a slice. The slice-cut itself could bias the smaller voids to have on average higher minima. Namely the slice need not to pass through the minimal values of a void. And as the minimal value of smaller voids are smaller, this might occur more often for these voids. In this same way artificial voids created by the slicing can cause the minima of the void population as well.

To see how this influences us, the particles just below and above the segmentation are plotted in figure 7.2.3 with the segmentation overlain again. The largest structures, though sometimes a bit shifted, are present in all slices. The smallest structures are ofcourse less coherent and can disappear in overdense structures, or can also unite to form larger voids. Several of these cases can be readily identified by comparing the segmentation to the particles. This thus suggests that indeed some of the small voids are created by the slicing itself through the edge of a void. This is a well known phenomenon from stereology, i.e. that grain sizes in a two dimensional cut do not have the same size distribution as the three dimensional representatives.

These two effects, the slight oversegmentation and the slicing causes us to be biased to smaller void sizes. Thus we expect that the void size distribution as found in figure 7.2.3 has too many small voids. This does imply that the peak has to shift to higher radii in the three dimensional analysis. However this thus means that the peak size distribution was a robust finding, which clearly agrees with the theoretical model of SW04.

In principle this explains the fact that smaller voids have an higher average overdensity.

However it does not explain the fact that small minima seem to avoid small values. Because the method starts out at the minima, they can not be lost. Moreover the trend seems to be present even on the largest scales. Therefore we think that the this finding is not due to the watershed method nor to the slicing. As it is very unlikely that only due to the randomness of the cut no low minima of small voids are found.

Considering the inability of the previous arguments to explain the avoidance of small voids of having low minimal values. Could it have to do with the evolution of voids? This might be understood as follows; voids embedded in larger voids could evolve faster. As they could have extra growth by the underlying larger void, and thus become more underdense than a similar void in an average environment. This is in contrast with voids near overdense regions, these could grow slower due to fact that they are in overdense regions. Thus these voids are less evolved, implying that they are smaller and less underdense. Moreover these voids could be collapsing and in that case, these voids are shrinking. Consequently due to this contraction they may become less underdense as their volume diminishes. This could explain the trend, because smaller voids have a higher probability of collapsing, as was shown by SW04 and was also noted chapter 3.

To visualize the minimal values, we plot a mosaic image figure 7.2.3. In such an image each region gets the color by its minimum, and darker blue represents deeper minima. The white patches correspond to patches that are not overdense and these should be ignored. The mosaic image of the $z=3$ slice shows that the void depth is not distributed randomly through space. To see more clearly, the contours of the density field smoothed with a Gaussian of $5.0 h^{-1}\text{Mpc}$ are overlain. Also for comparison the particles are plotted in the left image. It seems that voids near overdense structure have minima that are far less deep.

In the bottom two plots of figure 7.2.3 we plotted resp. the minimum value of each watershed area in the smoothed density field versus that in the unsmoothed field and also the smoothed minimum versus void sizes. Although there is much scatter both show a trend that less underdense minima are preferentially locate near overdense structures and thus for small voids to lie near overdense structures.

These findings confirm our hypothesis that small voids are pushed away by the larger voids and pulled inward by the larger overdenser regions. This causes small voids located directly near overdense structures to collapse, in approximately the same fashion as described in the spherical model of chapter 3 and perhaps more like the collapsing voids in chapter 4. This will be checked in the following sections, where the evolution of the void population is followed by the particles positions.

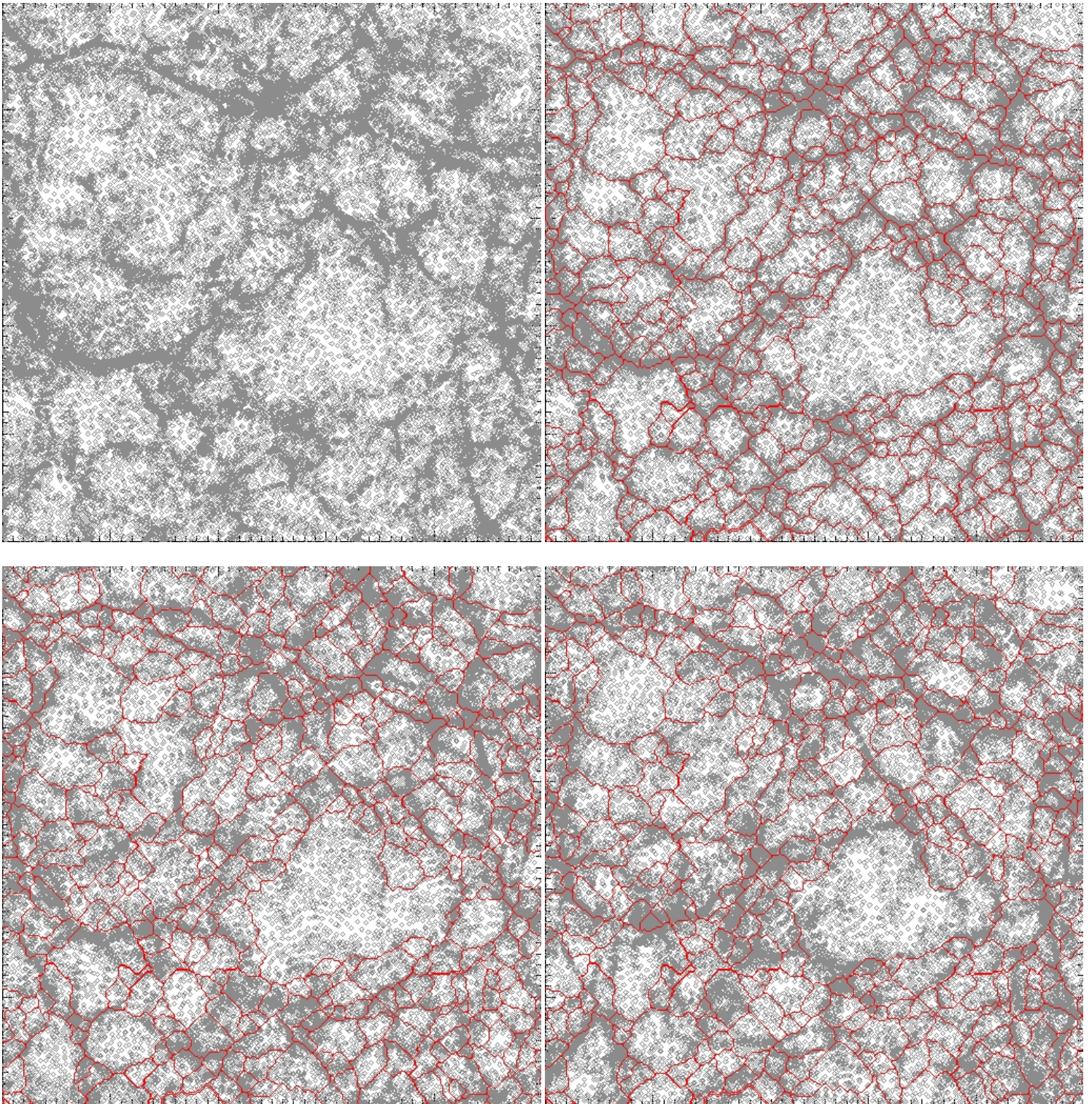


Figure 7.14: The figure shows consecutively the particles associated with the z density slice, the segmentation of this slice over plotted on the particles. And the two bottom pictures shows the same segmentation projected on two slices, one that is just below the z -slice and the right image shows the particles that lie just above it. All slices are of $1.4 h^{-1}\text{Mpc}$ thickness and are located in the lower left corner of the slice. The segmentation follows the filamentary particle distribution quite accurately. Also seen is that nearly all watersheds enclose a local dip in the particle distribution. The lower images give an impression of the three dimensional coherence in the segmentation and thus the limitations of a 2 dimensional analysis

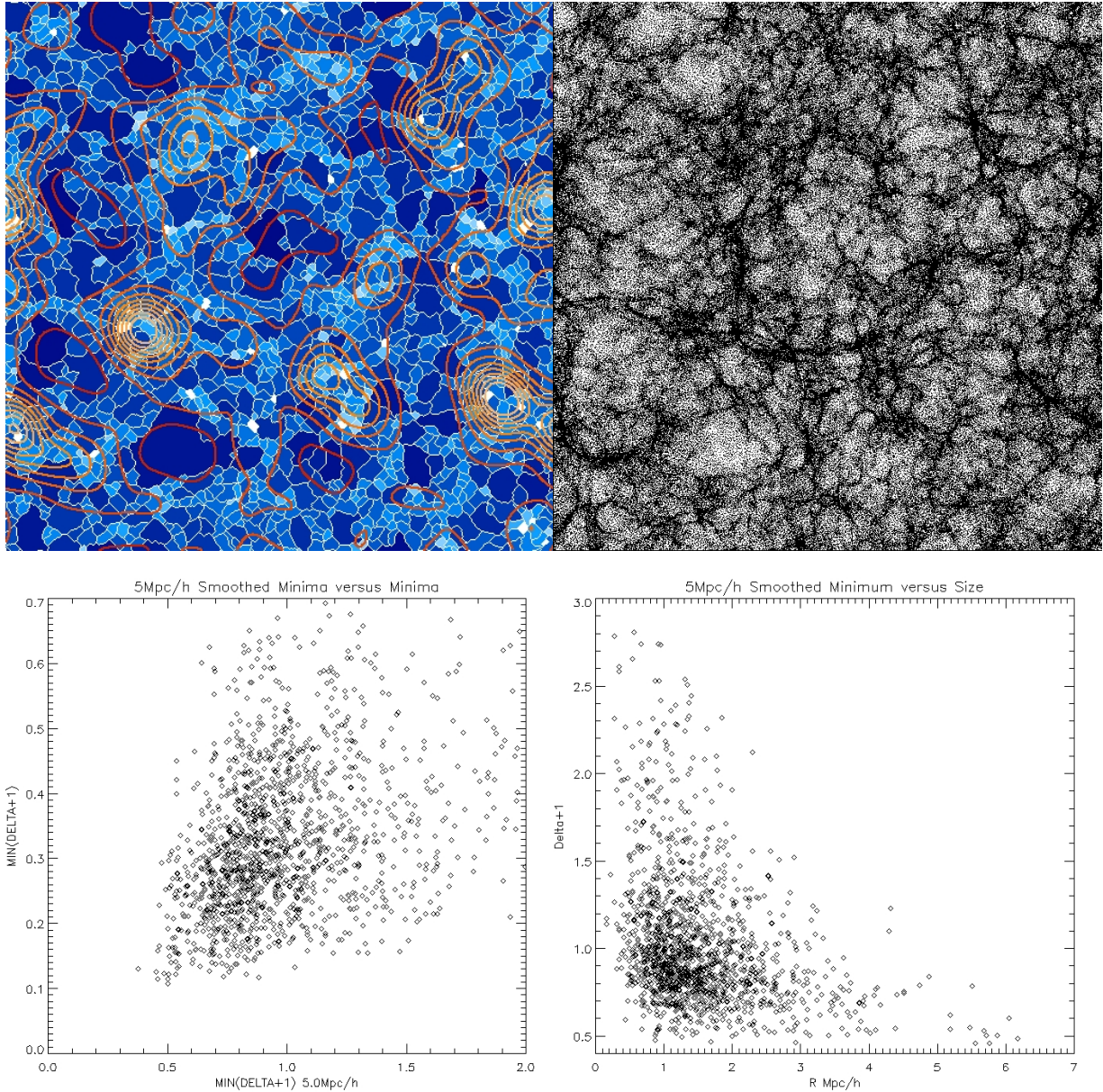


Figure 7.15: The mosaic images shows the spatial distribution of minima within the segmentation. For comparison the density contours from the $5.0 h^{-1}\text{Mpc}$ smoothed field are overlain. The ten contours are linearly distributed between $\delta\rho$ of 0.3 and 3.0. Also shown are the particles in a slice of centered around this density field. The lower row show two scatter plots of the minimum value in the smoothed density field versus that in the unsmoothed field, and versus void size.

7.3 Watersheds and Void Evolution

In subsection 7.2.2 it was shown that watersheds also detects the void hierarchy present in a void. And if an image was thresholded at ever increasing values this gives a kind of merging process. Furthermore at certain values the threshold will not only unite subvoids, but also the neighboring voids. This might suggest that continuing this process, a prediction about the void evolution can be made. In some sense thresholding can be regarded as mimicking the merging process of voids. Approximately like the process described by Dubinski et al.(1996), i.e. that voids merge when the boundary between two voids vanished. This process can be emulated, because by increasing the threshold the weaker boundaries will percolate first. Then applying the watershed transformation two neighboring voids are merged. Thus under the assumption that the present overdensity of the boundary is representative for the future voids merging, the void population at later times can be approximated.

Besides the threshold of 0.3, three higher thresholds will be studied, resp. 0.4, 0.5 and 0.6. For each of the corresponding segmentation the following is plotted; the mosaic image, the thresholded density, the skeleton and the particles of later time steps. These four plots are shown on the topside of the next four pages. The mosaic images are the same as described above, where darker colors correspond to deepest minima inside the void. On the right side the thresholded density field is plotted, and all pixels below the threshold are shown with the white color.

On the left side of the middle row the skeleton by watersheds is plotted. Each boundary is given a color by its average density value. That is the blue colors are all the overdense boundaries, and the yellow and red are underdense. The darker blue the more overdense and the redder the less underdense, see also the color-bar shown in the margin. These values were calculated by constructing the adjacency graph as described in section 5.5.2. For each two adjacent voids the average density over the boundary was calculated. This yields for each threshold a different skeleton. Comparing the skeletons indeed shows that the lowest boundaries have been removed. Aside of the skeleton the particles out of the $z=3$ slice are plotted for the following four time steps $z=3, 1, 0.42$ and 0 . These particles were followed in the same manner as in figure 7.2.3, only now the whole slice is plotted. As previously, note that this primary shows where the particles out of the density slice at $z=3$ end up. Thus it can at some places be well extended in the z -direction, and therefore it can not readily compared with for example the slices of figure 7 (Though the general agreement between the largest structures is apparent). As the slices in figure 7 are at fixed location, this implies that each slice contains different particles. While the particles plotted here are always the same, but possibly at very different z -coordinates. By comparing the particles at different time steps and the mosaics of different thresholds, we looked if there was global agreement between the voids in the particle distribution and the voids in the mosaic and skeleton images. The time steps with the most agreement were plotted to compare with the void evolution.

In this section we will only consider these four following plots; the mosaic, density, skeleton and particles. The bottom two images will be treated in the next section. A quick comparison shows that at the largest scales there is remarkable good agreement between the voids and filaments in the mosaic and the particles. There is though less agreement when one looks at all the small voids present around the filaments. These are still present in the last two segmentations, but are not present in the particle distribution. These small voids will be treated in the next section. First the evolution of the largest voids as present in the final slice will be studied.

The voids in the four mosaic images show the same kind of merging process, as described in section 7.2.2. For example the void discussed in that section can be readily seen in the four figures. Its position is indicated with the letter A in the skeleton of the threshold 0.6. This void only mildly evolves, by merging outward with a few smaller neighboring voids on its edge. As can be seen in the thresholded mosaic images of 0.4 and 0.5. The particle evolution shows a



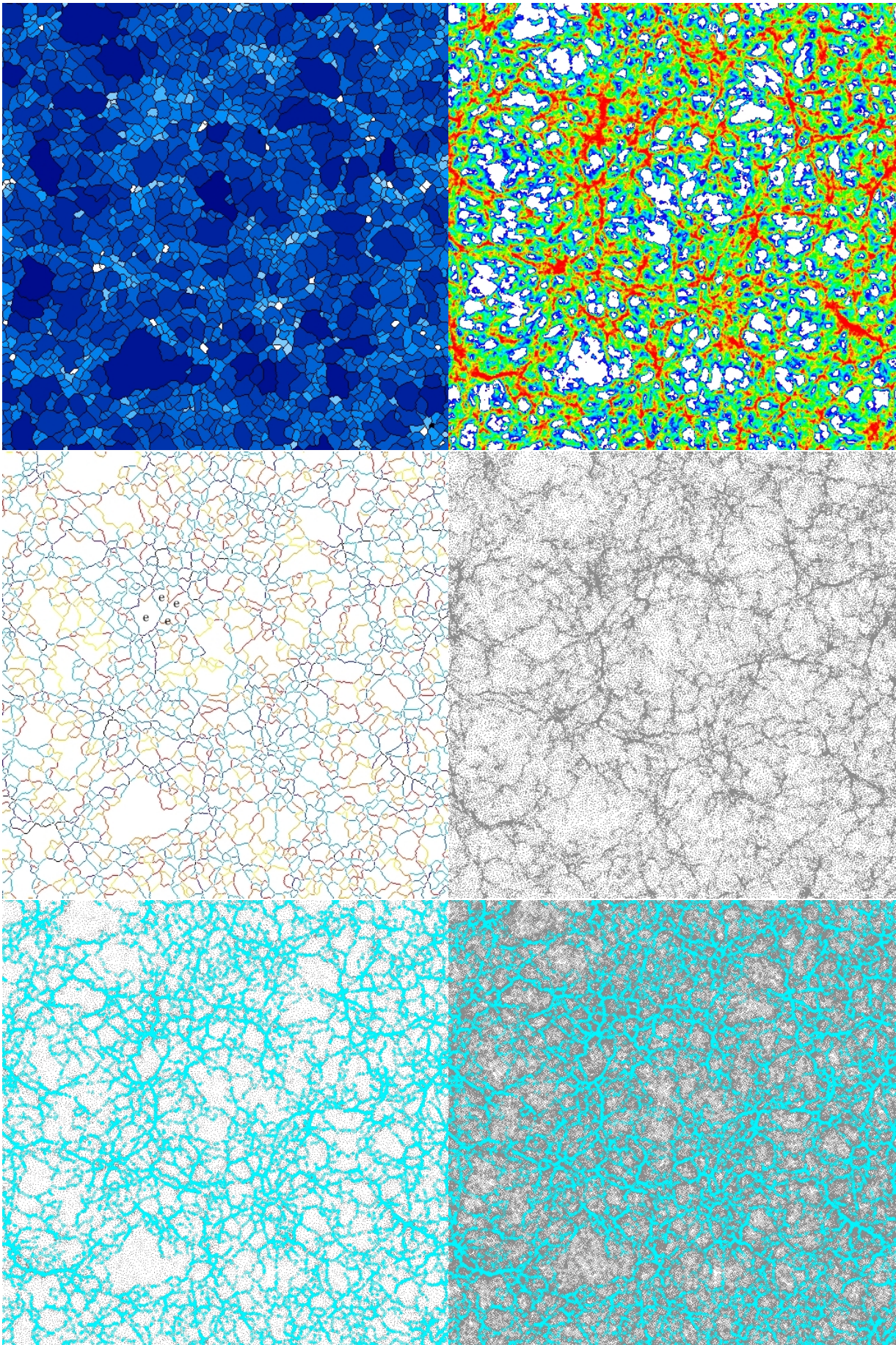
similar behavior, and it does not undergo any significant merging between $z=3$ and $z=0$. They also show that void A merely expands into its surrounding. Theoretically this would correspond to a void that approximately goes non-linear at redshift 3. Thereafter it evolves self-similar, meaning that the void has a power law like expansion and it is just rescales in time. This ties in with the fact that it had much substructure and subvoids found in section 7.2.2, and as seen in figure 7.10.

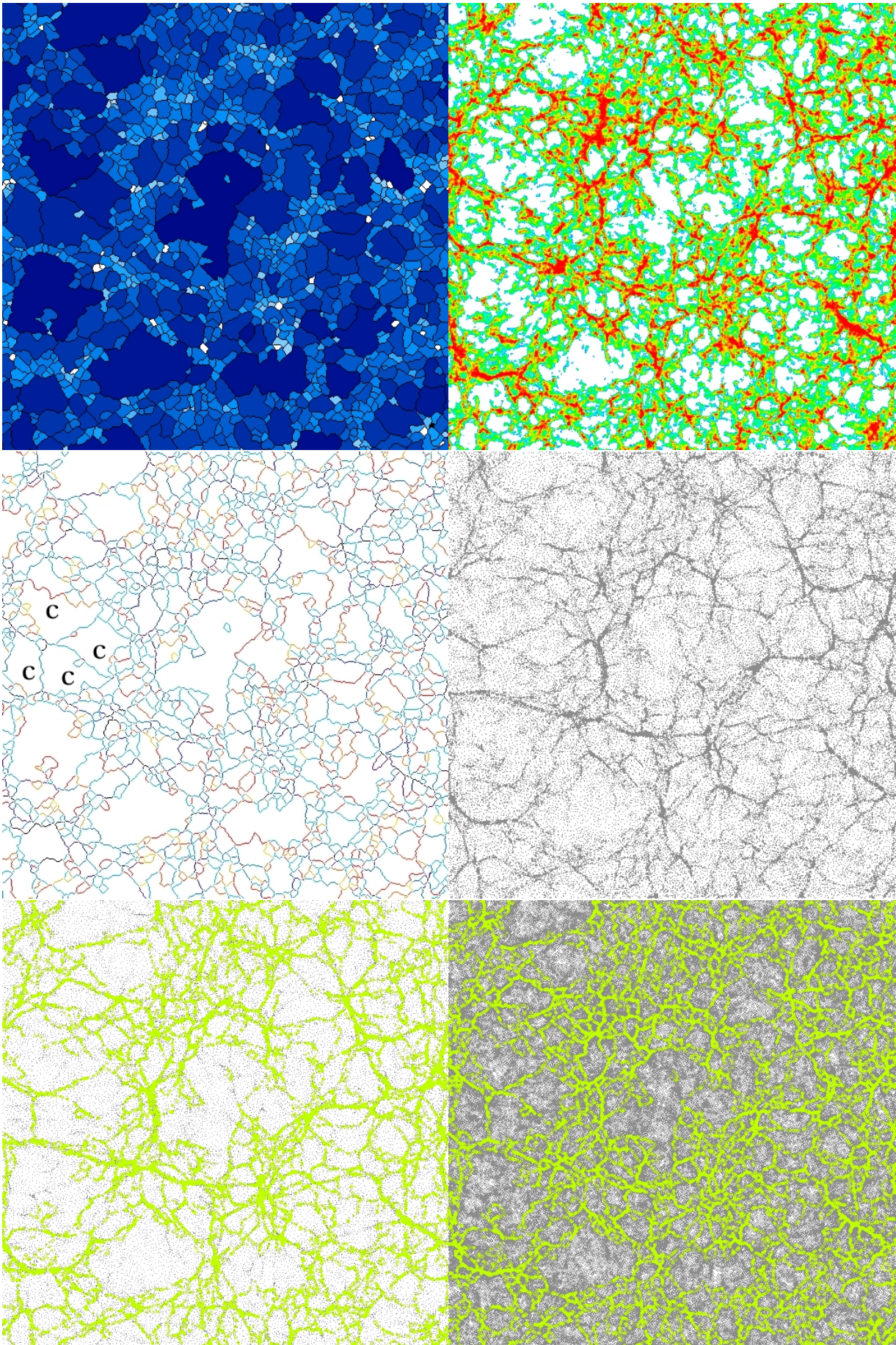
Approximately the same can be seen for void B, as it expands into its surrounding, it merges with few boundary voids. Though for void B, it is less visible when the two largest subvoids, resp, B1 and B2 (indicated in 0.5-skeleton), can be considered as one large void. Mainly, because the dividing boundary is still very much present at $z=0$. However as shown in the last image of figure 7, the outer boundary of void B indicates that it is one large void. The best way to check this would be with the density field at $a=1$. And study the strength/overdensity of filament/wall B1|B2.

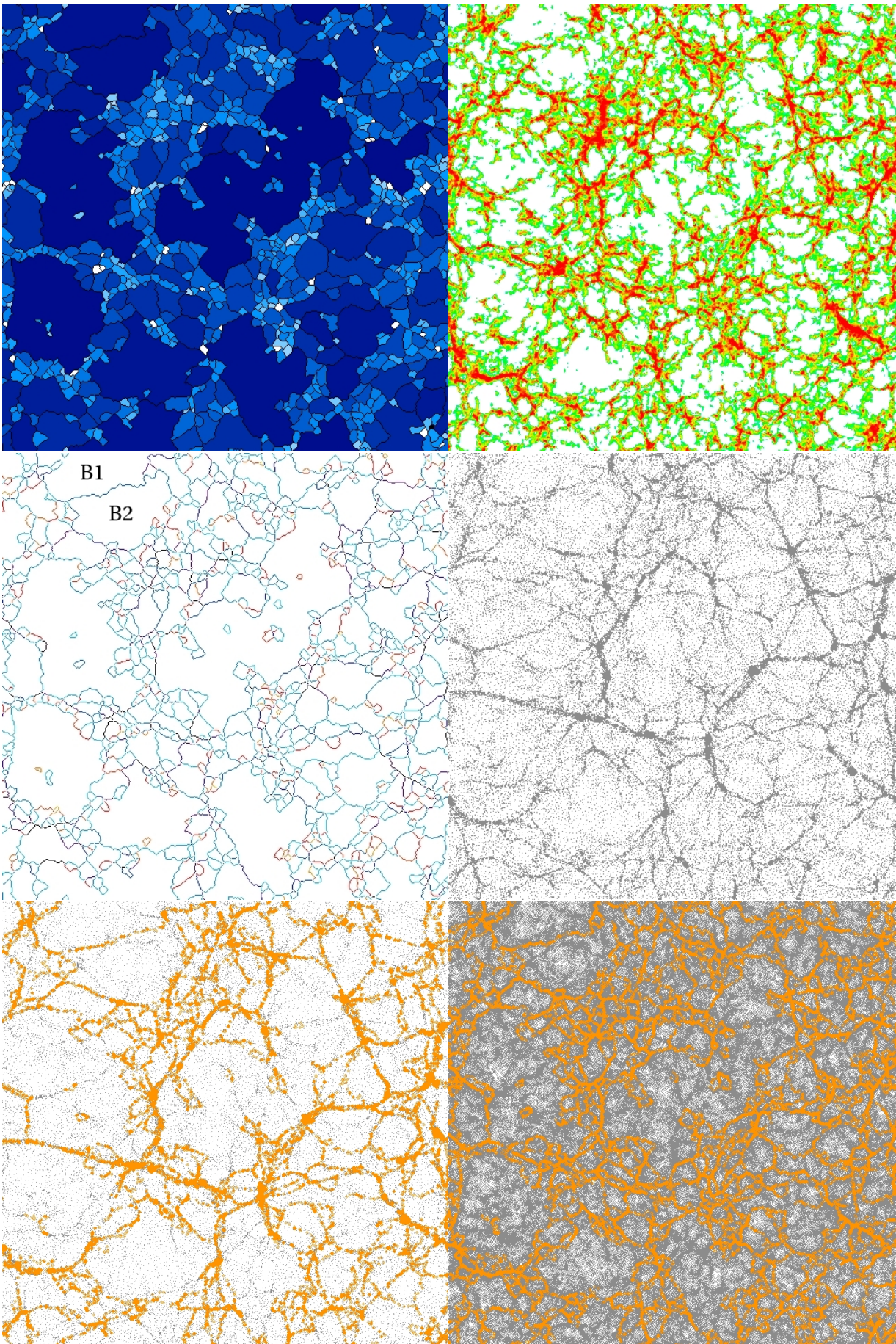
At the highest threshold, 0.6, void A percolates at its underside, into the upper right void B. Again this is checked with the final particle distribution, as also shown on this page. Clearly this does not happen, instead a boundary of smaller voids are present in between these two voids. These finally collapse into a boundary as can be seen in the particles at $z=0$. This is the limitation of the present analysis; unaware of collapsing regions after $z=3$. This causes a fiducial merging of these two voids, while actually a dividing filament formed. The same can be said for void D, which spuriously percolated into another void into in the upper right corner.

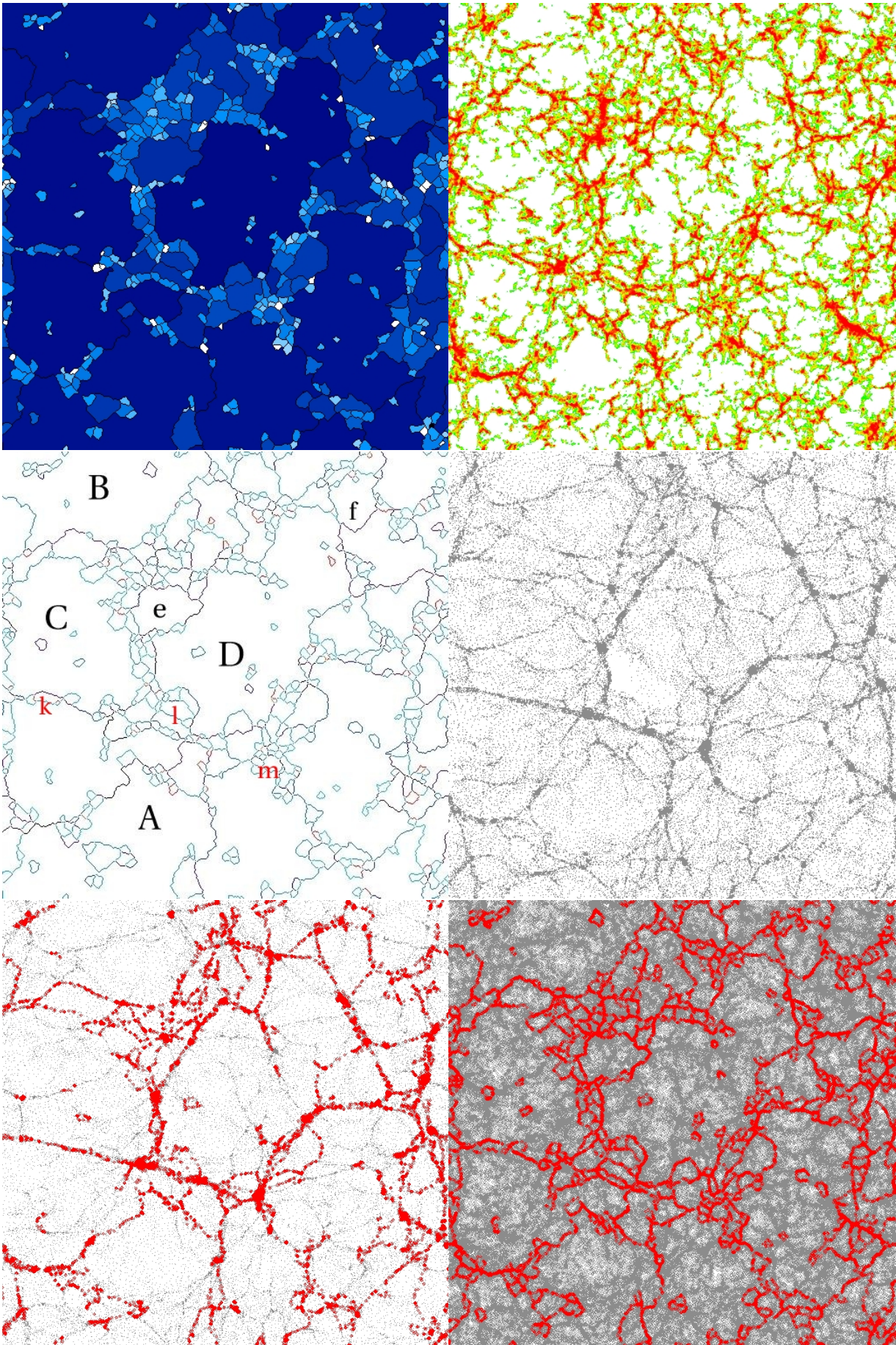
The mild merging evolution of void A and B differs from other large voids identifiable at $z=0$. Take for example the void indicated with the letter C. It has merged from numerous voids out of the $z=3$ slice. These $z=3$ voids first merge into four larger voids, as shown in the 0.4-skeleton. They are indicated with the letters c. Subsequently these merge to form the larger void C. The same hierarchical merging pattern can be seen in the particles. This build up can also be seen for void D. Again various smaller voids have merged to form D. These smaller voids that formed these larger voids, still remain as substructure inside the void, and expand along with its motion.

Next, we will focus on two smaller void, resp. indicated with the letters e and f in the 0.6-skeleton. Here a clear dichotomy occurs, while both are approximately of the same size, the corresponding particles show a very different behavior. As f can be readily identified in the particles at $z=0$, at the position of e no void can be identified. Nor is there a subvoid in C or D that can be associated with e. This would suggest that the smaller voids, which e encompasses, ended up in between the two overdense structures surrounding e. This can be confirmed if one looks at the particles in the different time steps. Tracing the particles that make up e in $z=3$, shows that most subvoids that made up e have collapsed into the two large structures around e. Clearly these subvoids are an example of collapsing voids. Furthermore this thus would suggest that many of the small voids still present at the highest thresholds, but with out a particle counterpart, are actually collapsing voids. In agreement with the fact that they all lie near the largest overdense structures, such as clusters and filaments in particle distribution.









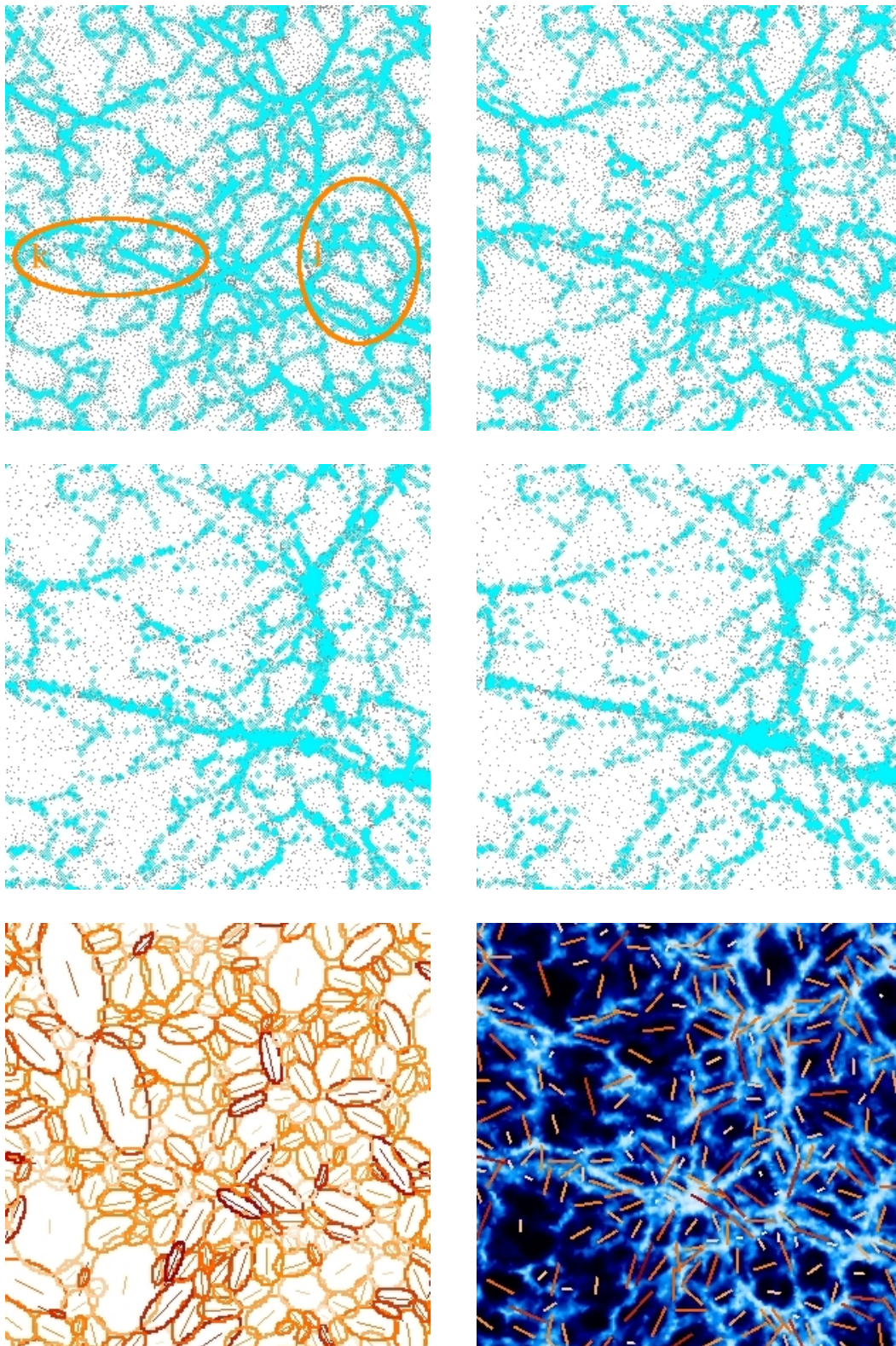


Figure 7.16: The evolution of both the collapsing regions k and l are shown. The selected particles of threshold 0.3 are plotted in cyan on top of the Lagrangian slice particles. This was done for resp. four redshifts; namely $z=3, 1.5, 0.42$ and 0 . Also plotted in the lower two images are the orientations of the voids. The left bottom image shows the fitted ellipses. The bars indicate the axis orientation of the major axis and the length of the bars indicates the ratio of the major and minor axis. The redder colors indicate a larger major-minor ratio. The right one show the bars projected on top of the density field at $z=3$.

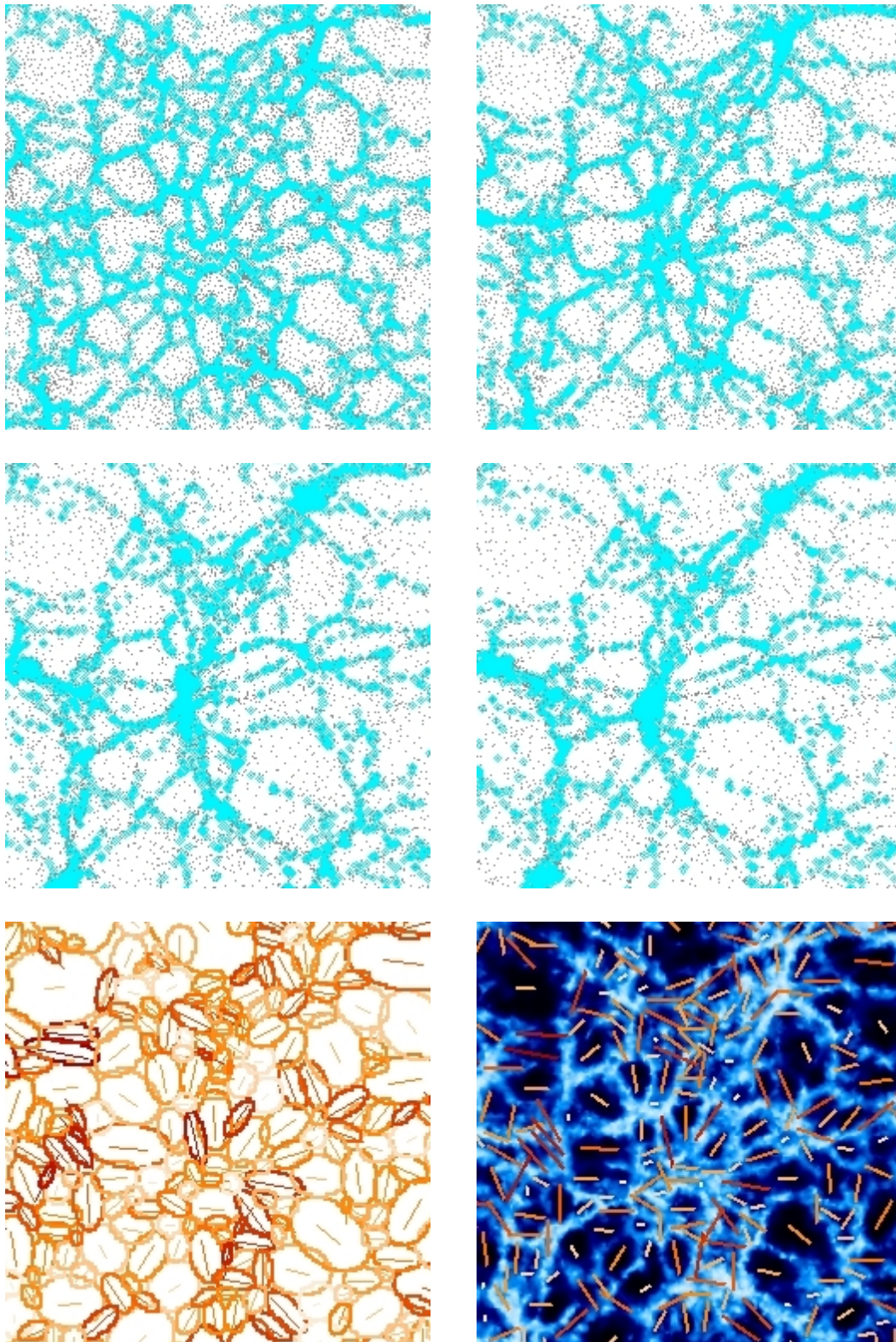


Figure 7.17: As in figure 7.3, only now for collapsing region m .

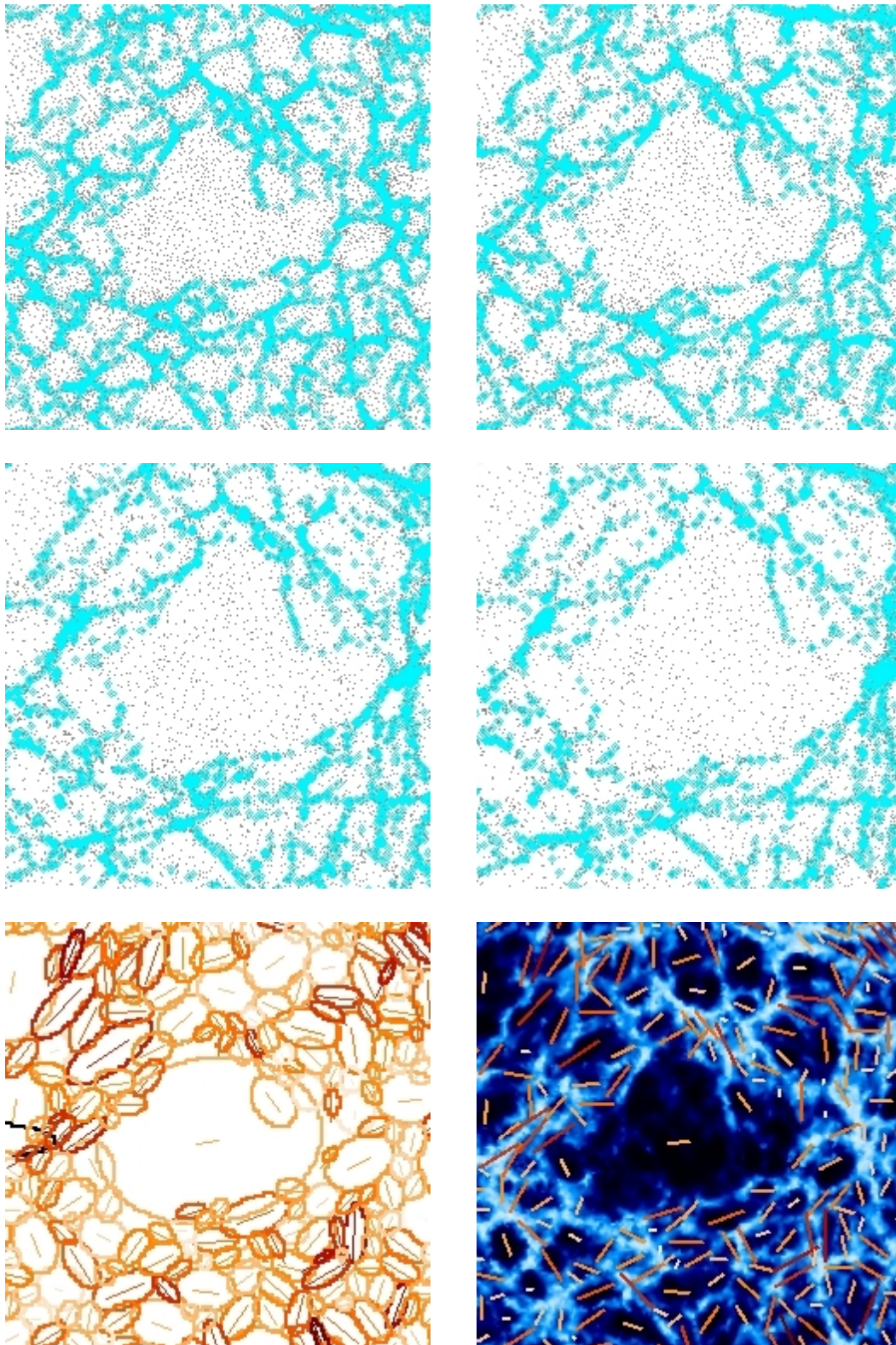


Figure 7.18: As in figure 7.3, only now for the void A.

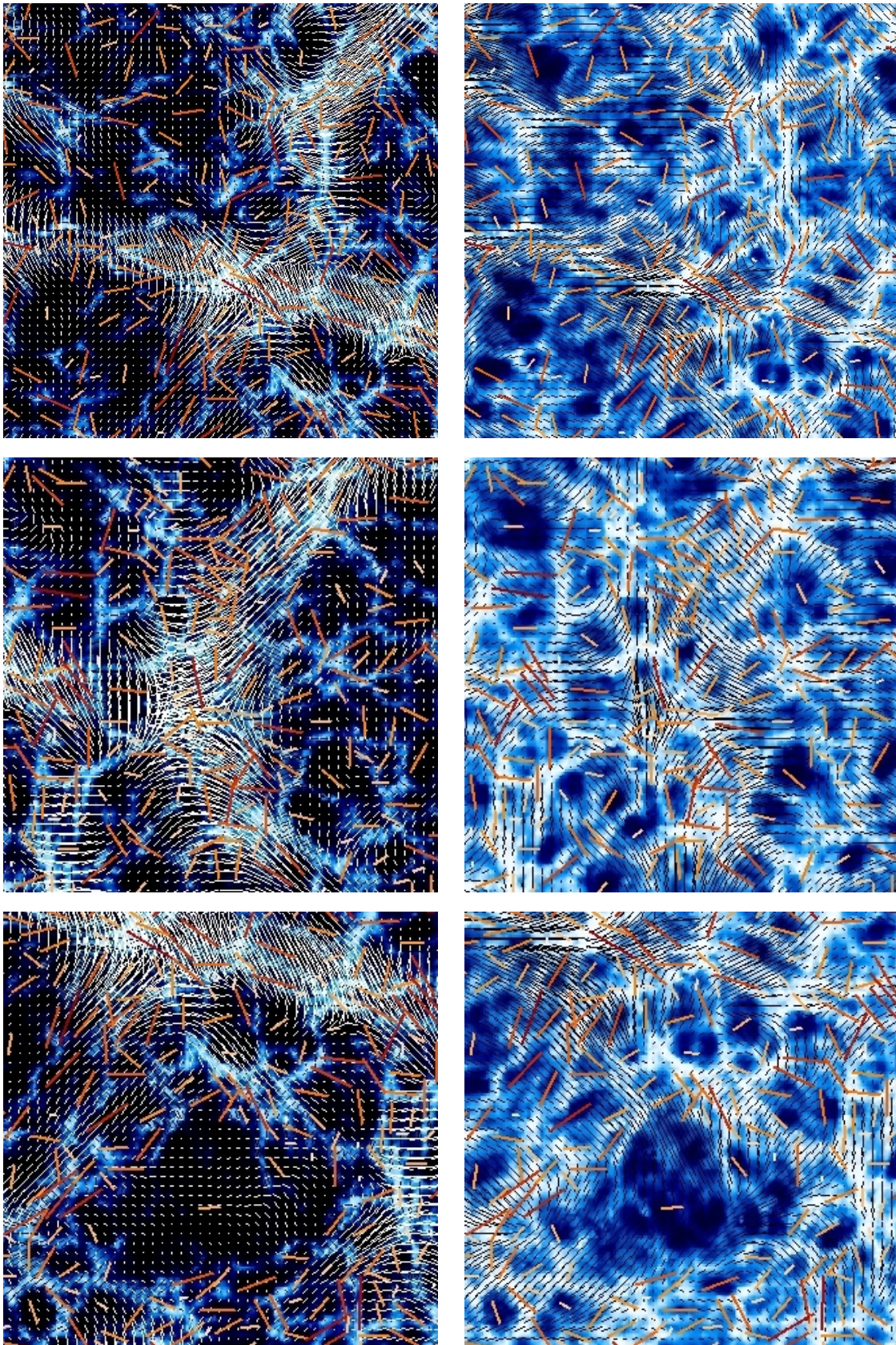


Figure 7.19: The figures show resp. the regions k and l, region m and void A. The density field at low and high gamma contrast is plotted. On top of these images the eigenvectors of the velocity shear component is plotted, indicated by the small white and black bars. Also the orientation of void shapes is plotted with the orange bars.

7.3.1 Lagrangian Evolution of the Watershed Selected Particles

In the previous section the void hierarchical build up of large voids was discussed by comparing thresholded segmentations with the Lagrangian evolution of the particles. All the segmentations were done on the density field at a redshift of 3. Since this field is representative of the particle intensity at that redshift and at that position of the slice. The evolution can also be traced by selecting certain particles from the segmentation. Here the evolution of the voids will be traced by selecting particles, which belong to the boundaries of the segmentation. Another possible choice is to follow the particles in the voids, but this will not be done here. The particles associated with the field were extracted with a thin slice centered around the field position at $z=3$. Subsequently, the boundary particles were selected by overlaying the interpolation grid on top of the particles. And for every boundary pixel, all the particles that are inside this slice-pixel cube, were tagged as a boundary particle.

This was done for the segmentations as discussed above (thus for a threshold of 0.3, 0.4, 0.5, and 0.6), the results are plotted in the lower right corners of the previous four series of image sets. The left image shows the position of the particles at the corresponding timesteps, while the right image shows the selected particles at $z=3$. The redshifts were swapped to be able to compare with the skeleton and particle distribution plotted above in the middle row.

The selected particles for a threshold of 0.3 are not that interesting, and merely shows twice the same cosmic foam. The difference between both of these is that for the right hand side a larger symbol was chosen for the particles, so to better show the substructure inside the voids. For $\delta\rho$ 0.4, 0.5 and 0.6 the selected particles at $z=3$ are plotted at the lower right corner, and it shows the void build up as discussed above. The left hand side shows the selected particles at the same redshifts as above (1.0, 0.42 and 0).

Comparing the first two time steps with the slice-particles at $z=1$ and $z=0.42$, reveals that indeed the selection at $z=3$ resulted in the presence of the prominent filaments. In the last threshold only the most prominent are completely incorporated in the selection. Some of the weaker filaments are missed, causing the gaps as already discussed above. Further comparison shows that the skeleton looks like the selected Lagrangian particles and vice versa the particles look like the selected particles at $z=3$. This is thus a direct confirmation of the above approach.

For the highest two thresholds most evolution is visible. By comparing the $z=3$ selected particles with their position at $z=0.42$ and $z=0$ shows that indeed many of the small voids present at $z=3$ have disappeared, or are collapsing. Thus concluding that at least a part of the collapsing voids are located near overdense regions such as clusters and filaments. This strengthens explanation of the collapsing void proposed in section 7.2.3.

Various interesting regions of void collapse regions can be identified. Take for example the region indicated with the red letter k in the 0.6-skeleton. The filament is surrounded by two large voids, suggesting that the outward push of both voids induced the formation of this filament. This can be seen more clearly in the zoomed time-sequence ($z=10,3,1.5$ and 0.0) of figure 7.3. In the collapse of the filament several of the smaller voids are taken with it as well. The collapsing region, as indicated by the letter l, suggests that both the push of void D and the pull of the cluster caused the infall of approximately four ellipsoidal voids. Various smaller voids surrounding the cluster at $z=3$ did also collapse into the cluster as well into the filament.

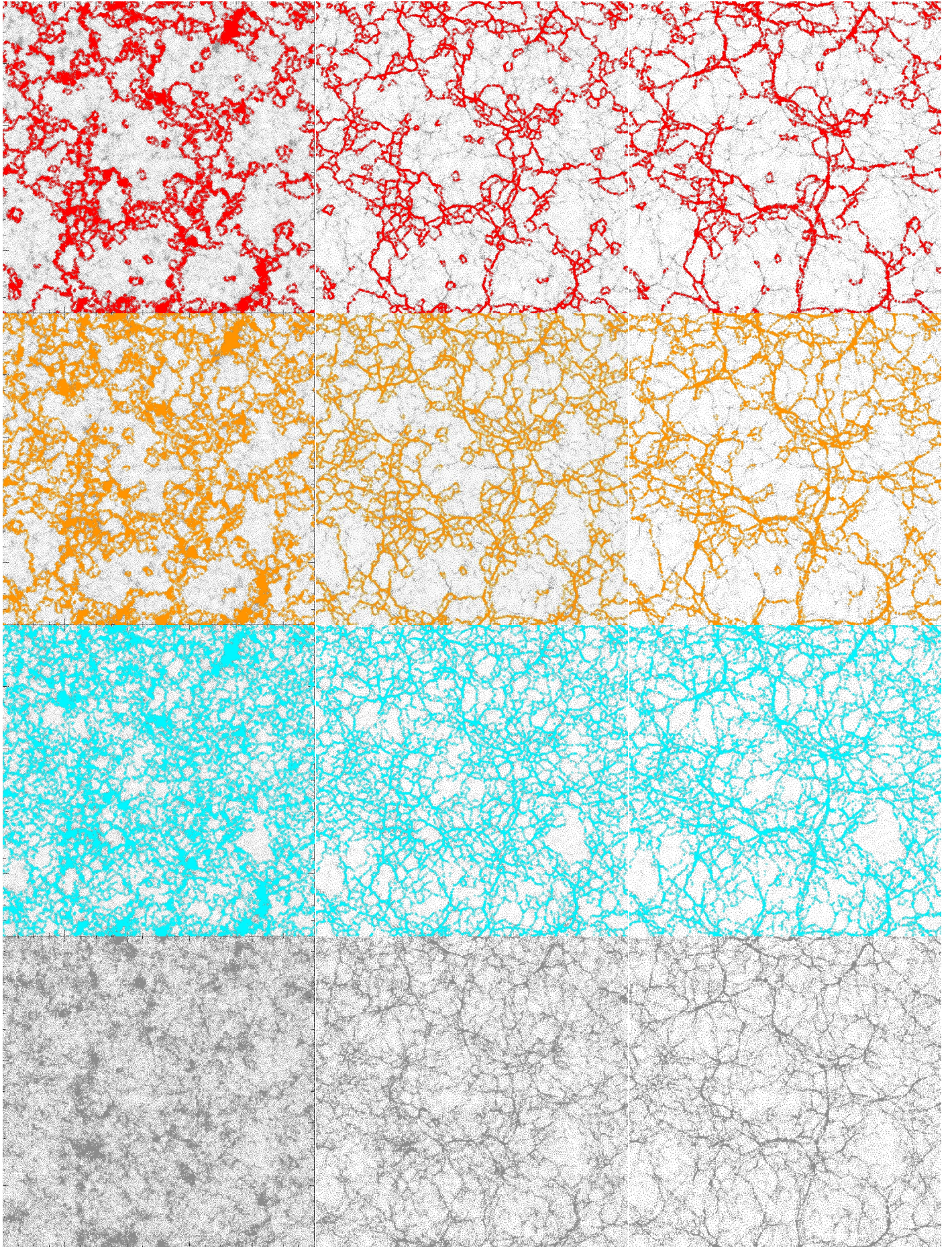
A similar behavior can be seen in region m, again a large overdense region forms, taking with it many of the small voids, see figure 7.3. Giving the cluster the appearance of a large sink of small voids. Moreover, all of the surrounding voids are at the same time pulled toward the cluster and the filament, while at the same time being pushed away by void D, as also seen in region l. This can be especially well seen in the orientation of the voids and the evolution of this orientation. The impact of the cluster can be seen in the stretching of the voids toward it, while voids that lie closer to void D are compressed in the radial direction and aligned in the direction of the filaments. The same behavior can also be seen in region k and l.

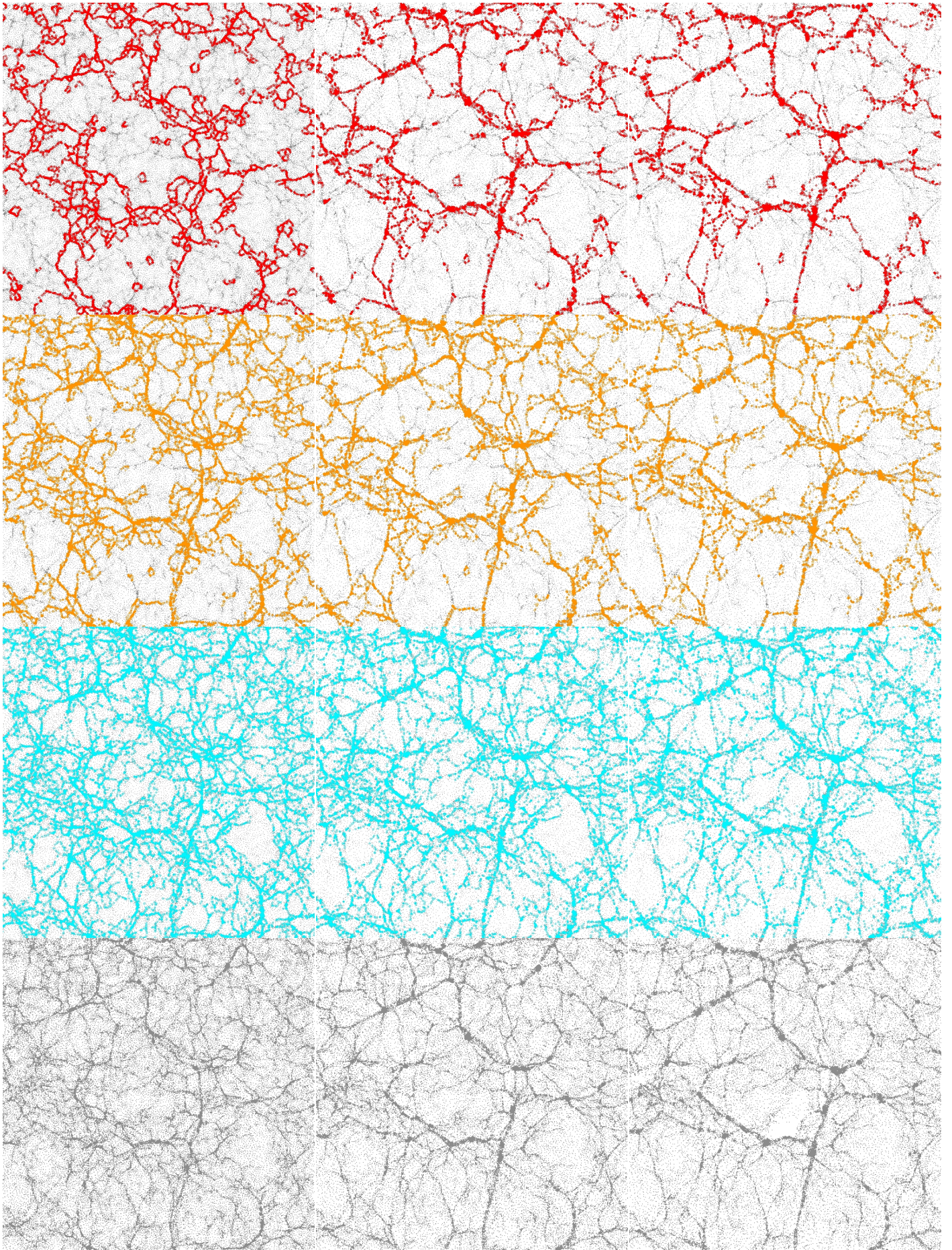
To show this preferred orientation more clearly in the bottom images the of figures 7.3, 7.3

and 7.3 the orientation of the voids is plotted. This was computed by fitting ellipses on the shape of the watershed regions, then the bars indicate the ratio between the major and minor axis. The color and length indicate the relative strength of the ellipticity. The orientation seems to occur in two different ways. Near the cluster the voids point preferentially toward it, as seen in the central clusters 7.3 and 7.3. Inside and near the filaments the voids have a tendency to align themselves along the direction of this filament as seen in region k and l. This is also shown in the evolution of the particles. Similarly, in figure 7.3, the smaller voids around void A preferentially align themselves in the direction of this voids boundary. The evolution of the particles show that these voids collapse in the same mode as described in chapter 4. The push of large voids cause the disappearance of smaller voids in its surrounding.

This is thus in contrast to the model of SW04, as these considered only the spherical collapse of the voids. Probably, this is still a good estimate in the central regions of the collapsing clusters. However the push of the large voids also matters as was shown in the previous collapsing regions. This is most strongly around the void itself, and as can be seen by the strong orientations of the small voids in the upper right corner in figure 7.3 and the upper right corner of figure 7.3 and most strongly in 7.3. Moreover voids also collapse into filaments as shown in region k and l, and in the filament of figure 7.3. Furthermore figure ?? for the zoomed images the velocity shear components are indicated. As in the linear regime the tidal field and the shear component of the velocity field are directly related. The figure shows that indeed the direction and magnitude play an important role in the collapse of the small scale voids.

The general void collapse in the selected particles can be followed more clearly in the set of images on the next two pages. It shows the Lagrangian evolved particles for various time steps ($z=10, 3, 1.5$ and $1.5, 0.42, 0.0$) and for different thresholds. The first column is without threshold, the next three columns are for resp. a threshold of 0.3, 0.5 and 0.6. Especially if one looks for collapsing regions in the threshold 0.6 images, and then follow this very same region in the other two thresholds many of the collapsing voids can be identified. Their evolution is similar as described above, pushed away by the voids and pulled inward by the clusters and the filaments. We thus conclude that anisotropic collapse due to the external tidal field plays a major role in the collapse of the small scale voids.





Chapter 8

Conclusion

Here we presented an analysis of the void population and its evolution. The simulations of the constrained voids in the powerlaw density fields showed that large voids have a big impact on their neighborhood. The expansion of the large voids in its surroundings, cause the smaller voids to be pushed away. Eventually this push induces the small voids to be sheared and teared away into the boundary of the void. This was shown with an example of such a collapsing void from one of these voids. The Λ CDM GIF simulations confirmed our finding.

In order to trace the void population we developed a new voidfinder, based on the watershed transform. This has the benefit that it places the boundary of the voids on the natural encompassing high density filaments. This makes the method sensitive to the outer boundary of the voids, which is vital for understanding the evolution of the void merging. Furthermore, it thus found also the filaments of the density field. And in this way the method can be regarded as a true foam-extractor, which is able to find as well the voids as the filaments at the same time.

The two dimensional method was tested on the kinematic voronoi model. This model maximizes the noise in the voids, due to the lack of substructure and interpolation method. It was shown that with a combination of thresholding and smoothing this could be suppressed enough to retrieve the underlying voronoi model.

The void population of the DTFE-density slices out of the GIF simulations were studied with the new watershed method. It was shown that indeed the watershed method is able to extract the cosmic skeleton. The void size distribution yielded indeed a peaked size distribution, as was predicted by the theoretical model of SW04. This peak is significant, since we are probably biased toward smaller scales, indicating that the peak can shift to larger scales, but not vanish.

The internal density distribution of the voids were also studied and showed a surprising relation that smaller voids are less underdense and have higher minima. This could only partly be explained by artifacts of the method and the effect of slicing. However the explanation presented by the void collapse model does also influence this finding. As the theory shows that smaller voids are more prone to collapse than larger voids. Hence one might expect that as the smaller voids turn around, the internal density increases or decreases less than expected from the isolated spherical model. The same reasoning of course applies to the minimum of the void. We attempted to show a correlation between the denser voids with their local neighborhood via the smoothed density field. This yielded that these voids indeed prefer high density regions, however the relations show much scatter. Which can be due to the smoothing, as it possibly erases much of the filamentary structures.

A good way to study the evolution of the voids is by increasing the threshold of the density field, and applying the segmentation. It was shown that this can approximately predict the resulting filaments and voids that make up the final particle distribution. This can be understood with the void merging process. As weaker boundaries are eaten away by the threshold, two catchment basins will merge in the segmentation and the corresponding voids will also merge.

Furthermore, in the segmentation with the highest possible threshold showed that many voids near overdense region remained. These obviously did not merge in the segmentation with the larger voids. By selecting these particles in the slice and tracing the Lagrangian evolution of the particles. The evolution of these voids was studied and it showed that almost all of these voids would have collapsed or were collapsing in the final slice. This strengthened our result on the unexpected values of the minima and underdensities of small scale voids.

The evolution of the smaller voids, triggered us to propose the following model of void collapse. The smaller voids will be seriously affected by the linear bulk flow and the velocity shear induced by the large scale voids and clusters. The small voids in regions located near overdensities will be primarily pulled into these structures. Equivalent to the collapse mode that is described by SW04. However also the voids and the anisotropic collapse of filaments have an impact on the small void population, resp. by their outward push and shear. This was seen by the various voids that are torn away into filaments and pushed away by the voids. Together this underdense push and overdense pull are responsible for the distortion and collapse of small voids, the *push-and-pull* model.

Chapter 9

Discussion and Future Prospects

Tools from mathematical morphology are often used to characterize the geometric properties of structures. Therefore it has been applied in geology, medicine and solid state physics to quantify the structural properties of the involved images. Various of these could also be useful for the cosmic web analysis. For example, a granulometry, this is a sequence of increasing sized morphological operators, that yields a morphological size spectrum. As was already indicated here, the length of the skeleton by watersheds in an excursion set, could hold some information about the filaments in the field. Also the skeleton can be analyzed by looking at the shape of it, i.e. like nodes distance, connectivity etc.

A novel 2D void finding method was introduced, that is able to find the voids and the filaments. It was shown that with smoothing and thresholding most of the oversegmentation can be removed. However still there seemed to be a population of small voids that result from oversegmentation. As discussed a 3D method could already give improvement. Because connected underdense regions were split up by the 2D slicing. It has been shown that the watershed method can be extended to 3 dimensional fields as the principle of the method is valid for the n-dimensional case.

Still in three dimensions one suffers from the fact that perhaps a void need not to have one minimum associated with it. This can thus either be to noise or subvoids. The major component of the noise can be taken out with a 3D smoothing. And most of the subvoids in large voids can be removed with thresholding. Though in the 2D case there were instances of smaller overdenser voids, that were still split up. Probably because the threshold could not unite these regions. Note that this was not an issue for the smallest voids as these all have one uniquely defined minimum. There are several possibilities to overcome this problem. These are inspired on the solutions presented in chapter 5.

First the flooding sources could be selected more carefully by imposing conditions on the minima, i.e. a marker based solution. These could for example be; a minimum amount of pixels that define the a minimum, a maximum and minimum value of the minima pixels. These are almost equivalent to smoothing and thresholding, but only apply on the minima of the image and not on the whole image. Furthermore, one could use voids of the fitting-ellipse method of Colberg in prep. as the initial flooding markers. One might also think of first doing a multiscale decomposition of the density field and then select according to some criterion the initial void patches. This could deal with the fact that

The other approach is the hierarchical one, where directly on the oversegmented tessellation some of the divide lines are removed. This removal must be done according to some criterion. A good indicator could be to remove the boundaries that represent filaments with small contrast between two adjacent basins. See figure 9, this shows the skeleton of the maxima (green) and the minima (red). The green lines partly connect the void patches and these paths have the least topological distance connecting to void patches. If such a path has a high cost then the

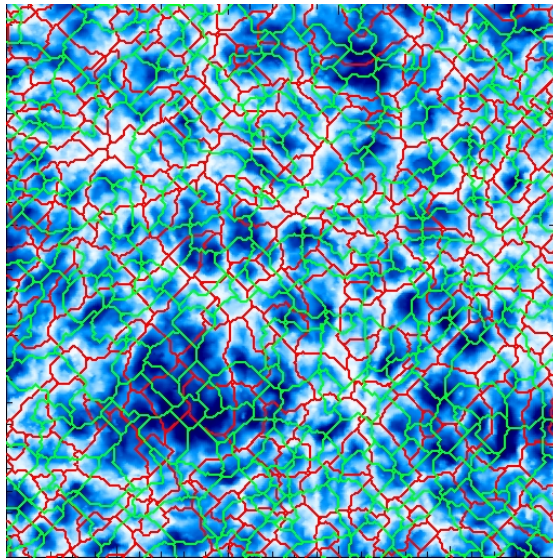


Figure 9.1: The figure shows the watersheds of the maxima in green and of the minima in red.

dividing filament is well defined and vice versa it is less prominent. In principle such a scheme might also be able to reduce the oversegmentation. This has the advantage that it only looks at the local curvature of the filament, therefore it is independent of the underdensity of two voids. So this could in principle be a way to remove the oversegmentation in more overdenser smaller voids, thus those not removed by thresholding.

The analysis of the voids showed that the external and internal tidal field plays a large role in the removal of small voids. This was not taken into account by the model of SW04. However Seth & Tormen showed that how to incorporate this in the excursion set model. This can also be done for the void collapse model of SW04 by including the ellipsoidal model. Thus in future work the model has to be updated and compared with the voids found with the 3D watershed method.

The watershed method also detects the filament, therefore a more detailed study of the void merging can now be done. This involves a study of the time evolution of the boundary density. Also the evolution of the in- and outflow pattern needs special attention. Theory predicts that the dividing walls should stream empty, and therefore the density decrease and two voids merge. This can now be checked by with the watershed method.

The extension to redshift surveys can also be done. The fastest way in doing it is by using an interpolated density field and applying the watershed transform in the same manner as was done here. Furthermore the watershed method is based on a weighted graph, therefore it is also possible to extend the method to point distributions. The only requirement is that the density for each node is known and that the connectivity is specified. Clearly this asks for DTFE to specify the density at the location of a galaxy/particle and the connectivity is given by the delaunay triangulation.

Acknowledgments:

Appendix A

Delaunay Triangulation Field Estimation, DTFE

A.1 Delaunay-Voronoi tessellations

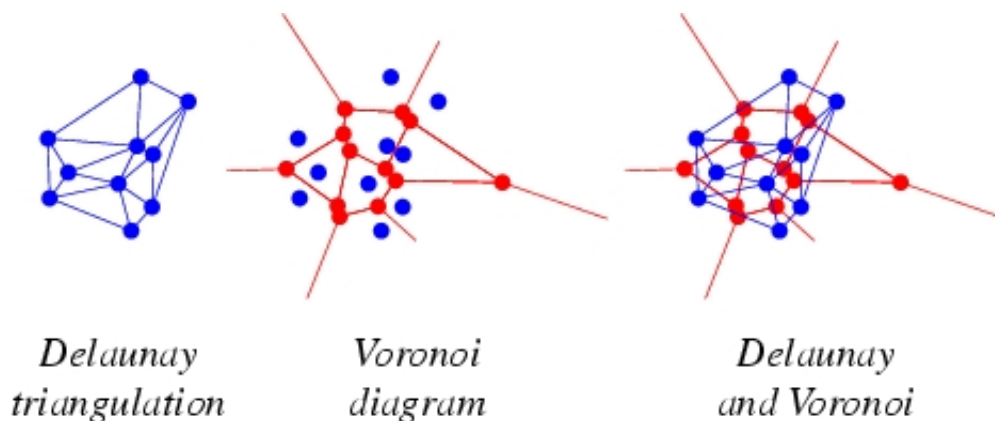


Figure A.1: The figure shown resp. the delaunay triangulation of a point set, the voronoi tessellation in red of the same point set. And the right one shows them projected on top of eachother to show their dual relation. From <http://mathworld.wolfram.com/DelaunayTriangulation.html>

The mathematical definition of a tessellation is regular tiling of space(3D) by polyhedra. There are different ways of tessellating space, depending on what kind of polyhedra is used. One way of doing this is using a Dirichlet region, this is a polygon of which all interior regions are closer to a particular lattice point than any other. Such a tessellation of space is called a Dirichlet tessellation or more commonly referred to as a Voronoi diagram, see figure A.1.

A three dimensional Voronoi diagram consists of vertices points, edges and faces of the polyhedron. Each faces is a part of the plane, which bisects space between to neighboring points. The line where two faces meet is called the edge of the cell and these edges cross eachother at the vertice points of the voronoi cell.

From the Voronoi diagram one can construct another tessellation, the Delaunay triangulation which is the dual tessellation. This is the connection of four voronoi neighbours via a tetrahedron. In two dimensions this would be three neighbours connected with a triangle, see figure A.1. The proper definition of a Delaunay triangulation is a devision of space in traingles or tetrahedra,

such that there are no other points are presents within its circumscribing circle or sphere.

A.2 Interpolation of points distribution to a grid

In N-body simulations the point distribution is a Monte-Carlo representation of the underlying density field. So to each particle is a certain amount of mass associated, and thus the density is proportional to the number of particles in a given volume. Then the problem of interpolation lies in chosing the volume of these bins in such a way that there are enough particles in the bin in order to supress the shot noise of the particles, but a fine enough grid to retrieve the most information out of the underlying field. Choosing a coarse grid will minimize the noise but yield little information and taking a very fine grid will maximize the noise, i.e. one will recover just the particle distribution. Especially, in low density regions one is sensitive to this noise, since there are very few particles that represent the field.

The solution would be to cellurize space in such away that one would place larger cells in places where there are viewer particles and smaller cells where there are more, so a grid that adapts itself to it's local enviroment. The way to do this is by looking at the neighboring particles of each individual particle, only how do we find these particles? An intuitive way to find these neighboring particles is by the Voronoi diagram. In this sense the inverse of the volume of the polygons will represent the density of the field. It was shown by Schaap (2005) that if one takes the inverse of the sum of the volume of all the delaunay tetrahedra around a particle that this recovers the density exactly.

The DTFE method of interpolating the density field goes as following; first one constructs a Delaunay triangulation on the particles. Then for each particle one calculates the volume of the contiguous voronoi cell, and thus the density at the position of each particle. Subsequently one interpolates these values to regular grid. To first order this can be done as following, for each regular grid one determines in which delaunay cell it is located and then one determines the gradient within the cell via the four vertices, the value at this grid node is then determined via linear interpolation.

Appendix B

Simulation Method, P³M

The code we used to perform our simulations was of P³M kind, see Efstathiou et al. (1985) and Bertschinger (1998). This acronym stands short for Particle-Particle, Particle-Mesh the latter meaning that the main part of the force computation is solved on a Eulerian grid, by means of Fast Fourier Transforms. The former means that for distances smaller than one grid spacing the force is computed in a direct manner by summing contributions of each particle.

In this code the interpolation steps to and fro the particles and grid are done with the Triangular Shaped Cloud (TSC) method. This attributes from each particle the mass, velocity or any other field value to the 27 nearest grid nodes, see also Hockney and Eastwood (1981). This interpolation scheme is also used for the force interpolation. The equation of motion that needs to be integrated is (see e.g. Peebles(1980));

$$\dot{v}_i + 2\frac{\dot{a}}{a}v_i = -a^{-3} \sum_{i \neq j} \frac{Gm_j x_{ij}}{|x_{ij}|^3}. \quad (\text{B.1})$$

Here m_i is the mass of the particles and x is the comoving coordinate which related to the physical coordinates r as $r = ax$. And $\dot{x} = v$ denotes the comoving velocity. The force is solved on a grid, this is because the summation in the previous equation leads to an $O(N^2)$ code and it does not represent the underlying continuous density field at small distances.

Therefor the particles are interpolated on a grid, so to get a field value on every node. In this code the interpolation steps to and fro the particles and grid are done with the Triangular Shaped Cloud (TSC) method. This attributes from each particle the mass, velocity or any other field to the 27 nearest grid nodes, see also Hockney and Eastwood (1981). The force is calculated by solving Poisson's equation for the gravitational field;

$$\nabla^2 \phi = 4\pi G a^2 \rho \quad (\text{B.2})$$

$$\phi(n_i) = \sum_{n_j, i \neq j} \mathcal{G}(n_i - n_j) \rho(n_j). \quad (\text{B.3})$$

$$(\text{B.4})$$

Here \mathcal{G} is the Green's function of the Laplacian in the B.4. And then taking the derivative of this field, yields the force field. Then the force is interpolated back on the particles via the TSC method, this gives in the right hand side of equation B.1. The fastest way to solve Poisson's equation is by going to Fourier space and noting that B.4 becomes a convolution. This is not only fast, but also incorporates naturally periodic boundary conditions. The Green's function often has to be modified to correct for inaccuracies in the strength and isotropy of the force.

If the typical distance of the particles is less than the grid spacing. The previous force solution underestimates the force, to obtain better spatial resolution a correction can be introduced. This

is the P² component of the simulation. Here these are tabulated, interpolated and the short range component is added to the particles. Furthermore here a leapfrog scheme was used to integrate the equation of motion and a fixed amount of time steps was distributed linearly from the initial expansion factor to $a=1$.